
Detection of Thin Structures in Biomedical Images

A thesis submitted by

Neda Sadri

In fulfilment of the requirements for the Doctor of Philosophy degree in

Computer Science

Faculty of Science, Engineering and Computing

Kingston University London, United Kingdom

January 2018

Director of studies: Prof. David Wertheim

RESEARCH DEGREE CANDIDATE'S DECLARATION FORM

I, Neda Sadri, declare that this thesis titled, Detection of Thin Structures in Biomedical Images is my own original work.

I confirm that all material contained in the dissertation is my own original work and that any references to or use of other sources have been clearly acknowledged within the text.

Neda Sadri.

November 2017

Acknowledgements

I would like to thank my supervisor, Prof. David Wertheim, who provided me his continues support, patience and encouragement at every stages.

I would like to express my warm and most sincere gratitude to my second supervisor Prof. Sarah Barman, for her support and guidance.

Many thanks to Dr Paraskevi Goggolidou for her kind support and providing the cilia data and images.

Many thanks to Prof. Jamshid Dehmeshki for all his supports and attentions.

I would express my appreciation to my dear mother, father, sister, my grandad and my husband for supporting me with their love every minute during my work and my study.

I would like to express my sincere gratitude and thanks to Mr Douglas Frances Turner with his unconditional support since I started my research by looking after my son, Master Parsa Shafiee, which with his great support, I have been able to focus on my research.

Finally, I am also thankful to the people whom I did not mention but have a valuable contribution to this research.

Neda Sadri
November 2017

Abstract

Lung cancer is life-threatening and difficult to treat. According to the World Health Organization, lung cancer is categorised by uncontrolled cell growth in tissues of the lung and is the most common cancer with 1.59 million deaths worldwide in 2012. There are estimated to have been 1.8 million new cases of lung cancer in 2012. About 20% of lung cancer cases are not thought to be related to smoking. Vessel characteristics may change in association with tumours for example due to angiogenesis which is a fundamental component in the development of tumours. Radiological images including MRI and CT can detect lung tumours and surrounding vasculature. Manual detection of vessel-like structures is time-consuming. Thus, computer-assisted detection of vessel-like structures may help in tumour assessment.

Cilia are membrane-bounded microtubules-based extensions of the centrosome that have different roles in mammalian development and adult physiology. Disorders of cilia or ciliopathies are associated with a number of genetic disorders such as situs inversus. Cilia-like blood vessels are thin structures and assessment of number and length are considered important in the detection of disease. Manual detection of cilia is also difficult and time-consuming.

This project divided into two applications of thin structures in biomedical images. First, the detection of the thin structures of cilia from microscopy images was performed used different techniques with aspects of linearity. Second, the best segmentation technique was created and developed to detect the cilia from microscopy images established and applies on the thin structure of vessels in CT scan images. The quantifications of both thin structures of cilia and vessels such as numbers and lengths were investigated.

The aim of this thesis is to develop and apply techniques for detection of thin structures in medical images with particular reference to microscopy images of cilia and CT images of vessel-like structures in the vicinity of a lung tumour.

A semi-automatic method was developed that combines mathematical morphological operations to enhance the thin objects combined with global thresholding, followed by user interaction methods to detect overlap and disconnected objects.

The system was successfully applied to detect cilia from electron microscope images and to detect vessel-like structures in CT images of lung cancers. The techniques were applied to assess a number of features such as number, length and tortuosity. In a study of unilateral lung tumour image sets, a statistically significant difference was detected in the number of vessel-like structures in the region of lung tumours compared with the contralateral side with no tumour.

Thus these methods may have application in detecting thin structures in microscope images as well as CT or other medical imaging modalities.

Publications and Presentations from the Research in this Thesis

[1] N. Sadri and D. Wertheim, Investigation of Vessel Structure in the Vicinity of Lung Tumours, London, Thorax 2016 71: A8.

[2] N. Sadri and D. Wertheim, Computer detection of thin structures in lung CT images, BIR Annual Congress, London November 2017.

Internal Presentation

N. Sadri and D. Wertheim, Sarah Barman and Paraskevi Goggolidou, Detection of thin structures in Biomedical images, presentation at Kingston University, 2013.

Table of Contents

Acknowledgements	ii
Chapter 1 Introduction	1
1.1 Motivation	1
1.2 Aim and objectives	3
1.3 Contribution to Knowledge	3
1.4 Thesis outline	4
Chapter 2 Cilia Biology and Manual Measurement of Cilia Properties	6
2.1 Introduction.....	6
2.2 Cilia Biology.....	6
2.3 Scanning Electron and Confocal Microscopy	10
2.4 Other Microscopic Technique	12
2.5 Methods and Material	13
2.6 Visual Analysis of Cilia Images.....	13
2.7 Manual Methodology of Cilia Detection	14
2.8 Experimental Results of Manual Analysis of Cilia.....	16
2.9 Conclusion and Discussion	19
Chapter 3 Literature Review	21
3.1 Introduction.....	21

3.2 Pre – Processing	22
3.3 Thresholding based on Intensity Value	23
3.4 Region-Growing	24
3.5 Directional filters	25
3.6 Derivative-based methods	28
3.7 Deformable models	30
3.8 Morphology Operations	30
3.9 Classification	33
3.10 Conclusion and discussion	36
Chapter 4 Cilia Detection Methodologies for Segmentation Process of SEM Cilia Images	38
4.1 Introduction	38
4.2 Background	39
4.3 Materials	39
4.4 Cilia Detection Framework	40
4.5 Methodologies for Cilia Detection	46
4.5.1 Methodologies	46
4.5.2 Pre-Processing Stage	46
4.5.3 Cilia Enhancement	48
4.5.4 Post Processing Stage	59
4.6 Cilia Length Measurements Methodology	59
4.7 Measurement of Overlap Cilia Images	61
4.8 Experimental Evaluation	62
4.8.1 Measuring Performance	62

4.9 Results	65
4.9.1 Segmentation Results.....	65
4.9.2 Cilia Length.....	74
4.9.3 Number of Cilia	76
4.10 Summary	77
4.11 Discussion and Conclusions.....	81
Chapter 5 Manual Analysis of Vessel-like structures in the Vicinity of Tumours ...	83
5.1 Introductions.....	83
5.2 Lung Cancer and Blood Supply	84
5.3 Material.....	91
5.4 Lung Imaging Modalities.....	92
5.5 Methodology of Visual Analysis of Lung CT Images	96
5.6 Experimental Results of Visual Investigation.....	100
5.6.1 Lung CT-Diagnosis Lung 1	100
5.6.2 SPIE-AAPM-NCILung Nodule Classification Challenge-LUNGx Lung 2.....	105
5.7 Summary	112
5.8 Conclusions and Discussion.....	114
Chapter 6 Quantifying Vessel-like Structures in Lung CT Images	115
6.1 Introduction.....	115
6.2 Literature Review	116
6.3 2-Dimensional Datasets	118
6.3.1 Windowing (Histogram Adjustment).....	119
6.3.2 Extraction of Lung Region.....	120

6.3.3 Lung Vessel CT Image Enhancement	121
6.4 Semi-Automatic Quantification of Blood Vessel Attributes	126
6.5 3D Visualisation of Vessels in Lung CT Images	128
6.6 Experimental Evaluation	132
6.6.1 Materials	132
6.6.2 Performance Measurements.....	132
6.7 Results	133
6.7.1 Lung CT-Diagnosis in Tumour Area Dataset Lung1	134
6.7.2 Lung CT-Diagnosis from Complete Lung Area Dataset Lung1	140
6.7.3 Lungx Challenge of Tumour Area – Dataset Lung 2.....	144
6.7.4 LUNGx Challenge from Complete Lung Area-Lung 2.....	149
6.7.5 Experimental Results of 3-Dimensional Visualization	157
6.8 Summary	160
6.9 Conclusion and Discussion	162
Chapter 7 Conclusion and Future Work.....	163
7.1 Introduction.....	163
7.2 Summary	163
7.3 Conclusion.....	167
7.4 Achievements.....	168

Glossary of Terms and Abbreviations

Cilia	Cilia is an organelle found in eukaryotic cells.
MRI	Magnetic Resonance Imaging
CT	Computed Tomography
SEM	Scanning Electron Microscope
TR	True Positive
FP	False Positive
FN	False Negative
TN	True Negative
SN	Sensitivity
SP	Specificity
AC	Accuracy
ROC	Receiver Operating Characteristic Curve
AUC	Area Under the Curve
TPF	True Positive Fraction
FPF	False Positive Fraction
KNN	K Nearest Neighbour

Spicule A small sharp body with a needle-like point.

Chapter 1 Introduction

1.1 Motivation

MEDICAL imaging allows visual representation of internal tissues of the body. The development of quantitative analysis and visualisation methods for extracting clinically useful information in medical images such as CT (computed tomography), MRI (magnetic resonance imaging) scan, or microscopy may help in detection and clinical monitoring. Computers are used for assisting in diagnosis for example to determine the presence of a tumour, the size of the tumour and such this information may thus support specialists in early diagnosing and treating medical disorders.

In this thesis, methods are developed and applied for segmentation and quantifications of the features in medical image applications. Of special the thesis interest is the detection of thin structures consider two applications, such as vessels from Lung CT images and cilia from microscopy images.

Lung cancer is life-threatening and difficult to treat. According to the World Health Organization, lung cancer is categorised by uncontrolled cell growth in tissues of the lung and is the most common cancer with 1.59 million deaths worldwide in 2012 (Ferlay *et al.*, 2015a). There are estimated to have been 1.8 million new cases of lung cancer in 2012 (Davies, 2018). The disease is the most common cancer in men worldwide and the second most common in women (Ferlay *et al.*, 2015a); it was the third most common cancer in the UK in 2014 (Davies, 2018). The incidence rates of lung cancer in the UK are estimated to fall by 7% between 2014 and 2035 (Davies, 2018). Lung cancer in the UK is common in people living in the most deprived areas (Davies,

2018). It is mainly caused by smoking but it is thought that about 20% of lung cancer cases are not related to smoking (Davies, 2018).

The centrosomes in cells help organise microtubules (Goggolidou *et al.*, 2014) including cilia. Thus cilia are membrane-bounded microtubules based extensions of the centrosome that have different roles in mammalian development and adult physiology (Goggolidou *et al.*, 2014). Ciliopathies are disorders of the cilia anchoring and are associated with a number of genetic disorders such as situs inversus (internal organs reversed or mirrored) (Baker *et al.*, 2009). Cilia fall into two classes: motile and immotile (primary cilia) cilia. Because cilia are a component of almost all vertebrate cells, dysfunction of them is likely to be associated with chronic disease (Waters *et al.*, 2011).

Thin structures such as lines are important features in many biomedical imaging applications. Medical examples include blood vessels in CT, valves in heart magnetic resonance imaging. Visualisation of such structures provides crucial information in planning, biopsy and diagnostic purposes. This thesis presents an approach in extracting and analysing thin structures, such as cilia and blood vessels from 2-dimensional biomedical images. There is a considerable amount of work has been performed on the enhancement and segmentation of blood vessels. It should be the straightforward task to apply existing segmentation algorithms with the aspect of linearity to similar thin structures such as cilia and blood vessels. However, biological images in the microscopic scale are much noisier and remain a challenge to the use of existing methods. The focus in this thesis is on the detection of thin structures in 2-dimensional medical images. More precise, is detection and quantification of thin structures particular reference to cilia and vessels.

1.2 Aim and objectives

The aim of this thesis is to develop and apply techniques for the detection of thin structures in biomedical images with particular reference to microscopy images of cilia and lung cancer of CT images.

Objectives:

- A. Visual investigation of cilia features from microscopic SEM images.
- B. Pixel-based labelling of cilia images was performed to evaluate the binary segmentation.
- C. Develop an algorithm for cilia segmentation and quantification such as cilia numbers and cilia lengths.
- D. Develop a semi-automatic algorithm based on best fit ellipse to measure the lengths of overlapping cilia.
- E. Visual investigation of vessel-like structures including spicules features in the vicinity of the lung tumours.
- F. Segmentation and quantification of vessel-like structures in lung CT images.

1.3 Contribution to Knowledge

This work claims the following contributions to knowledge:

- A. A novel semi-automatic algorithm for the detection and quantification of thin structures in medical images has been developed and applied to the new application of microscope images of cilia and CT lung images.

Chapter 1 Introduction

- B. The system was successfully applied to detect a new application of cilia from electron microscopy images.
- C. The system was able to count the number of cilia and measuring the length of the cilia.
- D. A semi-automatic method applied to detect and measure the overlapping cilia lengths
- E. The techniques applied to detect vessel-like structures in CT images of lung cancers.
- F. It was also used to assess a number of features such as number, length and tortuosity of the blood vessels in CT images. In a study of unilateral lung tumour image sets, a statistically significant difference was detected in the number of vessel-like structures in the region of lung tumours compared with the contralateral side with no tumour.

1.4 Thesis outline

- Chapter1: Describes aim, objectives and contribution to knowledge of the thesis.
- Chapter2: Describes the biology and manual analysis of cilia.
- Chapter3: Literature review of methods applied for segmentation of the thin structures and theories of image processing for different applications.
- Chapter4: Describes the methodology and results of the detection of linear structures (in cilia) by using different techniques.
- Chapter5: Elaborates the lung cancer and the appearance of vessel-like structures and manual analysis of lung CT images.

Chapter 1 Introduction

Chapter6: Illustrates the blood vessels segmentation in the vicinity of lung tumours and show the quantification results.

Chapter7: Describes the conclusion and future work.

Chapter 2 Cilia Biology and Manual Measurement of Cilia Properties

2.1 Introduction

THE objective of this research is to develop and apply image segmentation to thin structures in medical images to allow further quantitative analysis. This chapter begins by exploring cilia biology. Firstly, it discusses the biology of nodal cilia. Secondly, it describes the material and image capturing processes for cilia images. Finally, it introduces manual analysis measurements of thin cilia structures.

2.2 Cilia Biology

Cilia are slender membranes and hair-like structures (Satir and Christensen, 2007), organelles that project out from the surface of the cell that demonstrates different roles in mammalian. Cilia are multiple or single and are composed of nine parallel microtubule doublets (Oh and Katsanis, 2012) surrounded by an extension of the plasma membrane. Motile cilia are long and thin (Baker and Beales, 2009), constructed of nine outer microtubule doublets and two microtubules in the centre, this is termed of “9+2” architecture microtubule (Satir and Christensen, 2007). Their length extends up to 20 μm from the surface of the cell (Baker and Beales, 2009). These thin and lengthy structures tend to appear in large numbers from the surface of the cell. They work to clear mucus from the respiratory epithelium and drive sperm along the Fallopian tube (Shoemark, 2014). In contrast, primary cilia lack a central pair of microtubules, have an arrangement of “9+0” and referred to as single non-motile (Baker and Beales, 2009). Primary cilia are immotile (Baker and Beales, 2009), with the exception of nodal cilia of the vertebrate embryo. They perform on the apical surface of the epithelial cells such as kidney tubule (renal cilia) (Kramer-Zucker *et al.*, 2005). The outer and inner microtubules are connected (Baker and Beales, 2009) to the basal body and their cylindrical structure is perpendicular to the cell membrane that

attaches cilium in the cytoplasm. The single primary cilium is present (Oh and Katsanis, 2012) in most cells however the number of motile cilia can vary from 200 to 300 per cell type.

In recent decades, it has been suggested that cilia are involved in multiple complex human diseases which may be classified as ciliopathies (Baker and Beales, 2009). Ciliopathies belong to class genetic diseases these diseases result in devastating effects affecting millions of people worldwide (Baker and Beales, 2009). Ciliopathies can cause wide-ranging phenotypes in mammals such as retinal degeneration, renal, pancreatic cyst formation, and situs inversus (Baker and Beales, 2009).

Both motile and non-motile cilia are necessary for left-right patterning and asymmetric positioning of all internal organs (Baker and Beales, 2009). Vertebrate organs are externally symmetrical between left and right, whereas patterning and organisation of their visceral organs and vasculature demonstrate asymmetry (Ermakov *et al.*, 2009a). Therefore an error in nodal cilia (9+2) of the early embryo causes asymmetry of the heart and visceral organs with a 50% risk of situs inversus (Levin, 2005).

The absence of all cilia (Norris and Grimes, 2012) causes early embryonic death. Menzl *et al.* present a study of primary cilia loss in pre-invasive breast cancer (Menzl, Ina, Lebeau, Lauren, 2014). The role of cilia has been investigated in some human cancers (Yuan *et al.*, 2010) and it has been shown that pancreatic cancer, prostate cancer, renal cell carcinoma all show a general loss of cilia (Yuan *et al.*, 2010). The studies suggested that loss of cilia may increase cancer development in some tissues. Therefore analysis of the role of the cilia became necessary and important to have a comprehensive analysis of cilia expression in human cancers. Therefore researchers studied the primary cilia frequency and their lengths from breast cancer to expand the knowledge of the role of primary cilia features in premalignant breast cancer lesions (Yuan *et al.*, 2010). One investigation was both on pre-invasive, invasive breast cancers (Yuan *et al.*, 2010). It was

been demonstrated primary cilia frequency was decreased in all stages. Also, primary cilia were lost on pre-invasive breast cancer lesions suggesting that this is an early event in cancer development (Yuan *et al.*, 2010). The number of cilia and their lengths were defined by counting cilia per cell and measuring length. Their study suggested that primary cilia are lost in breast cancer development of the cell cancer and the surrounding cells. The lengths of nodal normal cilia (wild-type) of embryos on day 8 (embryonic day) were measured and the lengths were approximately 4-6 μ m (Sulik *et al.*, 1994).

Goggolidou *et al.* study the lengths of cilia from three mouse mutants. They found the average lengths of the normal nodal cilia were 3 μ m (Goggolidou *et al.*, 2014).

The Ataxia telangiectasia mutated (ATM) gene was identified in DNA damage repair. The ATM gene changes the function of the protein in the cell and sends signals to the cell. Experiments of ciliogenesis genes in mouse embryo (gpg6) confirmed ATMIN and its transcriptional target (DYNLL1) are important for normal lung morphogenesis and ciliogenesis. As ATMIN regulates expression of ciliogenesis genes, they are required to measure the true length of cilia in the embryo. Goggolidou *et al.* examined the lengths of cilia and found the average lengths of Atmin gpg6 average nodes length are <1.5 μ m and the normal nodal cilia were 3 μ m (Goggolidou *et al.*, 2014). Ermakov demonstrated (Ermakov *et al.*, 2009b) gpg6 had short and stumpy nodal cilia.

The literature showed that the thin structures of cilia are having a vital role in mammalian physiology therefore analysing of these thin structures features are important for further investigation of the disease. Investigation of cilia and cell morphology may help in the further investigation of a variety cilia-related disease. Diseases generally respond better to treatment if they are being diagnosed at an early stage.

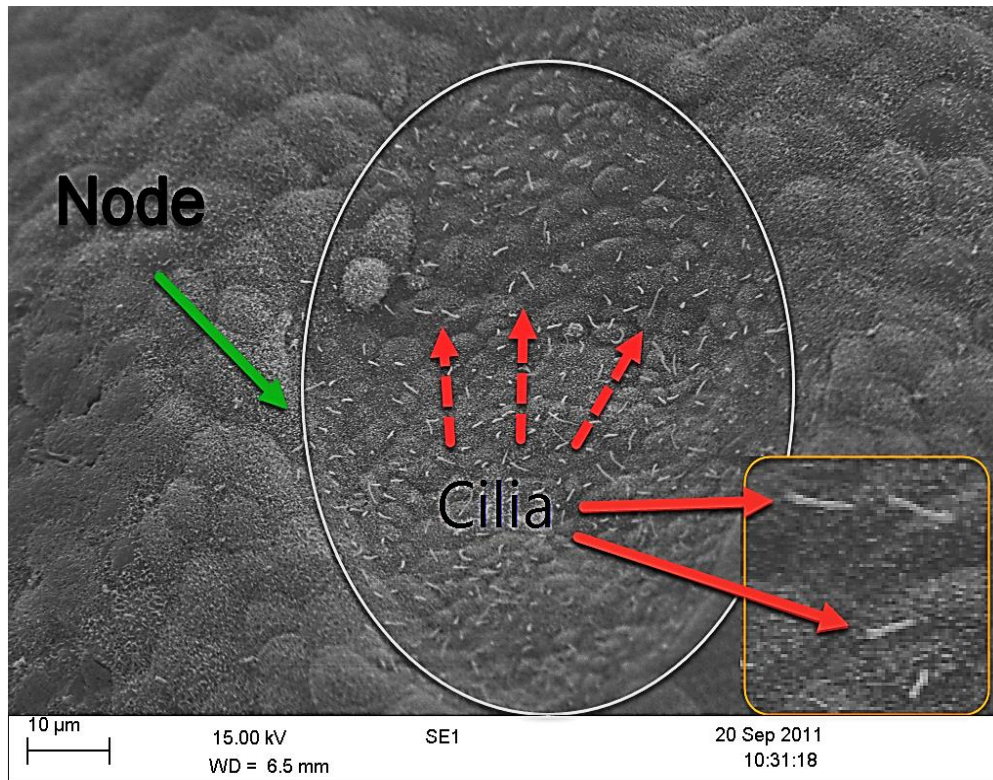


Figure 2.1: An image from the dataset. Nodal image of cilia with a 10µm magnification scale bar. The ellipsoidal area shows the node contains cells and cilia hanging from the surface of the cell. Red arrows point at cilia. Image of cilia presented in a zoomed orange box.

Figure 2.1 shows the original nodal cilia image example from the dataset. The white oval shape displays the whole node and the green arrow points to it. The open red arrows point to the cilia within the node. This illustrates the whole node and shows the normal cilia that are projected from the surface of the cells. There are nodal cilia lying flat and highly magnified in the orange box in the panel. These types of images (nodal images) are used to investigate the number of cilia.

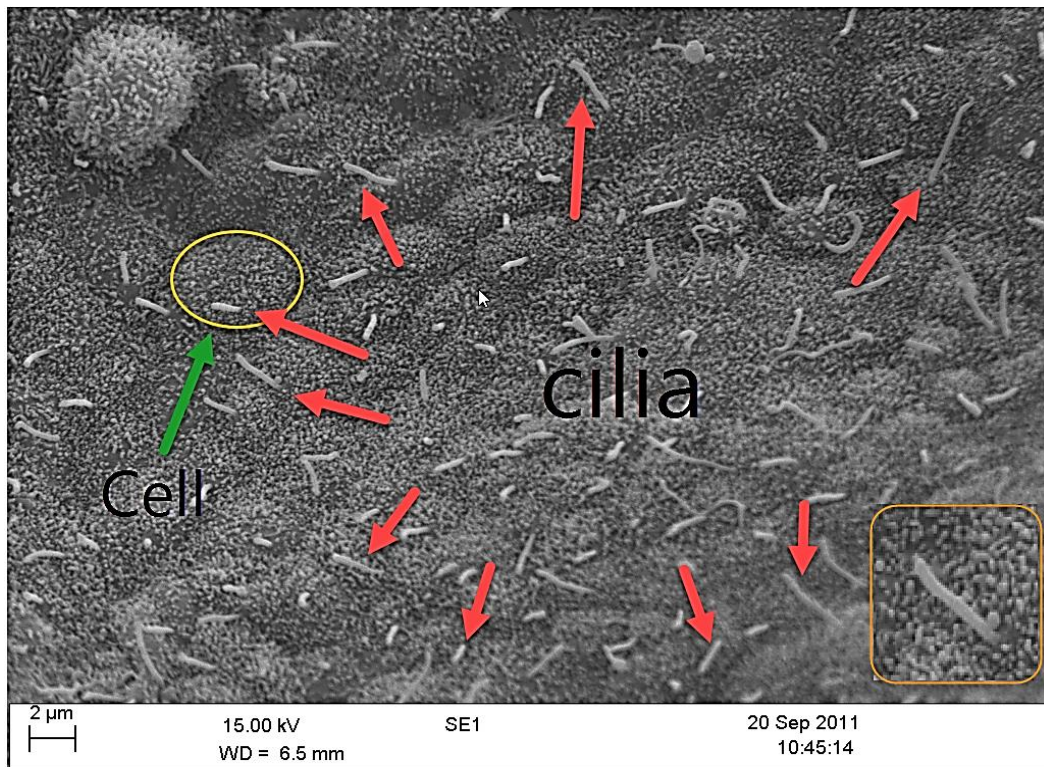


Figure 2.2: Image from the dataset. High-resolution cilia image with a 2 μ m magnification of scale bar. Cilia hang from the surface of the cell in diverse orientations. The cilium in the orange box shows higher magnification of one cilium from the main panel.

Figure 2.2 illustrates the original 2-dimensional high-resolution image of normal cilia. This image is of nodal cilia with a 2 μ m magnification scale bar. The orange square shows the zoomed in cilia. The yellow border with green arrow demonstrates the border of the cell with cilia hanging from the cell surface.

2.3 Scanning Electron and Confocal Microscopy

Scanning electron microscopy (SEM) allows visualisation of fine detail and offers insight into the structure and functionality of various delicate structures (Erdman, 2018). Scanning electron microscopy image methods can be used to magnify sub-cellular elements such as cilia and provides details of the surface of cells. SEM devices offer the ability to view the very tiny hair-like structure of cilia (Goggolidou *et al.*, 2014).

SEM is one of the best ways to very closely look at the surface of the cilia. SEM uses electrons instead of light to view objects in detail. The electron gun (electron source) releases the electron through the condenser lens (used to adjust the diameter of the electron beam) and the objective lens (used for focusing of the final diameter of the electron beam). The electron beam from the electron gun is focused by the magnetic lens and objective lens. These lenses are magnetic and help narrow down the electrons to be properly focused on the specimen. When primary electrons hit the surface of the specimen, electrons emitted from the specimen are detected by a secondary electron detector. Then the output from the secondary detector is transferred to a computer to construct and form an SEM image. The number of secondary electrons forms a SEM image as the brightness variation of an image depends on the number of the secondary electrons appearing on the display unit. Because the energy of the secondary electrons is very small, only those produced at the surface of the specimen are detected by secondary detectors. If the incident electron beam (primary electron) enters perpendicularly to the surface, the number of secondary electrons emitted from the surface of the specimen is less than if the electron beam enters indirectly. The difference in brightness of the specimen surface depends on the difference of the incidence angle of the electron beam. Therefore the secondary electrons are used to observe the topology of the specimen surface.

The electrons absorbed into the specimen lose their energy and they stop moving around the specimen. Therefore to make the electrons flow through the specimen and prevent the charging the specimen needs to be conductive. A non-conductive specimen is coated with a highly conductive thin metal film such as noble metal (gold-silver-platinum) (Erdman, 2018). Figure 2.1 is a schematic diagram represents the elements of the SEM device. The SEM devices have been used to capture the cilia images.

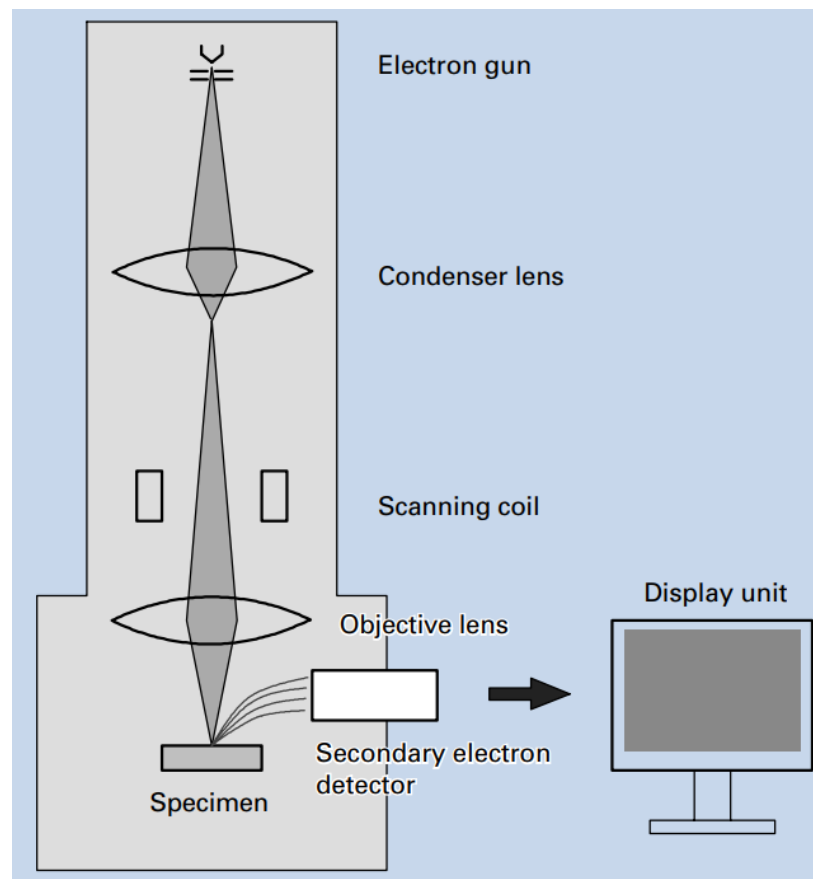


Figure 2.1: Schematic diagram of a SEM device (Erdman, 2018).

2.4 Other Microscopic Technique

Laser scanning confocal microscopy shortened to just confocal microscopy is one of the most advanced devices in optical microscopy developed, primarily because the technique enables deep visualisation of living and fixed cells and allows the user to do optical sectioning. Confocal microscopy also can be used to capture and form cilia images. Laser scanning confocal microscopy uses a laser beam to focus onto the specimen. It works by passing a laser beam through a light source to pass a pinhole which is then focused by an objective lens. The objective lens focused these lights into a small area on the surface of the specimen. The pinhole passes only the focuses light to the specimen. Then detectors collect the photons emitted

from fluorophores in the specimen. These detectors transform the light into an electrical signal that is recorded by a computer (Paul, 2017).

2.5 Methods and Material

Cilia samples were isolated from the Harwell archive (Goggolidou *et al.*, 2014). To prevent the deformation and the changing of the structure of the tissue after its death the tissue needs to be fixed by chemicals such as glutaraldehyde and dehydrated by ethanol or acetone. Cilia fixed, and were dehydrated through an ethanol series, and viewed in a scanning electron microscope (Goggolidou *et al.*, 2014). Images were captured under the direction of Paraskevi Goggolidou (Ermakov *et al.*, 2009b),(Goggolidou *et al.*, 2014) at Kingston University. The images were captured from mouse embryos day of 8.5 (E8.5) to analyse. The 2-dimensional images were obtained from SEM device with different magnification. The images were captured in the digital form of size 768 x 1024 pixels and 8-bit grey scale. The images are stored in uncompressed, versatile TIFF-format (Tagged Image file format). The total dataset is 23 images obtained by three different observers included normal (wild-type) and abnormal (mutant type) nodal cilia. Only 3 normal and 3 abnormal were analysed.

In this thesis, two magnifications of cilia images were used with scale bars of 10 μ m (85 pixels) and 2 μ m (45 pixels).

2.6 Visual Analysis of Cilia Images

This section explains the manual quantification of cilia and the process of preparing them. The author used manual investigation of the cilia to obtain measurements for comparison with computer analysis. The purpose of this manual analysis was to use it to validate our automated system which will be proposing in chapter 4.

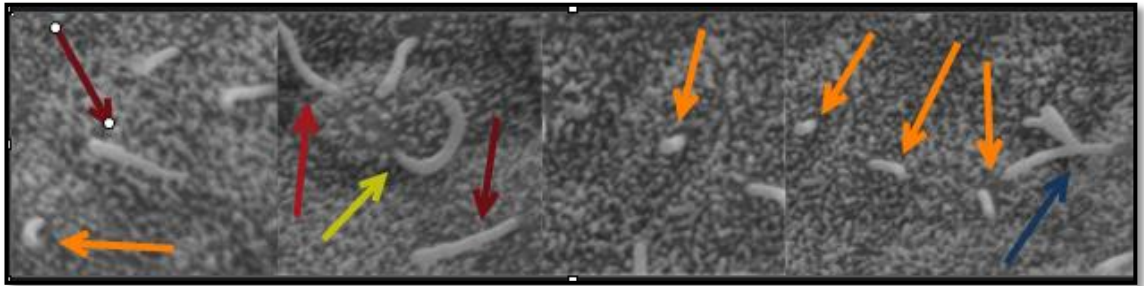


Figure 2.2: 2-dimensional zoomed in the image of figure 2.3, cilia with different angle position. Yellow and blue arrows point at a bent cilium and overlapped cilia respectively.

Figure 2.4 shows a zoomed in image of different positions of cilia on the image. A close look at this figure reveals the constraints of this study where due to the image being taken in 2-dimensional and because cilia are hanging from cells surfaces in different angles and directions, it is likely that the true length of many cilia cannot be obtained from such 2-dimensional images. For example, the red arrows point to some of the cilia with longer lengths, whereas the orange arrows show cilia with shorter lengths. The blue arrow shows the overlapping cilia. Having already known that the cilia image is from a normal dataset then they might have been from the cell surface in a different angular position than red arrows.

2.7 Manual Methodology of Cilia Detection

To perform this visual analysis, 2-dimensional high-resolution cilia images ($2\mu\text{m}$ magnification scale bar) were used to manually measure the length of the cilia. Nodal cilia images with $10\mu\text{m}$ magnification scale bar were used to count the number of cilia from the node. The assessment was performed on sets of normal and abnormal cilia images.

A manual image analysis procedure was performed in MATLAB version 2015b (The MathWorks Inc., USA). The image processing tool viewer called 'imtool' was used to measure the length of each cilium and the number of

cilia per cell from high-resolution images. The distance tool in “Image Viewer toolbar” assisted in measuring individual cilium lengths. This tool allows measurement of length with a click-and-drag approach. Length measurements were pixel based but the results were converted and are presented here in μm .

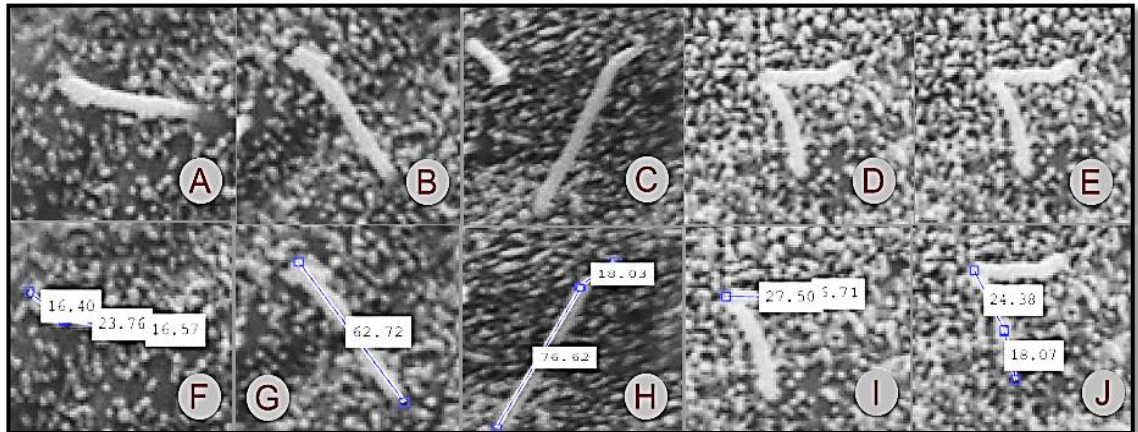


Figure 2.3: A, B, C, D and E each illustrate magnified cilia of diverse directions of original normal cilia image. F, G, H, I, J are demonstrate examples of manual measurements.

Figure 2.5, A, B, C, D and E show a zoomed in image of original high-resolution images of normal cilia in different directions. F, G, H, I and J demonstrate examples of how each cilium has been measured. Often cilia appear curved or overlap each other. Therefore in order to measure the true length of cilia, the observer is required to perform several clicks-and drags. In Figure 2.5, D and E with the results of the image I and J demonstrate an example of overlapping cilia which were measured separately.

The objective of length measurements of all data in terms of ground truth was to use it to evaluate the performance of algorithms. The results will be demonstrated in the next section.

2.8 Experimental Results of Manual Analysis of Cilia

Visual investigation of normal and abnormal cilia images was performed. The number of cilia was counted from the 3 normal and 3 abnormal nodal images (magnification of 10 μ m). The manual length measurements were also performed from the same 3 normal and 3 abnormal cilia slides but with higher magnification (2 μ m scale bar). Bar charts and individual value graphs were plotted to analyse the cilia images. The 3 normal and 3 abnormal cilia images were analysed.

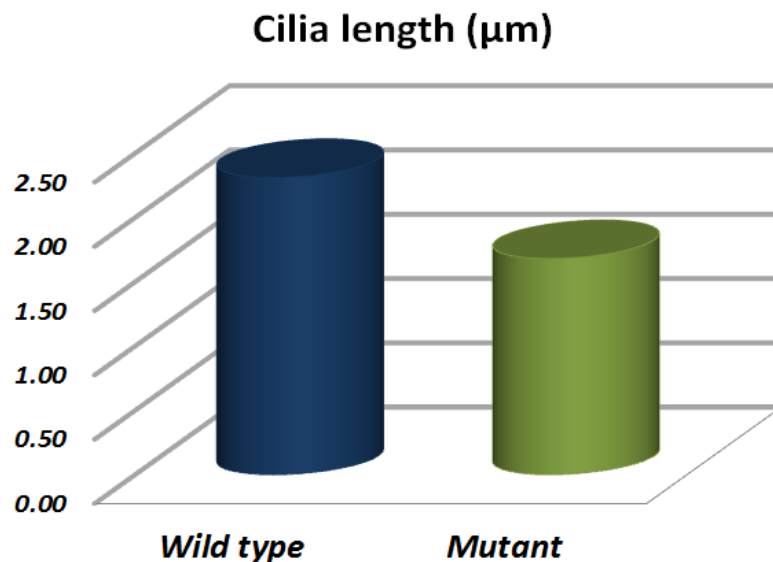


Figure 2.4: Comparative analysis of normal (wild-type) and abnormal (mutant type) cilia length. The bars show the mean of the cilia lengths for 3 normal and 3 abnormal cilia.

All visible cilia lengths were also measured and documented. Figure 2.6, the bar chart represents the mean of the normal and abnormal cilia lengths. The blue bar shows the mean of the normal cilia 2.31 μ m whereas the green bar represents the mean of abnormal was 1.6 μ m. Therefore, the mean lengths of the normal cilia were higher than the mean length of mutant type.

Goggolidou analysed the cilia length in normal and abnormal cilia. Their results revealed that the length of abnormal nodal cilia is shorter than normal as observed also in this study (Goggolidou *et al.*, 2014). Table 2.1 shows a summary of their results and the results were obtained by the author. The results show the abnormal cilia are short and stumpy compared to the normal cilia.

Cilia Length (μm)	Normal	Abnormal
Goggolidou	3	1.5
Sadri	2.31	1.6

Table 2.1: summery of the cilia length in μm

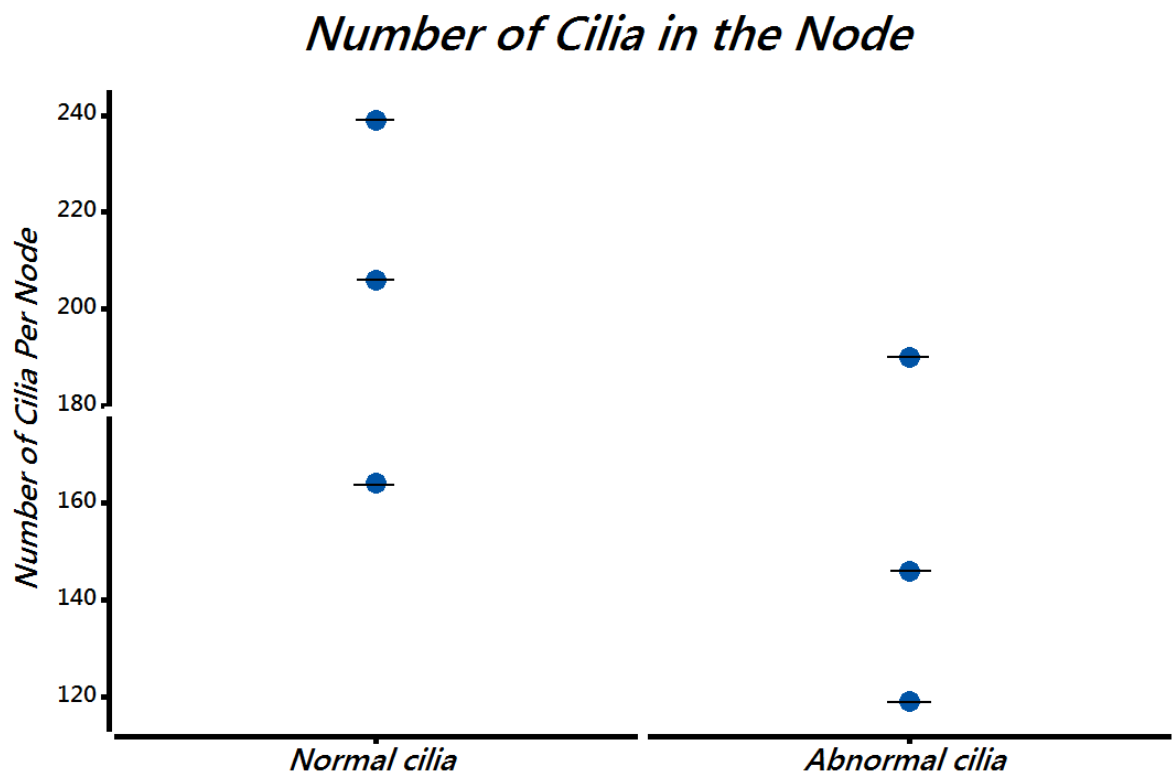


Figure 2.5: Individual value plot shows the number of cilia within the whole node of normal cilia and abnormal cilia per image.

The numbers of clear and visible cilia were counted from images of 10 μ m magnification scale bar. The number of cilia was initially counted from the whole node and for further analysis, they also were counted from the small crop of the node. The individual value was plotted, in Figure 2.7, it demonstrates the number of cilia counted from the whole node of the normal and abnormal images. The individual value plot of the cilia data shows that in 2 of 3 cases, there are more cilia per image in the 3 normal cases. In the abnormal cases, the number of cilia seems lower but numbers are low.

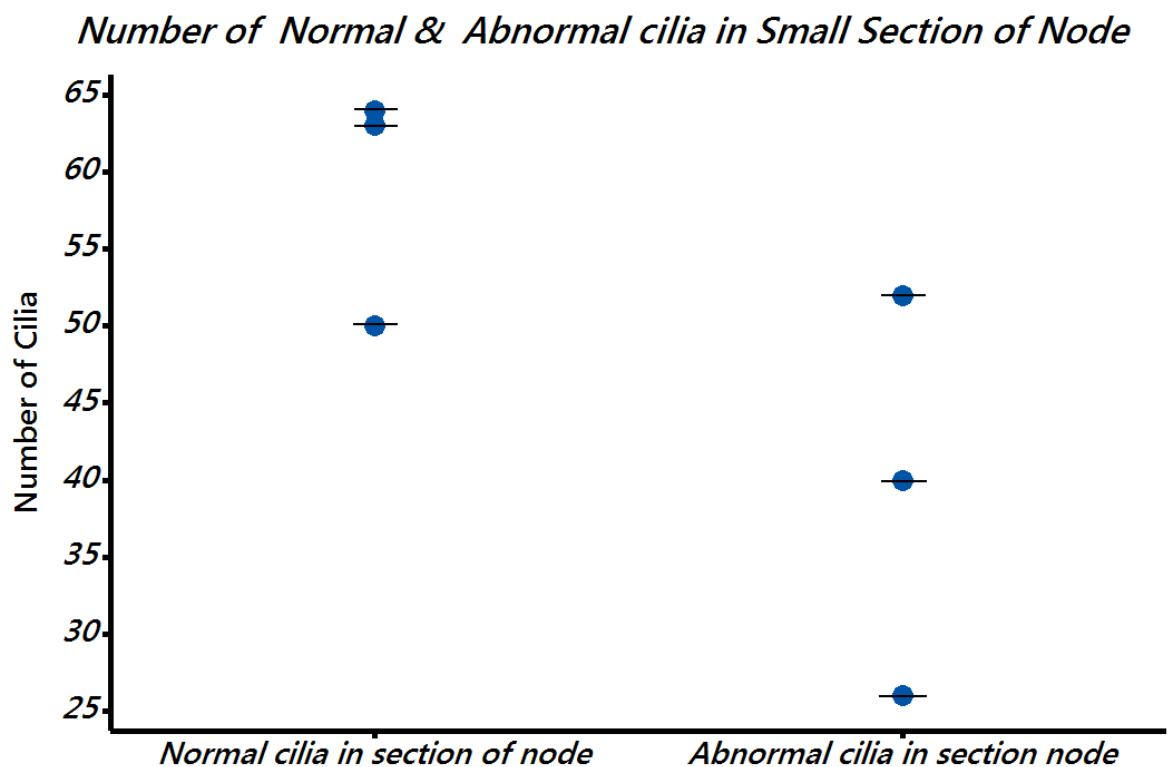


Figure 2.6: Individual value plot shows the number of normal cilia from the small section and the corresponding section from the abnormal image.

In addition, the number of cilia from small sections of the node was investigated. This was performed in a small section of the node of the normal cilia and compared to the corresponding area of the abnormal cilia images.

From the results shown in figure 2.8, for the number of cilia in the small section, the 2 of 3 normal images are higher than the corresponding area of the 3 abnormal images.

2.9 Conclusion and Discussion

Cilia are membrane-bounded hair like structures [6], organelles that hang from the surface of the cell that demonstrate different roles in mammalian and adult physiology. Identifying them at an early stage of the disease is vital as they respond better to treatments. Therefore investigation of the cilia feature may assist specialist for early disease investigation. Goggolidou analysed the cilia length in normal and abnormal cilia. Their results revealed that the length of abnormal nodal cilia is shorter than normal as observed also in this study(Goggolidou *et al.*, 2014).

For morphological analysis of cilia, the number and lengths of cilia were analysed. This investigation was performed on 3 normal and 3 abnormal images of cilia with 10 μ m magnification scale bar used to count the number of cilia in the node. 3 normal and 3 abnormal cilia images with 2 μ m magnification scale bar used to measure the lengths of the cilia.

The clear true lengths of cilia were measured manually with MATLAB. The length measurements were performed from normal cells and abnormal cells. The results suggest that nodal cilia of normal may be longer than abnormal cilia lengths, which is similar to previous investigation (Goggolidou *et al.*, 2014).

Chapter 3 Literature Review

3.1 Introduction

A HUMAN body tissue contains many different types of thin curvilinear structures such as blood vessels, bronchial trees, cilia on the cells and so on. The visualization of these curvilinear objects is crucial for the planning of and navigation during interventional therapy, surgery (Kikinis *et al.*, 1996),(Sato *et al.*, 1997) and diagnostic purpose. There has been a considerable amount of work done on the enhancement and segmentation of curvilinear structure via medical images such as cerebral blood vessels from magnetic resonance angiography (MRA) images (Vandermeulen *et al.*, 1992),(Bullitt *et al.*, 2005a) bronchial trees from lung CT images (Mori *et al.*, 1995),(Helmberger *et al.*, 2014).

The research field of thin structure image analysis has attracted a lot of interest from the history of image analysis in different areas. Automatic and semi-automatic detection of thin structures from medical imaging have received a considerable share of this interest. Curvilinear structure segmentation is broadly used in medical image analysis (Sato *et al.*, 1997).

Kirbas and Quek created comprehensive reviews and surveys of the methods for blood vessel extraction and elongated structures in 2-dimensional and 3-dimensional medical images in a variety of domain applications (C. Kirbas and F. K. H. Quek, 2003). Fraz *et al.* reviewed methodologies to segment blood vessels in 2-dimensional colour retinal images (Fraz *et al.*, 2012).

This chapter will briefly introduce the most common techniques of enhancement and segmentation in a variety of areas regarding thin structures in medical images. Hence, this review is not restricted to the thin

objects concerned in this project (cilia and lung vessels). These elongated thin objects can be considered to be similar to tubes. Importantly they can be approximated as piecewise linear objects; therefore, some of the most popular techniques take advantage of this property. For instance, the methodologies described in section 3.4 apply the filters (with a linear structure and at different angles) to the image in order to distinguish the objects of interest (e.g. cilia and lung vessels).

3.2 Pre – Processing

Most of the methodology present later in this work consists of pre-processing techniques. Pre-processing was performed prior to the image segmentation and depends on the quality of the image and the general image artefacts such as noise. Therefore, pre-processing stages are applied to suppress noise and correct the contrast and poor illumination in the background. Uneven illumination occurs because of the source itself, due to a nonlinear response of the detector, or due to poor sample alignment (Solomon *et al.*, 2011).

Medical images can have the problem of suffering from non-uniform illumination (Niemeijer *et al.*, 2005), correcting this problem allows for better enhancement and segmentation of objects from an image. Sae-Tang *et al.* suggested the method of using non-uniform illumination background subtraction on retinal images (Sae-Tang *et al.*, 2010). The method used the average filtering to estimate the background with non-uniform illumination. Then, the background was subtracted for further segmentation analysis.

Contrast Local Adaptive Histogram Equalization (CLAHE) (Pizer *et al.*, 1987),(Reza *et al.*, 2004) is an enhancement method extensively used. This method computes several histograms corresponding to a different section of the image and uses them to redistribute the lightness values of the image. The main idea of this method is to find the mapping for each pixel based on

pixel neighbourhood. Therefore, CLAHE is appropriate for improving the local contrast and image enhancement.

Histogram equalization is a global technique for adjusting intensities to enhance the contrast of an image (Gonzalez and Woods, 2008.). Abdullah-Al-Wadud et al. proposed smart contrast enhancement technique based on histogram equalization (HE). This partition the image histogram based on local minima and sets specific grey level ranges for each section prior to equalizing them separately (Abdullah-Al-Wadud *et al.*, 2007).

Images can be affected by mixing with some amount of noise which either uninteruptable or without interest. Filtering out these noises provides the way to the visual interpretation of images or help for further digital processing such as segmentation. Nonlinear median filter often used to reduce the "salt and pepper" noise and also preserves the edges of the objects. Teoh produced a revised survey of median filtering frameworks (Teoh and Ibrahim, 2012). Deswal et al. review a survey of different bilateral filtering techniques (Deswal *et al.*, 2015).

3.3 Thresholding based on Intensity Value

Early and simple techniques for segmentation are based on the theory that objects of interest in an image can be segmented based on intensity values only. This simple common approach identifies objects of interest by using a single global threshold value (Gonzalez and Woods, 2008.); pixels with intensity values of above and below the threshold are object pixels and background pixels. This approach is fine in high contrast objects with a high pixel value at the edges, but it fails often if the edges are smooth with varying intensity value and influenced by noise. An adaptation of this is a local adaptive threshold method in which the threshold varies according to the attribute of the local neighbourhood (Luessi *et al.*, 2009).

Kiraly et al. used CT images to propose a lung vessel segmentation method applying a global threshold operation to the lung region. Their intention was to find the location of pulmonary emboli; investigating the characteristics of a local arterial tree and analysing of arterial sub-trees which are affected by pulmonary emboli. As an initial stage, they segmented the entire lung vasculature by using a global threshold, labelling all connected components and eliminating small objects (Kiraly *et al.*, 2004).

3.4 Region-Growing

Region-growing has been one of the first complex techniques for image segmentation (Zucker *et al.*, 1976) and in particular vessel segmentation dedicated to seeded region-growing segmentation. Basically, region growing is based on two elements: one (or several) seed(s) (Adams and Bischof, 1994) assumed to belong to the structure of an object of interest to be segmented, and a propagation criterion that enables the segmentation of the object from the seed by iterative addition of adjacent pixels.

The approach is to start from a given seed point known as an object pixel. The neighbourhood of that pixel is categorised as background. Pixel/Pixels connected to the object are segmented by a recursive search and those pixels are classified as objects. The quintessential problem with this method is leakage because it is difficult to set a threshold value to confine an actual object.

Zhou et al. proposed a fully automatic pulmonary vessel tree segmentation by threshold-based region growing. Their proposed method was to design an automatic system to recognize lung anatomical structure. They applied the method on CT images that have a pulmonary embolism, even without applying any contrast enhancement. Because abnormal tissue or pulmonary embolism can destruct the vessel the region growing filter based method fails, therefore they modified their method by selecting a local threshold for small vessel branches (Zhou *et al.*, 2006).

3.5 Directional filters

The methods reviewed in this subsection take advantage of the piecewise linear characteristics of the objects of concern. They convolve a filter (with a linear structure) with the image that contains structures which are linear in some aspects (resembling a line) and apply this filter in multiple directions because the object of concern can appear in different orientations.

The matched filtering approach was proposed by Chaudhuri and became a common technique. It was introduced to segment retinal blood vessels. Blood vessel cross sections can be approximated by a Gaussian function and vessels can be considered as piecewise linear (Chaudhuri *et al.*, 1989). Therefore a 2-dimensional filter was designed to match the vessel appearance, with the linear aspect of the filter (this also made up the length of the filter) was created by stacking together multiple cross-sections of a single 1-dimensional Gaussian function. This filter was rotated in different directions and convolved with retinal images in order to match the blood vessels (which appear in different orientations). The vessel enhanced image was produced by taking at each pixel location the maximum response across all orientations. The binary vessel map was created by applying a global threshold. It was suggested that the matched filter could be extended to the detection of geological features from satellite images and enhancement of the fingerprint.

To extract segmented blood vessels, Jihene et al. applied matched filtering to segment the blood vessels in retinal images having been inspired by the method of (Chaudhuri *et al.*, 1989). The aim of the method was to examine the effect of topological changes in the retinal vasculature on the hemodynamic distribution in the retinal circulation. The matched filter kernel was applied in 12 directions over 180°. The final resulted image was computed by taking the maximum response of the 12 filters at each location. They used the final threshold image results for producing a binary

segmentation of the vasculature. The outcomes of the segmentation assisted the partition of the vessels in order to measure the tortuosity (Malek, Azar and Tourki, 2015).

Koller et al. assumed lines in 2-dimensions have a bar profile (Koller T. M.*et al.*, 1995). They presented the novel method to detect the elongated, symmetric line-like structure while suppressing the response to edges. The method was based on the extension of a Hessian matrix to multiple scales. It was a nonlinear combination of linear filters and had a steerable orientation and responded to the local contrasts while was independent of the local width. The algorithm searches for elongated and symmetric line structure was applied to the 2- dimensional image and proposes also an extension to 3-dimensional images from different applications leading to an efficient and parameter-free implementation. The algorithm was used to detect the line-like structures in an aerial scene, detect the stripes in the zebra images. This filtering was also applied to magnetic resonance volume images in order to detect the cerebral blood vessels.

The Gabor filter was originally introduced by Dennis Gabor. A 2-dimensional Gabor filter is a Gaussian kernel function modulated by a sinusoidal plane wave(D. Gabor et al., 1946). Hong believed the high performance of automatic fingerprint identification depended on the quality of an input image. Hong et al. used Gabor filters. The developed method adjusted the clarity of local ridge and valley pixels structures based on local ridge orientation and ridge frequency estimated from the input image (Hong et al.,1998).

Kharghanian proposed a method for retinal blood vessels segmentation. The method applied the Gabor filter and line operator to create a set of features for further analysis of vessels segmentations (Kharghanian *et al.*,2012).

Soares et al. presented an automatic algorithm segmenting the vasculature from retinal blood vessel images (Soares *et al.*, 2006). Classifying each pixel as vessel or non-vessel based on pixel's feature vector. They applied a 2-

dimensional Gabor wavelet transform on retinal images to enhance the vessels and filtering out the noise. The Gabor filter wavelet was chosen due to its orientation selectivity and frequency selective properties, allowing fine-tuning to maximise the vessel enhancement. The 2-dimensional Gabor wavelet was computed for orientation spanning from 0 to 170 degrees in steps of 10 degrees. The maximum response over all angles was taken. The segmentation was based on supervised classifications using a Bayesian classifier with the feature vector consisting of the pixel's intensity and the 2-dimensional Gabor wavelet transform response over angles for different scales. The wavelets were rotated and selected so that all vessels would be detected.

Kaur used an approach based on a bank of Gabor filters to segment the vessels in retinal images. Twelve banks of Gabor filters were oriented in the range of 0 to 170 degrees and used to enhance the oriented vessels image. The output enhanced image was threshold by using a grey level co-occurrence matrix (Kaur *et al.*, 2012).

Cervantes-Sanchez (Cervantes-Sanchez *et al.*, 2016) used Gabor filters and Boltzmann Univariate Marginal Distribution Algorithm in X-ray angiograms to segment the coronary. The method used the area of ROC curve as the fitness function.

Detecting linear structures is important as Zwiggelaar *et al.* investigated a number of methods to detect and classify linear structures in mammograms. The goal was to classify linear structures into an anatomical type such as vessels, spicules and ducts in (Zwiggelaar *et al.*, 2004). To evaluate the performance of different methods of linear structure detection they used the set of synthetic images designed to simulate some of the characteristics of digitized mammograms. The methods were the *Line Operator* (Dixon *et al.*, 1979), (Zwiggelaar *et al.*, 1996), (Marti *et al.*, 2001), *Orientated Bins* (Zwiggelaar *et al.*, 2004), *Gaussian Derivatives* (Karssemeijer *et al.*, 1996) and *Ridge Detector* (Lindeberg *et al.*, 1998). According to their results, the

line operator provided the best results for further experiments on real mammograms. The line operator method evaluated the average grey level along lines of fixed length at different orientations and compared this to the average grey-level of a similarly oriented square neighbourhood. The *Oriented Bins* method is similar to the line operator but was based on circular neighbourhood, and opposing sectors are used instead of the square neighbourhood and line.

Ricci suggested the line detectors method should be applied on retinal blood vessels(Ricci *et al.*, 2007). The suggested method was computationally simple but a more effective realization of the same concept inspired by the method of Zwiggelaar et al (Zwiggelaar *et al.*, 2004). The previous method was used in mammography, whereas this method was applied on retinal images, specifically on the green channel as this presented better vessel contrast. The method evaluated the average grey level along lines of fixed length at different orientations, but this time the square neighbourhood was not oriented and instead remained fixed. They segmented an image based on support vector classifications.

3.6 Derivative-based methods

Generally, vessels are brighter against the dark background; in this case, vessels appear as maxima of the image. Consequently, it may be possible to detect them by analysing the differential properties of the image. Based on the different types of properties, Agam et al. used the filters based on the assumption of the tubular model of the blood vessels and a spherical model of the nodules in thoracic CT scan images (Agam, Armato and Wu, 2005). Hence, initially, images were convolved with first-order partial derivatives and were less sensitive to noise. The algorithm was followed by multiple sets of eigenvalues due to distinguishing between nodules and vessel junctions.

Karssemeijer applied algorithm based on the Gaussian derivatives. The method convolves the image with Gaussian second derivative kernels, at

three different orientations using a Gaussian width of 0.8(Karssemeijer *et al.*, 1996).

A simple First-Order Derivative of the Gaussian (FDOG) was introduced by Zhang in order to extract blood vessels of retinal images (Zhang *et al.*, 2010). This proposes a novel extension of the matched filter which was introduced by Chaudhuri and it suggested an extra modification of the first-order derivative of Gaussian (FDOG). The vessels are segmented by thresholding the image's response to the matched filter (MF), while the threshold is adjusted by the image's response to the FDOG. The modified method helped to reduce frequent false vessel detection.

In the detection of vessels, a second-order derivative is another method that is used. The information from second-order derivative is used to characterise the local image geometry. Canny applied filters of second-order derivatives of the Gaussian function to detect lines where the convolution of that function with lines gives a maximum response(Canny, 1983).

A Hessian matrix is one of the most prevalent methods developed in the 19th century by the German mathematician Ludwig Otto Hesse (Lewis, 1991). The method is based on a square matrix of second-order partial derivatives of a multi-valued scalar function. The Hessian matrix compared to the image gradient can detect the shape characteristic of objects such as noise and tubes like structure while the image gradient response is independent of the shape. Therefore, different combinations of eigenvalues in the Hessian matrix can help to enhance points belonging to vessels in the image. Krissian *et al.* applied a corrected design of the Hessian matrix at multiple scales, that he called 'vesselness' function which gave a stronger result at one particular scale of tubular objects in the image (Krissian *et al.*, 2000).

3.7 Deformable models

Deformable models in computer vision have been extensively studied and widely used in medical image segmentation with good results. Deformable models are curves or surfaces defined inside an image that can move under the influence of internal forces, which are defined inside the curve or surface themselves and external forces that are calculated from the image data. The internal forces help to keep the model smooth during the process of deformation while the external forces help to move the model towards the boundary object for other desired features within an image. The deformable model was first introduced by Terzzopoulos (Terzopoulos, 1987).

Snake (Kc, Witkin and Terzopoulos, 1988) are one of the first classical techniques of Deformable models for segmentation, especially for the general multi-dimensional deformable model theory. Hernandez used 3-dimensional images of brain aneurysms in CTA images to segment the brain aneurysms by snakes(Hernandez, Frangi and Sapiro, 2003).

Holtzman et al. presented a novel segmentation method for thin structure segmentations of blood vessels and vascular trees. The method was based on geometric active surfaces that evolve according to geometric partial differential equations, where the method was stopped at the boundaries of the objects. The system employed was the weighted sum of three integral measurements. An alignment evolving surface to the border of the desired object. The minimal variance was calculated and measures the homogeneity inside and outside the object. A geodesic active surface used for regularisation (Holtzman-Gazit *et al.*, 2006).

3.8 Morphology Operations

Morphology is a toolset used to extract an image component in order to represent and describe the region shape; such as boundaries, skeletons and convex hulls (Gonzalez and Woods, 2008). Basic operations in mathematical

morphology work on images and with the use of a structuring element. Dilation, erosion, closing and opening are composite operators of Morphology. They operate on binary and grayscale images. The erosion operator on a binary image is used to erode away the boundaries of foreground pixels while the effect of dilation is to enlarge the areas of foreground pixels. The opening achieved by erosion followed by dilation where closing is the opposite of this. The morphology operation is an operator that processes images based on a predefined structuring element. One simple way to detect line or thin structures in an image is to design a structuring element, or filter that resembles this structure [Gonzales and Woods, 2008, Chap. 10.1].

Preserving the elongated objects in an image with morphological operations is possible by applying appropriate structuring elements in a line segment. (e.g. linear structuring element). If the object has varying directions, it would be necessary to combine the outcomes of using the structuring element in several directions.

The top-hat transform is an important technique in medical image analysis. It is a morphological operator that applies opening (erosion followed by dilation) with the structuring element. This top-hat can be used to enhance the thin structures of cilia with used of linear structures.

Spencer used the top-hat operator to detect micro-aneurysms in retinal images. The top-hat operator was used with a linear structuring element which first took the vasculature structure as the interest and then subtracted it from the original image to produce an image containing only circular objects of microaneurysm (Spencer *et al.*, 1996). A linear structuring element was used whose length was greater than the diameter of the largest red lesion, not too long and small enough to fit within all of the vessel structures.

The morphological top-hat is useful when there is a variation in the image background. Where applied it can detect the local variation of the

background. Eiho 1997 applied the top-hat algorithm to enhance blood vessel images (Eiho and Qian, 1997). Choosing the structuring element size is important. In this case, the structuring element size was set slightly larger in size than the diameter of the vessel.

Zana et al. described a different method of morphology for detection of vessel-like objects in 2-dimensional images. They defined blood vessels as a bright pattern, piecewise connected and locally linear. The method was combining a rotating linear morphological operation followed by a cross-curvature analysis. The aim was to segment the vessels from the background (Zana and Klein, 2001).

Sun applied the combination method of Gabor wavelets filters and the top-hat technique on a real-time angiogram. The top-hat transform was proposed to enhance the local contrast of a coronary angiogram. The size of the structuring element for each pixel in the top-hat was estimated using the 2-dimensional Gabor wavelet. The Gabor wavelet was applied at multiple scales and orientations; the maximum response of different orientations and scales was calculated (Sun and Sang, 2008).

Due to the possible low contrast between the background and small blood vessels in the image, Kang and Li proposed an algorithm based on a degree-based fusion algorithm for coronary angiograms (Kang *et al.*, 2013). The proposed method initially used to enhance the original images. They believed the cross-section shape of the vessel is approximated as round and the vessel greyscale profile approximated a Gaussian curve. Thus, the top-hat with a round structuring element used. The coronary arteries were detected from two enhanced images through the degree method. Lastly, two extracted vessel images were fused.

3.9 Classification

Supervised: The focus of this section 3.9 is to describe the various image segmentation techniques that use supervised learning involved in the area of thin, elongated structure of medical images. This section will provide a brief overview of image classification techniques used in this area of medical image analysis.

Classification methods are pattern recognition methods, their aim being to extract features from pixels/objects in the image and output class labels. Classifiers produced using supervised methods have been trained on manually labelled data. Once the classifier has been trained it can then be applied to the task of labelling (e.g. segmenting) new data.

The K Nearest Neighbour classification (KNN) is the simplest classifier but works well in practice. The goal is to find the class labels for the new points. When a prediction is required for a new data, the KNN algorithm will search through the training dataset for the k-most similar instances. The most similar instances (based on the feature vector) is summarized and returned as the prediction for the unseen instance. This algorithm actually uses a similarity measure or distance function to find the nearest cases to a new case. For classification of a new sample, its k closest neighbours must be found. Euclidean distance (Duda, Hart and Stork, 2012) is mostly used for defining what closest means, but there are other distance measures have been used as well. An object is classified by a majority vote of object neighbours (Cover and Hart, 1967). The main advantage of KNN is simplicity but the disadvantages are computation time (because it uses internal competition between data to make a predictive decision), and it requires more memory. There are several methods to overcome the memory limitations which are structure based. Bhatia presented the survey of a variety of algorithms developed on the basis of KNN (Bhatia, 2010).

Nancy proposed the k-nearest neighbour algorithm for the segmentation of retinal blood vessels, based on a feature vector that consists of the largest eigenvalue, gradient magnitude and green channel of the image intensity (Salem and Nandi, 2006). The aim of the first two features was piecewise linearity and parallel edges. Results show that classification with these three features significantly reduces the processing time compared with the original method that used 31 features (Niemeijer *et al.*, 2004). The produced result of the Gaussian filter and the original grey level of green channel images (31 features) were inputted into the K nearest neighbour classifications (Niemeijer *et al.*, 2004). KNN will be one of the method apply on the thin structure of cilia. This can help to separate the thin structures of cilia from non-cilia. The KNN algorithm strategy and the affected of the results will be shown in chapter4.

Bayesian decision theory is a fundamental statistical pattern classification algorithm, based on Bayes' theorem (ÇELEBİ, 2016). It simply describes that there is no dependency between a particular feature of a particular class.

Soares used the Bayesian algorithm, in which class likelihoods were described as a linear combination of Gaussian functions. Soares *et.al* created a feature vector for individual pixels from image pixel's intensity and from the results of applying a 2-dimensional Gabor filter at multiple scales and various orientations (Soares *et al.*, 2006). Ricci applied the line detector on the green channel of retinal images which was used in mammography images. The method evaluated the average grey level along lines of fixed length at different orientations. The average value of short orthogonal line was calculated. Results of these two values along with pixel's intensity value were calculated to create a feature vector used by support vector classifications (Ricci and Perfetti, 2007).

Kharghanian applied Gabor filters and line operator as two sets of input features for using two classifiers: Bayesian and SVM to classify retinal blood vessels. The set of feature vectors consisted of; pixel intensity of an image,

four features of Gabor filter in different scales, two features of line operators (Kharghanian and Ahmadyfard, 2012).

Unsupervised, clustering algorithms performed the same function as classifier methods without any training data. Thus, they are named unsupervised methods. K-means and the fuzzy C-means are commonly used clustering algorithms.

Fuzzy C-means is one of the most prevalent methods involving feature analysis. This clustering algorithm (FCM), allows the pixel to belong to more than one cluster, it was first presented by Dunn (Dunn, 1973). Because some data belonged to multiple clusters, it was impossible to combine them into one cluster. Therefore, Bezdek revised the method several times to improve it (Bezdek, 2013).

Ahmadi proposed a fuzzy C-mean (FCM) algorithm in conjunction with genetic algorithms (GA) and applied them to CT scan images of the liver to detect vessels. The CT images convolved with Gaussian low-pass filters to eliminate noise. Then the combination of fuzzy C-mean and GA performed the segmentation by feeding a FCM with the random values of the core centres (chromosomes), (Ahmadi *et al.*, 2016).

Yang applied fuzzy C-mean based on the vascular feature. His idea was that fuzzy cannot give an accurate vessel segmentation result. Therefore, the algorithm was based on the combination of the tubular structure information and grey value scale information to segment cerebral vessels from MRA images (Yang *et al.*, 2015).

Kande used matched filter to increase the contrast of the blood vessels against the background, then employed spatially weighted fuzzy C-mean clustering based thresholding in retinal images to segment the vessels (Kande, Subbaiah and Savithri, 2010).

3.10 Conclusion and discussion

In this chapter, several methods for detection of thin structures in different types of biomedical images were discussed. No method was found to have applied by other researchers on elongated structures of the cilia. Hence, the literature review is more based on general thin structures such as blood vessels, fingerprints etc. From all different methods of thin structures enhancement, and detection, the interest is in methods that can segment and distinguish the thin structures of vessels and other structures for further quantitative analysis.

Blood vessels with a low intensity often are encapsulated by the noise in the background. However, this can be a problematic task due to the background noise as required more attention from the researchers. There are other problems with vessel detection which are false positives of camera artefacts and motion artefacts.

The most popular methods were used around for thin structures detection were based on directional filters such as matched filtering and Gabor filters. These filters rotated in order to detect vessels in different directions. Also, the outcomes of these filters were used as features along with intensity.

The morphology operation was another method for detection of vessels. The results showed that morphological operators were able to segment linear structure well in different orientations to detect 2-dimensional structures in a highly noisy background.

The described methods above have shown a wide range of choices for particular problem-solving. The selected method depends on the type of application and its constraints. Another important feature to decide upon is if a method should be automated or semi-automated.

From all different methods of thin structures enhancement and detection, the interest is in methods that can easily segment and distinguish the thin

structures of cilia or vessels and other structures for further quantitative analysis. Moreover, the interest is in the method that is computationally inexpensive, easy to apply and precise.

The conclusion is, every technique performed well in a particular field under the particular circumstance and must be considered with these parameters in mind.

Chapter 4 Cilia Detection Methodologies for Segmentation Process of SEM Cilia Images

4.1 Introduction

THIS chapter focuses on applying various methodologies to detect cilia in SEM images and determining the most suitable algorithms to detect the thin cilia structure. As with any other image processing methodology, segmentation is crucial to analyse the results, which may be used in a wide range of applications varying from the medical to any industrial cases where they are needed.

This chapter explores the creation of various automatic detection methods of cilia. As discussed in chapter 2, cilia are hair-like structures that hang from the surface of the cell. Their images were captured by scanning electron microscope devices and the images are stored and then segmented. Segmenting objects from SEM microscopic images is challenging in many bio-imaging applications due to background noise and automated techniques are often susceptible to this. In these approaches, cilia segmentation was performed using different algorithms to enhance their linear structure. The result of segmentation then used to quantify cilia with respect to length and cilia number. A semi-automatic algorithm was used on overlapping cilia to measure their length. The performance of the algorithm was then evaluated by comparing results derived from using various methodologies, which discuss in the following sections in the segmentation results with the manual ground-truth results. Local morphology features such as length measurements using various length measurement methods were

investigated using high-resolution images of the cilia. The nodal images were then used to count and evaluate the number of cilia.

4.2 Background

The proposed algorithms were adopted from existing common approaches of the thin structure segmentation applied on a variety of the biomedical images, followed by analysing the segmented cilia as documented in the literature review (chapter 3).

Spencer used the top-hat operator with a linear operator to detect micro-aneurysms from fundus images (Spencer *et al.*, 1996). Canny applied filters of second-order derivatives of the Gaussian function to detect lines where the convolution of that function with lines gives a maximum response (Canny, 1983). Soares *et al.* applied a 2-dimensional Gabor wavelet transform on retinal images to enhance the vessels and filtering out the noise (Soares *et al.*, 2006). Salem proposed the k-nearest neighbour algorithm for the segmentation of retinal blood vessels, based on feature vector consists of, largest eigenvalue, gradient magnitude and green channel of the image intensity (Salem and Nandi, 2006). These algorithms applied to high resolution cilia images to segment the cilia. All algorithms were evaluated against ground truth (manual labelled images) and the best one was chosen according to the ROC curve.

4.3 Materials

A dataset of cilia contains high resolution and nodal cilia images of normal and abnormal microscopic scans. To evaluate the proposed methods, algorithms were applied to both cilia images of normal and abnormal datasets. In order to measure the length of the cilia, high resolution images were used. Cilia nodal images were used to calculate the number of cilia

within a node. These images were captured by 3 different observers with experience in cilia biology.

All images contain a white bar showing the image information. This was removed (cropped) by applying the mask without changing the size of the image and alter any other information from original images before further segmentation analysis.

High resolution cilia images - These cilia images have a resolution of $2\mu\text{m}$ including normal and abnormal cilia which were then used to segment and measure the cilia length.

Nodal cilia images - These images have a resolution of $10\mu\text{m}$ contain the whole structure of the node with normal and abnormal projected from the cell. They were used to segment and to count the number of cilia on the nodes.

A SEM device was used to capture images with a resolution of 768×1024 . Data were collected, prepared and processed at MRC Harwell from mouse embryonic nodes which took place at Kingston University London. The dataset contains 6 high resolution images (3 normal + 3 abnormal) and 6 nodal images (3 normal + 3 abnormal).

The pixels in these images were labelled manually as either cilia pixels or background pixels to create the ground-truths. This was performed by author knowledge and all cilia pixels were marked. Manually labelling cilia pixels were selected to create a ground-truths for segmentation evaluation of algorithm by using Paint editor software.

4.4 Cilia Detection Framework

All the algorithms discussed in the following sections were developed and evaluated using MATLAB software (2015b). The step-by-step process flows of all the algorithms are illustrated in Figure 4.1. The initial step is the preparation stage, which involves removing the white bar that shows the

information of the image without changing image structure in order to ensure the system's robustness, see figure 2.1. This procedure is common for all algorithms. Each algorithm starts with a pre-processed initial stage to eliminate the noise and to remove the background. Various cilia enhancement techniques with linear structures were then used to enhance the cilia followed by the cilia segmentation in individual data sets. A post-processing technique is applied in all algorithms on resultant images to remove small and non-cilia objects.

The post-processed images now contain cilia images without any noise paving the way to then measure the length of cilia using length measurement algorithm and to count the number of cilia. However, the post-processed images result contains the overlap cilia and non-overlap cilia and the overlapping cilia are then removed from the dataset. The non-overlap cilia and overlap cilia measured in a different way but the results cover both.

The original images of the overlapping cilia were measured with the semi-automatic algorithm. The boundary lines of the selected cilia images are then marked/selected resulting in a semi-automated process. The semi-automated length measurement algorithm was using best fit ellipse on the data set which has overlapping cilia images thereby aligning the results with the rest derived by using non-overlapping cilia images.

Figure 4.1- 4.3 show an outline flow chart of the system architecture. Figure 4.1, illustrates the flow chart of the high-resolution images, the algorithm first enhanced and segmented images and eliminated the false objects. Then the segmented image was used to measure the lengths of the cilia. Figure 4.2 shows the step by step of the semi-automatic algorithm applied to measure the overlapping cilia length. Figure 4.3, shows the stages involved in nodal cilia images. The output of all the segmentation algorithms was evaluated against the ground truth and results shown that the mathematical morphology

with used of the linear structure was the best method to segment cilia. Then the nodal cilia segmented images were used to count the number of cilia.

All algorithms developed were implemented in MATLAB version 2015b using the Image Processing and Statistics Toolboxes. All the results in this thesis have been generated from the MATLAB.

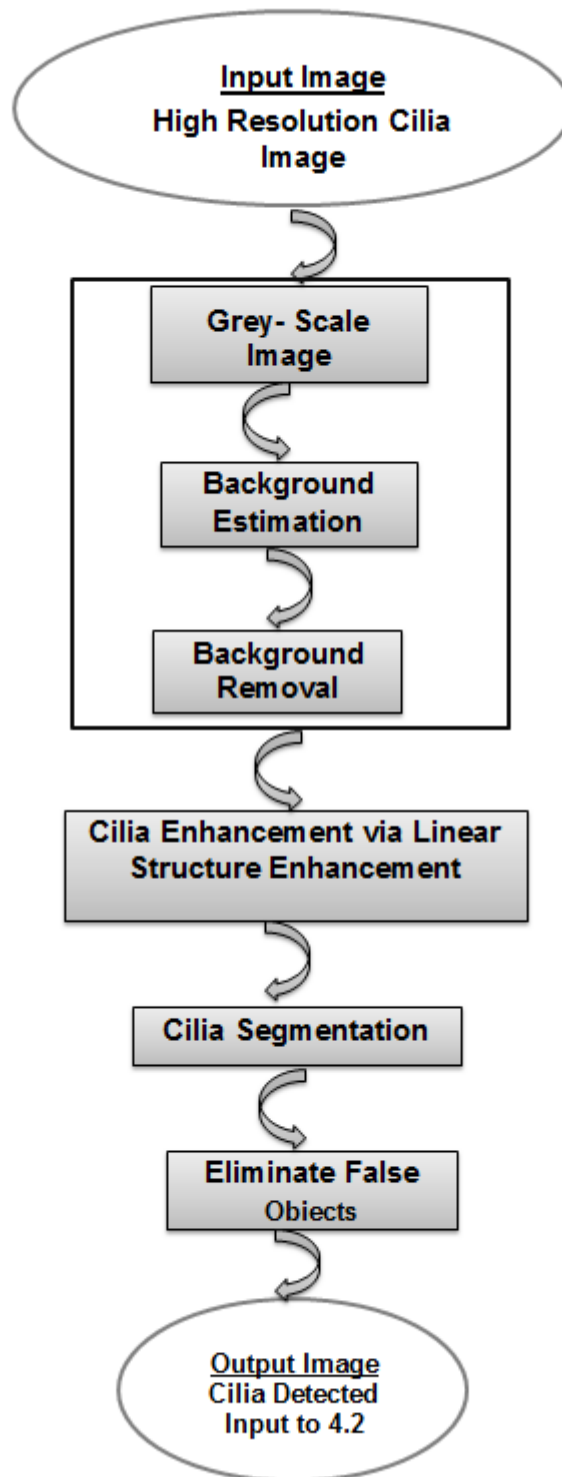


Figure 4.1: High Resolution Images Architecture Segmentation

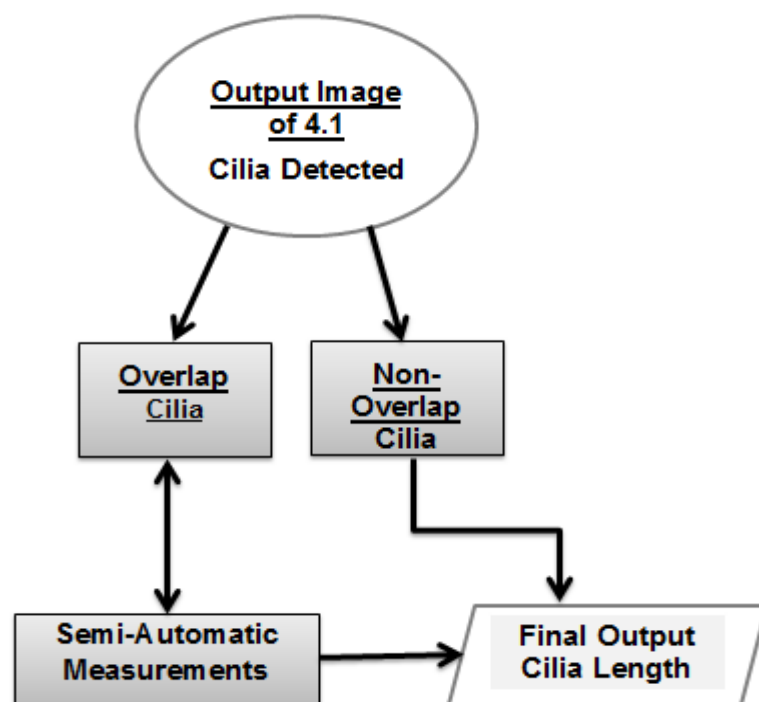


Figure 4.2: Flow Chart for semi-automatic measurements

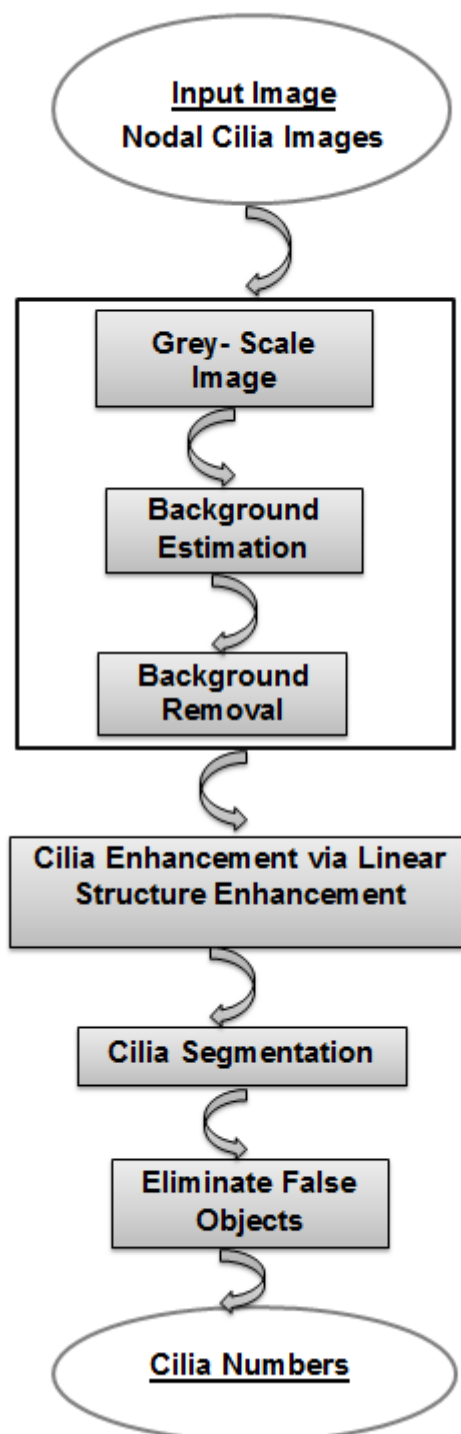


Figure 4.3: System Architecture for Nodal images

4.5 Methodologies for Cilia Detection

4.5.1 Methodologies

SEM images can reveal the structure of cilia with a high level of resolution. Accurately segmenting of the cilia images is an important task in order to analyse the quantification of cilia. Fully automated techniques are often susceptible to noise and challenging to develop, because of natural and artificial noises in the images and the natural movement of objects during the capturing process in microscopic images. Overlapping and bending cilia can confound the profile model. These properties had to be taken into account when defining the algorithms/methodologies. Thus, the semi-automatic algorithm used to assist user for precise segmentation. Having discussed the properties of the cilia images, the next section discusses the methodologies used to detect them.

In this section, multiple approaches were investigated to detect the thin structure of cilia. These methods were performed prior to pre-processing technique. The enhancement methods studied in this thesis are as follows: Mathematical Morphology operations, Gabor filters and Gaussian filters (all with the aspect of linearity). These methods used global thresholding. An additional approach used on the information derived from the above three approaches, that used along with the use of a KNN classifier. The approach proved to be the most suitable was evaluated from ROC curves of the segmentation results.

4.5.2 Pre-Processing Stage

The image details were visible as text overlaid on the bottom corner of the image and thus had to be removed. This was achieved by an interactive

polygon tool “roipoly” in MATLAB software. This tool returned the mask the same size as the original image. The purpose of this was to stop the bar details interfering with the decision of segmentation and quantification measurement process. Then cilia images were converted to grayscale images using the equation 4.1(Slezak *et al.*, 2010) which is based in MATLAB:

$$(0.29 \times R) + (0.58 \times G) + (0.11 \times B)$$

Equation 4.1

Noise in part can cause pixels with random variation intensity and are visible as grains in the images (Kaur *et al.*, 2015). Non-uniform illumination is referred to as shade and intensity inhomogeneity and is one of the main challenging tasks in the field of medical imaging. Therefore, before applying cilia enhancement techniques to cilia images, shade correction technique (Niemeijer *et al.*, 2005) to correct/remove the non-uniform illumination from images was performed as the highest priority. Then background approximation was gained by applying a median filter. The filter mask size was set empirically to 9 x 9 and 30 x 30 pixels for nodal cilia images and high-resolution images respectively. These filter sizes were chosen according to the magnification of the image and width of the cilia, to ensure the cilia structure were preserved. The shade correction was then performed by subtracting an image background from a grayscale image.

Figure 4.4 illustrates an example of removing the non-uniform illumination. It is clear that the low-frequency components have been removed.

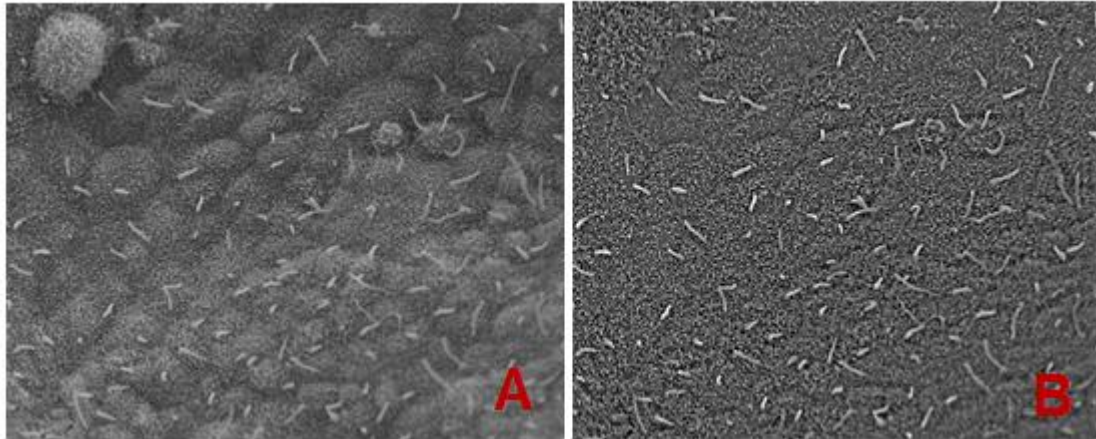


Figure 4.4: Image A, Is an original image. Image B shows the result of shade correction. Low-frequency components have been removed.

4.5.3 Cilia Enhancement

Four different enhancement methods were applied to images of elongated cilia. Gaussian, Gabor, mathematical morphological operation with a global threshold and a K-nearest neighbour classification approach were applied. The mathematical morphology operation was found to be the appropriate method based on the results which are discussed and illustrated in a result section. Note, all listed methodology parameters in section 4.5.3 are in respect to the application to the high-resolution cilia images.

The segmented results of the algorithms are plotted using receiver operating characteristic (ROC) curves. ROC curves are plots of true positive fractions versus false positive fractions for varying thresholds were compared successfully.

4.5.3.1 Gaussian Based Segmentation

Cilia may be considered as piecewise linear segments. Grey-level profile of the cross-section of the cilia is approximated by a Gaussian-shaped curve.

Therefore Gaussian filtering was applied on cilia images which were inspired by Chaudhuri (Chaudhuri *et al.*, 1989) method. Chaudhuri introduced the algorithm to detect piecewise linear blood vessels in 2-dimensional retinal images. Figure 4.5 shows the zoomed in image of different cilium from the panel with different lengths and orientations.

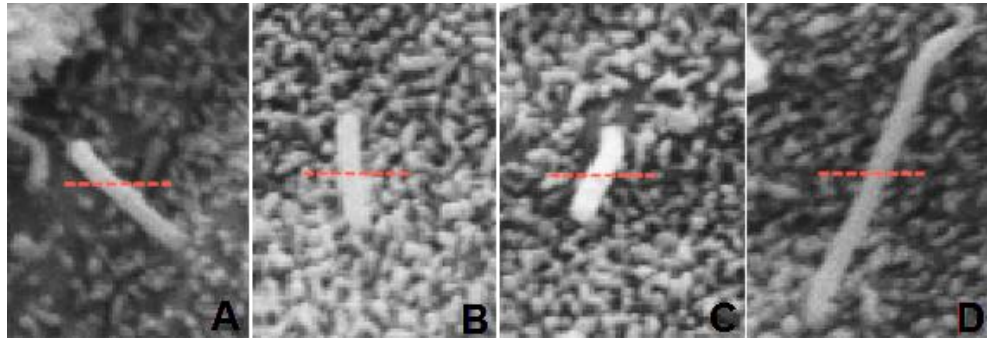


Figure 4.5: It shows a different cilium with different lengths and orientations.

As shown, in Figure 4.6, the grey level profiles of the cross-section of cilia are related to zoomed in image of figure 4.5. It was observed that the intensity profile of cilia was varied and it may be approximated by a Gaussian curve.

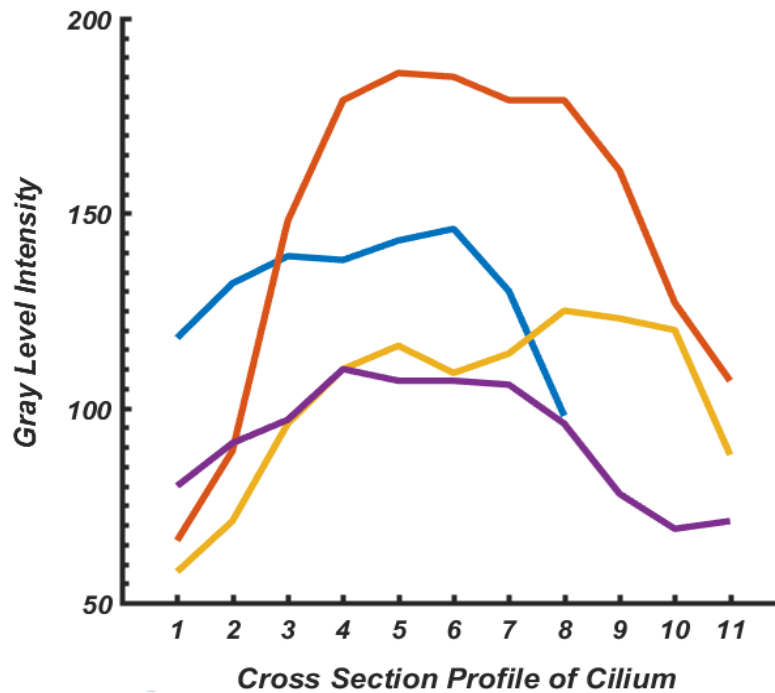


Figure 4.6: The grey -level (brightness) profiles of the cross-section of several cilia from the image of figure 4.3. The cilia have different intensities. Each curve represents the cross-section of each cilium.

Gaussian filters were used in order to enhance cilia at different scales. The aim of using the Gaussian filter is to reduce the level of noise and enhance the cilia from a background in the images, to improve the results of the following processes and stages. This Gaussian filter was different from the standard isotropic Gaussian filter; in this method, a 1-dimensional Gaussian function was repeated a number of times and stacked to make the length of the filter which gave the filter an aspect of linearity. The Gaussian filter was convolved with cilia images, typically to reduce image noise and enhance the elongated structure of cilia. The sigma value of Gaussian filter was chosen upon empirically from a range of values. In order to detect the true length of each cilium, the value of sigma was chosen based on the widths of the cilia. The widths of the cilia are found to lie within a range of 6 - 9 pixels (0.3 – 0.4 μm) in high resolution images. Therefore the value of sigma chosen is 1, in order to pick up the width of the cilia efficiently.

The filter length was chosen 19 pixels empirically which gives it an aspect of linearity. The Gaussian filter in 1-dimensional is defined below in equation 4.2, where δ is a standard deviation of the distribution.

$$G(X) = \frac{1}{\sqrt{2\pi\delta^2}} e^{\frac{-x^2}{2\delta^2}}$$

Equation 4.2

Cilia are projected in different orientations at an angle θ ($0 \leq \theta \leq \pi$). Therefore, 12 different kernels with an angular resolution of 15° were spanning in all possible orientations. These 12 sets of kernels are applied to the cilia image and the maximum response among them is selected/chosen. This is repeated to the whole dataset of the cilia images resulting in enhanced cilia images.

This was followed by applying the global threshold to create a binary cilia image. These objects matched the shape of the filter. Post-processing required identifying and subsequently eliminating the false detections. Figure 4.7 and 4.8 illustrates the set of Gaussian filters applied on cilia images.

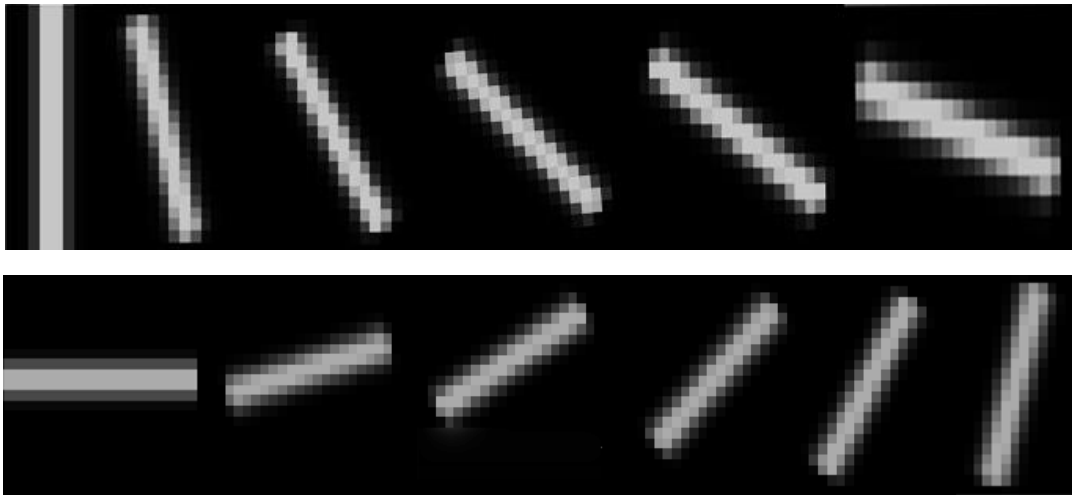


Figure 4.7: 12 sets of the Gaussian filter with an aspect of linearity rotated with an angular resolution of 15° .

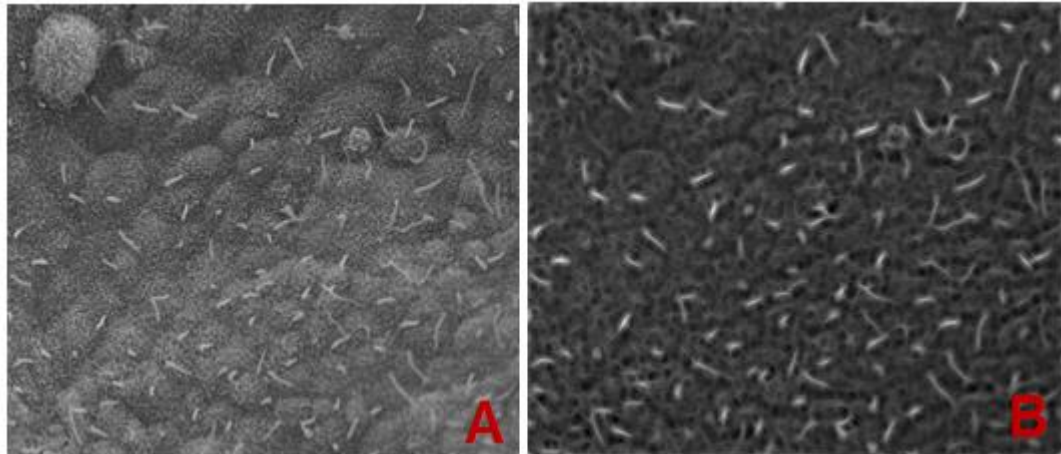


Figure 4.8: The image A is an original image of the cilia. The image B illustrates the results of the enhanced image applied by the Gaussian filter.

4.5.3.2 Gabor-Based Segmentation

The Gabor filter is an important algorithm that plays a role in many application areas and it was applied here for the purpose of enhancing the thin structure of cilia in noisy images due to directional selectiveness and well tuning to specific frequencies. It is an essential algorithm to enhance multi-oriented thin objects and filtering out the background noise. A 2-dimensional Gabor filter is achieved by modulating a sinusoid with Gaussian kernel function. The linearity aspect of the filter in the Gabor was provided by the sinusoidal. The Gabor filter used sigma size equal to 3, lambda 15.5 and gamma 1 which they were driven empirically. 12 different Gabor filters with an angular resolution of 15° orientation applied to high resolution cilia images to enhance the cilia. The maximum response of overall angles was taken. These resultant enhanced cilia images then went through the global thresholding process resulting in binary cilia images. The binary cilia images are created based on the best operating point on visual analysis process which will be discussed in the result section. Figure 4.9, demonstrates 12 Gabor filters in 15° angular resolution. In figure 4.10 image, A is an original

image and image B, demonstrates the result of the cilia enhancement by Gabor filter.

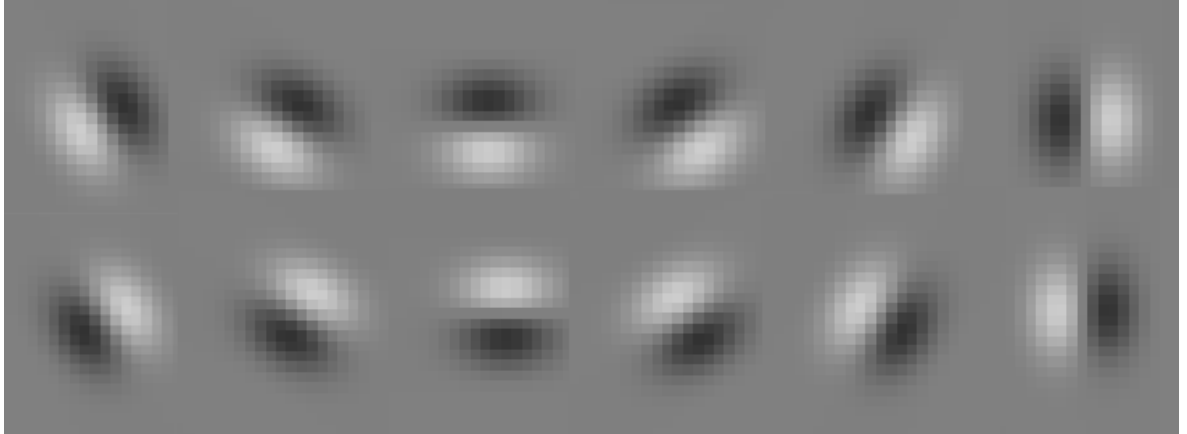


Figure 4.9: This image demonstrates the Gabor filters rotated in 12 directions of 15° .

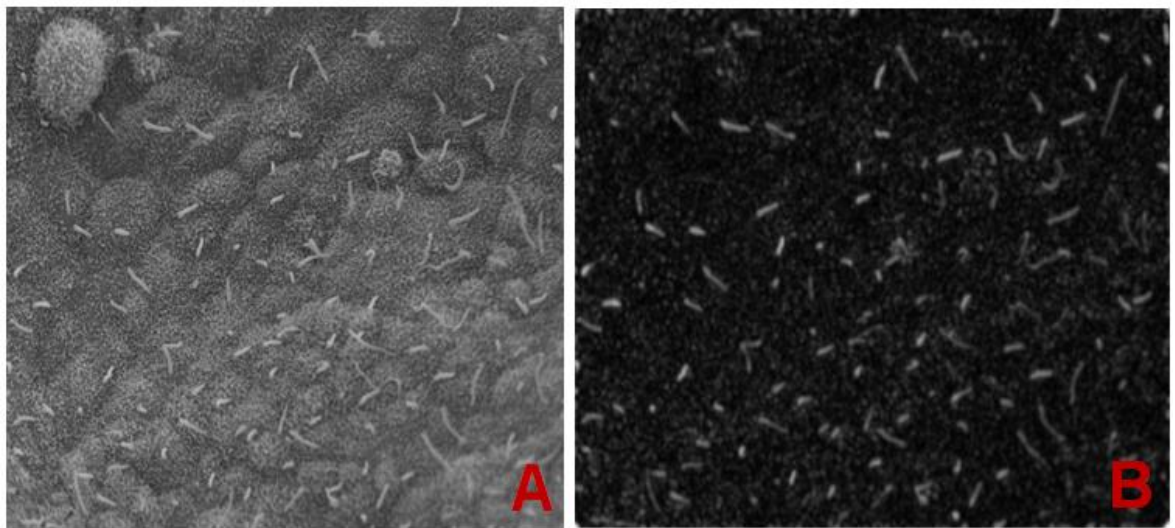


Figure 4.10: The image A is an original image of the cilia. The image B illustrates the results of the enhanced image applied Gabor filter.

4.5.3.3 Mathematical Morphology Operation Based Segmentation

According to the literature review, one of the approaches to enhance thin structures used mathematical morphology operation with linear structuring elements (SE) in many applications. The opening of an image f is simply the

erosion of an image by structuring element $\$$, followed by the dilation of the result by structuring element. The opening of an image is defined by an equation 4.3 where f is an image and $\$$ is a structuring element.

$$f \circ \$ = (f \ominus \$) \oplus \$$$

Equation 4.3

Once the background image is estimated and removed, cilia images are ready for further enhancement. Cilia enhancement was performed by employing a basic mathematical morphology operation using a linear structure, applied at different orientations to the cilia image dataset. This process again involves applying linear structure oriented at 12 angles with 15-degree angular resolution. As cilia are considered as piecewise linear, a linear structure element of the length of 19 pixels was applied to perform the morphological operations. The length of the structure element was driven empirically. In each of the 12 images in different orientations, only those parts of the cilia in which the linear structuring element can fit, remain. By taking the maximum pixel value at each pixel location in all 12 images which detected cilia selections of all orientations, with little noise present. Therefore objects smaller than the linear structuring elements are diminished in intensity and those that can fully contain the structuring element are enhanced in intensity. The results have shown an image containing the mainly elongated structure of cilia of all orientations. Binary segmentation created by global thresholding the enhancement image that will be described in the result section. In figure 4.11 image A is an original image with cilia, image B illustrates the results of the enhanced image created by the Mathematical Morphology operator method.

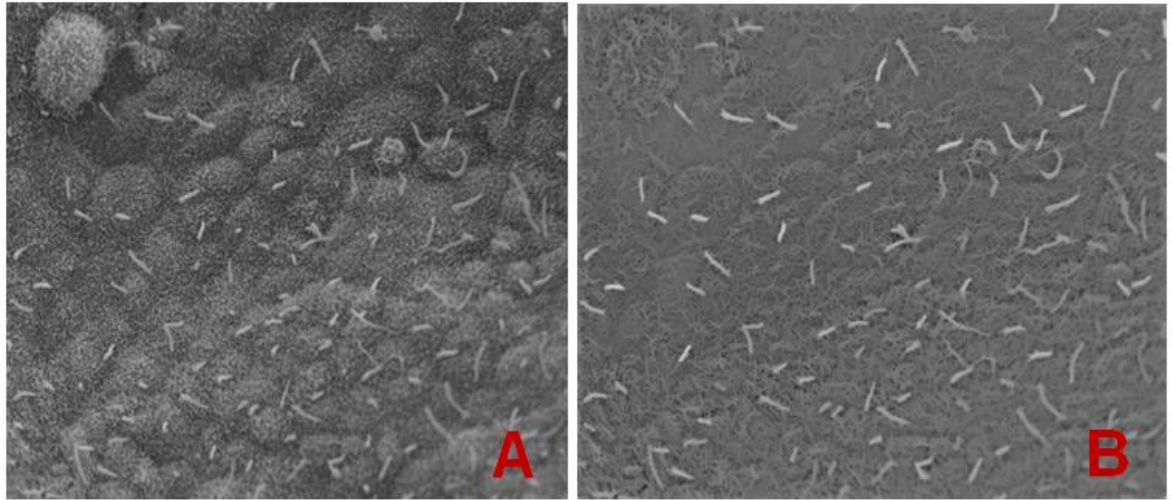


Figure 4.11: Image A is an original image of the cilia. Image B illustrates the enhancement result applied by Mathematical Morphology Operator.

4.5.3.4 KNN Classification Used for Segmentation

Nancy used scale-space features and k-nearest neighbour classifier for segmentation of retinal blood vessels (Salem and Nandi, 2006). K-Nearest Neighbour (KNN) Supervised Nearest Neighbour classification is one of the simplest classifiers, in fact, it is easy to understand and implement the algorithm but it works well in practice. The algorithm used pixels from 2 training images consisting of one normal and one abnormal image, and pixels from 4 testing images of two normal and two abnormal cilia images. Predictions for the test data were based on the nearest neighbours from the training data using Euclidean distance. For classification of a new sample, its k closest neighbours must be found. The algorithm basically relies on the distance (e.g. Euclidean distance) between feature vectors. If there are two points q (q_1, q_2, \dots, q_n) and a point p (p_1, p_2, \dots, p_n) the Euclidean distance between the points q and p is defined as the equation 4.4:

$$d(p,q) = \sqrt{\sum_{i=1}^n (q_i - p_i)^2}$$

Equation 4.4

The K- nearest neighbour classification phase classifies the cilia images into cilia pixels or background pixels. This method using a vector of 5 features derived from properties of cilia images. The method was aimed to classify cilia and non-cilia for cilia segmentation. The details from five features used to form training data:

1) Grayscale pixels intensity of cilia image

Convert pixels of cilia image to grayscale image, explained in 4.5.2.

2) Shade corrected pixels intensity

Subtracted median filtered output from the grayscale image, also explained in 4.5.2.

3) Gaussian filter output

This feature was selected based on the output of the Gaussian filter and is elaborated in the section 4.5.3.1.

4) Gabor filter output

This feature was selected based on the output of the Gabor filter as explained in the section 4.5.3.2.

5) Mathematical Morphology operator output

This feature was selected based on the output of the Mathematical Morphology operator as explained in the section 4.5.3.3.

These features were applied to cilia images to prepare training data. The classification separates the testing sample into cilia and non-cilia pixels by

calculation the closest Nearest Neighbour based on Euclidean distance. The method was chosen for classification purpose due to its simplicity.

The main drawback of KNN is the competition in searching the nearest neighbours for each sample. Due to the fact that there are lots of elements which are required in finding the distance between each element to the element that needs to be classified so for the larger dataset it could result in being a problem. As a consequence; to reduce a complexity and running time training data was produced by the random selection of feature vectors for 500 cilia pixels and 500 non-cilia pixels.

K is the number of instances (nearest training samples) that the classifier considers for determining the class label of the test sample. It is very important to select the correct K value. A large K value can reduce the overall noise whereas a too large K value could result in picking up unwanted samples from outside the local region (in respects to feature space). Hence, K is required to be small enough to ensure it picks up only nearby samples. Therefore, choosing an optimal K is vital. In this research of cilia classification, K is represented as the square root of the size of the training (Hassanat *et al.*, 2014). Also, it is favourable if K is an odd number. Based on this, the value chosen for K was 31. This will define the nearest neighbour region.

Now that we have discussed K values, the predictions can be discussed. The KNN predictions are commonly based on a majority vote. Therefore, for a test sample (i.e. test pixel) the classifier searches for the 31 nearest neighbours in the training data and identifies their class, the class with the most votes is awarded as the class of the test sample. The majority vote will create a single operating point; various operating points will be required for the creation of the ROC curve (as will be discussed in the results section). This can be achieved by varying the number of votes for a particular class that is required to achieve that class label for the test sample. This starts at

zero and then incrementally increases by 1 until $k+1$ is reached, hence producing 32 operating points.

Figure 4.12, shown, KNN algorithm applied on abnormal cilia image (A) and normal cilia image (B). In this figure, image (C) and (D) illustrates the binary cilia image resulting from the KNN algorithm.

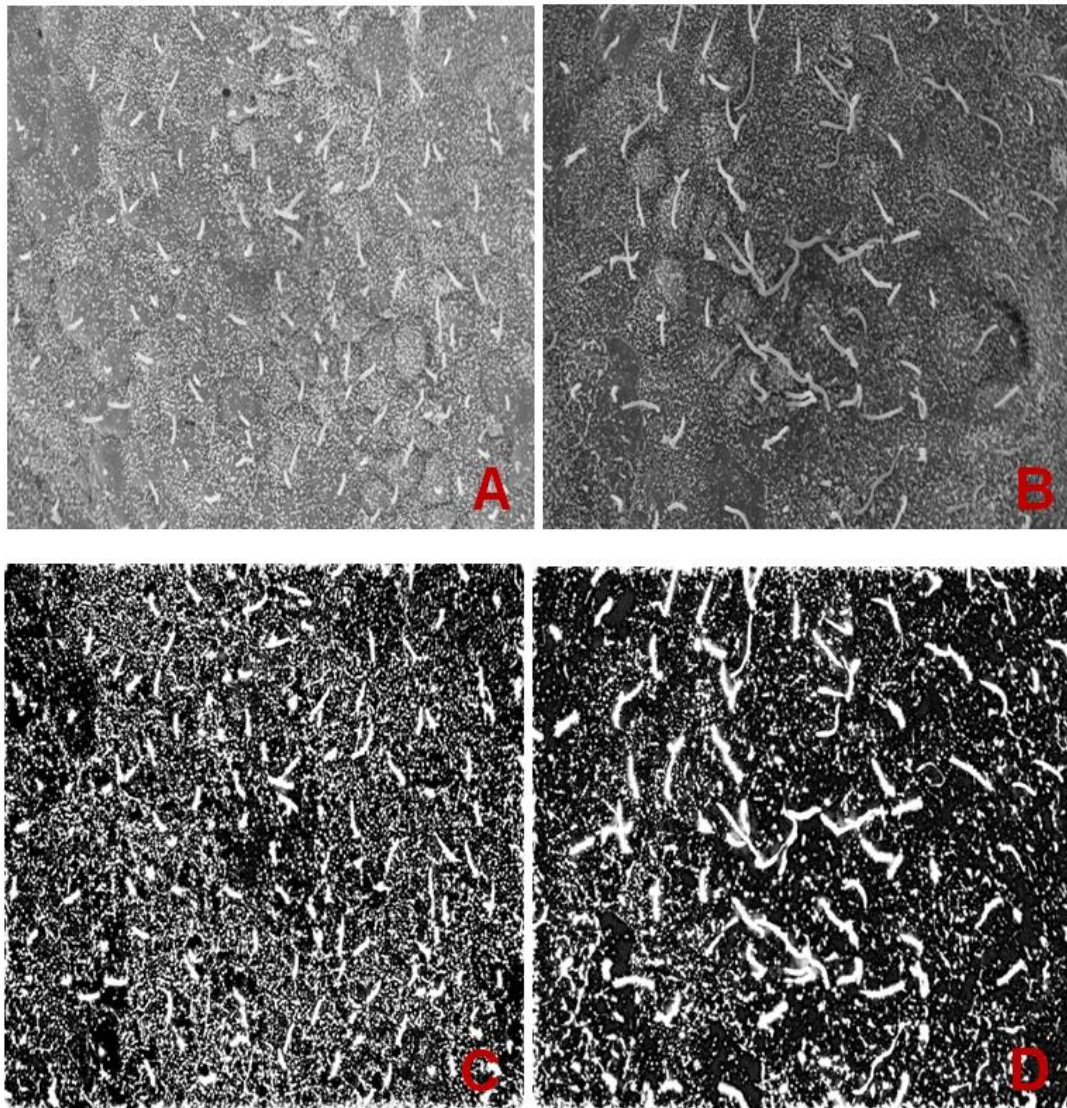


Figure 4.12: Image A and B is original abnormal and normal cilia images respectively. Image C and D illustrate the binary cilia images from K-NN, $k=31$. The image C is a result of K-NN corresponds to image A. The image D is a result of K-NN corresponds to image B.

4.5.4 Post Processing Stage

Before the post-processing stage, the enhanced images go through global thresholding or classification resulting in binary cilia images which are then used for further quantitative clinical purposes. However, it is important to have a true length and a true number of cilia for further quantification analysis of cilia images. To stop noise interfering with the results it is essential to remove them from the binary image. Likewise, objects that are connected to the borders of the binary images were required to be ignored and removed. Therefore post-processing was applied to the cilia binary images. This stage was included to remove all connected components that have a smaller area of pixels than a specific size from binary segmented cilia images. In post-processing stage a mask was applied to the images to eliminate the regions that were touching the border.

Once post-processing was performed the cilia images are then labelled. Overlapping cilia are removed from the labelled image by visual assessment for further quantification assessment. The non-overlapping cilia are measured automatically by applying different length measurement methods. Length detection of overlapping cilia were refined by the use of the semi-automatic method as explained in earlier sections of this chapter.

4.6 Cilia Length Measurements Methodology

A variety of length measurements were used to measure the real length of the cilia. The approaches proposed were, Major Axis, Perimeter, Extrema, find the area of skeletonisation and Extrema_centroid. They are the different types of measurement techniques of image region properties commonly used and available in MATLAB software. Chain code boundary-based method was also used to measure the length of the cilia. Proposed methods return a scalar value that specifies the length in pixels. Results were converted to

micrometre. Table 4:1 illustrates all the different methods. The results will be shown in 4.8.2.

Extrema	Returns an 8-by-2 matrix that specifies the extreme points in the region. Find two end points and calculate the Euclidian distance from two points.
Major-Axis	Returns the major axis of the ellipse that has the same normalized second central moments as the region.
Perimeter	Specifies the distance from the boundary of the region divided by 2.
Extrema_centroid	Uses 'centroid' to specify the center of the mass. Uses the concept of the 'Extrema'. Identified the Euclidian distance; from top-left point to center, centre to bottom-right point and add two distance together. Calculates the Euclidian distance from centre points to two end points.
Chain code	Gives Freeman chain code 8-connected representation of a boundary
Skeletonisation	Calculates the number of pixels in skeletonisation of the cilia.

Table 4.1: Cilia length measurement methods

4.7 Measurement of Overlap Cilia Images

Cilia images were captured from microscopic SEM devices. As shown, in, figure 4.13, red arrows depict different examples of cilia touching/overlapping. When two single cilia overlap, they appear as one long cilium. However, this causes problems when measuring the length of each cilium.

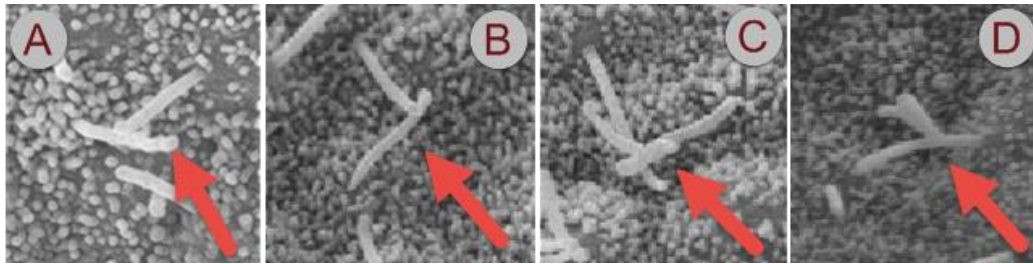


Figure 4.13: Cilia overlaps, Images of A and B showed cilia touch each other. C shows three cilia are overlapping. D shows two cilia are overlapped.

Therefore, the author used a semi-automatic algorithm to measure the lengths of the cilia to avoid any miss-detection. Then the objective of this subsection is to measure the length of the touching/overlapping cilia by applying the semi-automatic algorithm.

The proposed method isolates the touching/overlapping cilia to measure their individual length. A fit ellipse function approach is used to estimate the best fit to an ellipse from a given set of points. This concept of fit ellipse function is used for the refinement stage of length measurements. This was performed in high resolution cilia images of normal and abnormal cilia. For the semi-automatic algorithm follows these stages as listed below:

- 1) *User intervention is required to performed local cropping around cilium by using the “ginput” function in MATLAB software.*
- 2) *Next, select/choose boundary points on each side of the cilium.*
- 4) *The algorithm finds the best fit to an ellipse for the given set of points.*

5) Next, the long axis of the best fit ellipse is used to measure the length of the cilium.

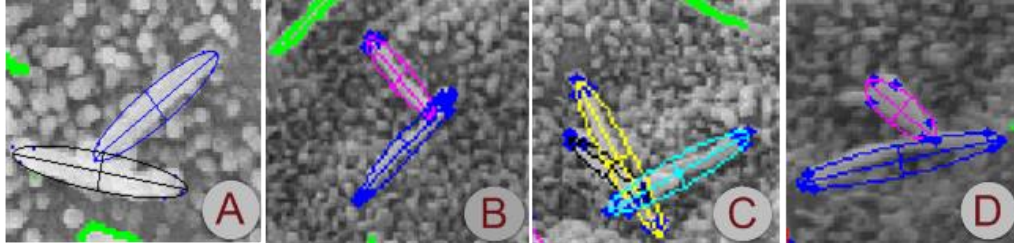


Figure 4.14: Results of the proposed method on overlap cilia of Figure 4.13.

In figure 4.14, demonstrates the performance of the semi-automatic system of overlap cilia. Results showed lengths measurements of different overlap cilia. A, B, C and D illustrate the plotted ellipsoidal with the long axis of ellipsoidal in overlap cilia. The length of the long axis of ellipsoidal in micrometre calculates the cilia length of the individual cilium.

4.8 Experimental Evaluation

4.8.1 Measuring Performance

The available ground-truths can assist to investigate the performance of the segmented results from using the above algorithms. The performance of the segmented results may be evaluated using a region-based scheme derived from the number of pixels of objects. This type of evaluation is prevalent in the medical image segmentation due to its simplicity.

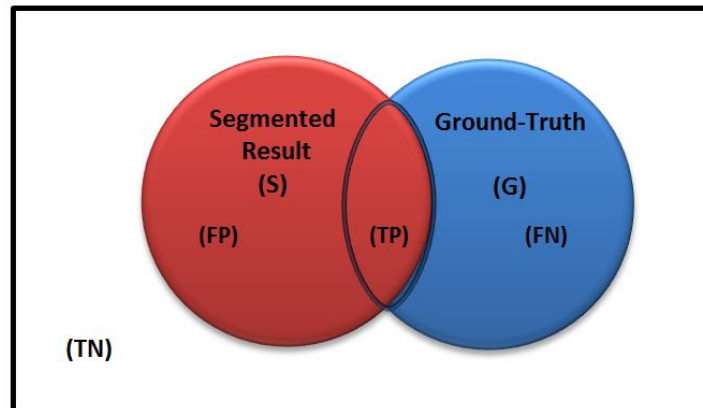


Figure 4.15: Demonstration of false positive (FP), true positive (TP), true negative (TN) and false negative (FN) regarding ground-truth (G) database and segmentation results(S).

As shown, in figure 4.15, G is a ground truth and S is a segmented area. The intersection of these two areas shows with black boundary. The terms (FN), (TP), (FP) and (TN) contribute in the performance of algorithms, which was evaluated in terms of sensitivity (SN), specificity (SP) and accuracy (ACC). These statistical measurements are used to determine the quality of binary segmentation and segmentation classification (Altman and Bland, 1994).

True Positive: Cilia in ground truth detected as cilia.

True Negative: Background in ground truth detected as background.

False Positive: Background in ground truth detected as cilia.

False Negative: Cilia in ground truth detected as background.

$$\textbf{Sensitivity} = \frac{TP}{(TP+FN)} \quad \textbf{Sensitivity} \in [0, 1]$$

$$\textbf{Specificity} = \frac{TN}{(TN+FP)} \quad \textbf{Specificity} \in [0, 1]$$

$$\textbf{Accuracy} = \frac{(TP+TN)}{(TP+FP+TN+FN)} \quad \textbf{Accuracy} \in [0, 1]$$

All these metrics are between zero and one and the higher the value within this interval indicates the better segmentation performance (Lalkhen and McCluskey, 2008).

Receiver operating characteristic (ROC) (Linden, 2006) curves are a commonly used way of overall visualization of the performance in a binary segmentation. The main value of ROC curves is that they provide a variety of possible trade-offs between the true positive fraction and false positive fraction, enabling the algorithm designer to choose an appropriate operating point. ROC curve is a plot with true positive fractions (SN) versus false positive fractions (1-SP) at different threshold levels. The closer the ROC curve approaches to the top left corner, the better the performance of the algorithm. The area under the curve measures how algorithms distinguish between cilia and background and give a general idea of SN, SP and accuracy. If the area under the ROC curve is 1 then the system has agreed totally with the ground truth segmentation. However, note that manual segmentations do not create perfect labelling.

The trapezoidal method is used to approximate an area under the ROC curve and offers a method of estimating integrals. This method is adopted by breaking the region into a number of trapeziums for easily computable areas.

Following cilia segmentation algorithm performance, the next stage was to evaluate cilia length measurements against the manual cilia length analysis. The box plot (McGill, Tukey and Larsen, 1978) and absolute value are two techniques used to verify the performance of the system. The use of box plot enables us to study the shape of the statistical distribution of the cilia lengths. Box plot visualization allows us to compare a variety of statistical measures and demonstrates overall patterns of response for each category methods.

The algorithms are evaluated to the actual magnitude of the cilia length values by calculating the absolute difference values which is a distance from zero. Box plots of the absolute difference value of methods are then plotted.

Cilia number in nodal images was counted and evaluated against the manual assessment.

4.9 Results

4.9.1 Segmentation Results

To systematically evaluate the performance of each algorithm, the ROC curves created for the visual performance of each proposed methods of whole cilia images which are presented in this section. This ROC curve created by varying the threshold level. Each point shows an operating point (cut off) threshold. The area under the curve (AUC) of ROC was calculated. Maximum accuracy and minimum distance to the top left corner of the ROC curve are two techniques used to find the best operating point.

The segmentation evaluation was performed on the high-resolution image dataset. The first three methods (Mathematical morphology, Gaussian and Gabor) were evaluated against all ground truth (manual pixel labelled) of six high resolution images. To evaluate the KNN method two images were used for training (one normal and one abnormal) and four images were used for evaluation/testing.

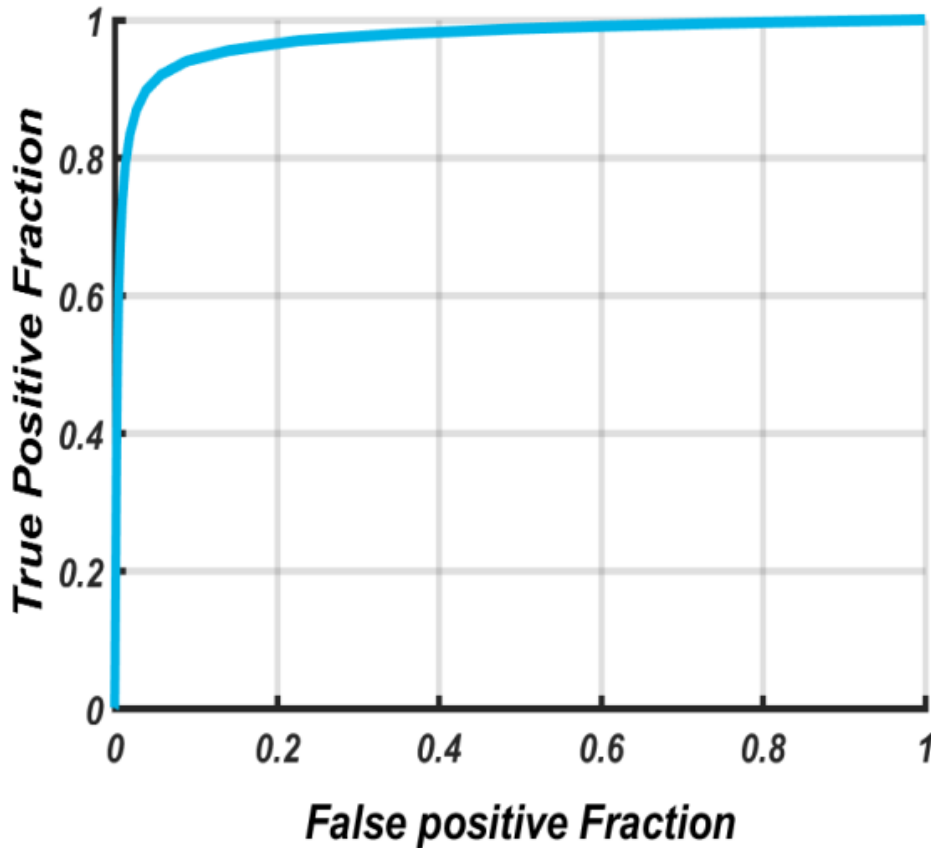


Figure 4.16: The ROC- curve for the cilia dataset. The performance result of the mathematical morphological operator.

As shown in figure 4.16, illustrates the ROC curve on the cilia dataset. The graph represents excellent ROC curve of morphological operator with linear structure applied on all cilia dataset. The AUC value for a dataset of normal and abnormal cilia was 0.9721. The operation point to the maximum accuracy of the performance was 0.9774 with a sensitivity value of 0.7358 and a specificity of 0.9901. These results showed the good performance analysis of the mathematical morphology with a linear structure. The operating point of the minimum distance to the top left (0, 1) corner of the ROC curve populates a value of 0.0987 with the sensitivity value of 0.9195 and specificity of 0.9429.

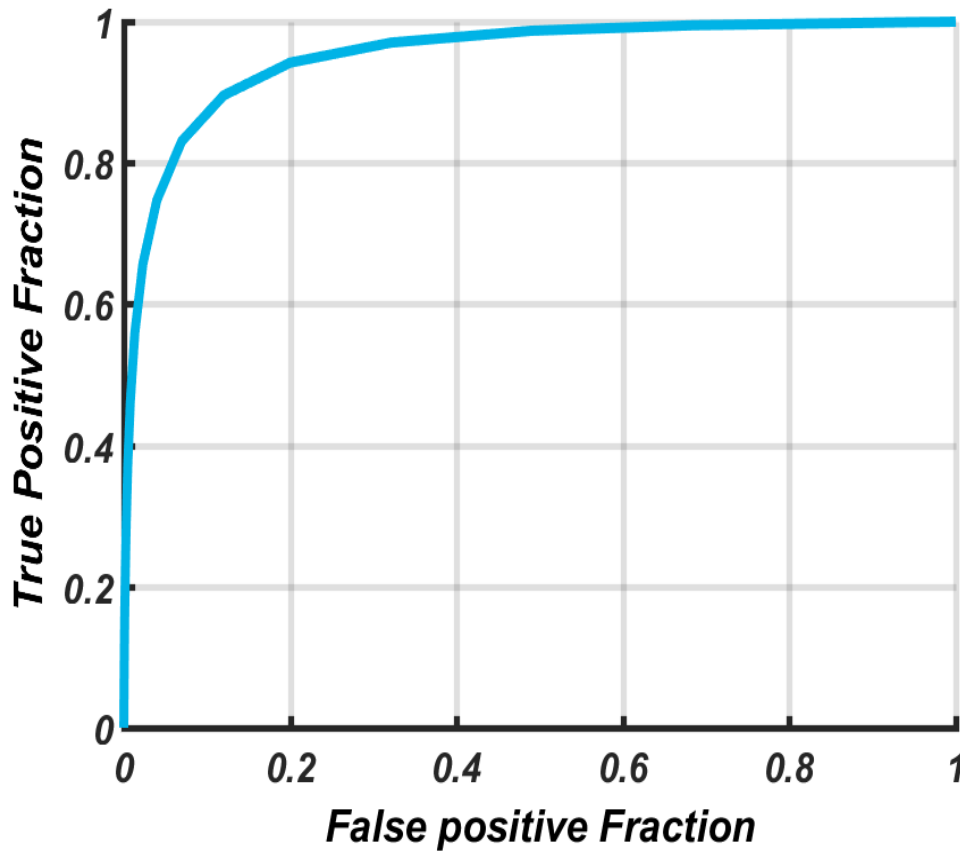


Figure 4.17: The ROC -curve for cilia dataset. The performance of the Gaussian filters.

The Gaussian-based approach was another method applied to cilia dataset for segmentation purpose as discussed earlier on. The result of the ROC curve in figure 4.17 presents a good performance of ROC curve with AUC value of 0.9520. The algorithm demonstrates with the operating point of maximum accuracy value of 0.9656 with the sensitivity 0.4626 and specificity 0.9923. According to the figure 4.17, the minimum distance curve to the top left (0, 1) corner of the graph was 0.1591 with a sensitivity of 0.8957 and specificity of 0.8799.

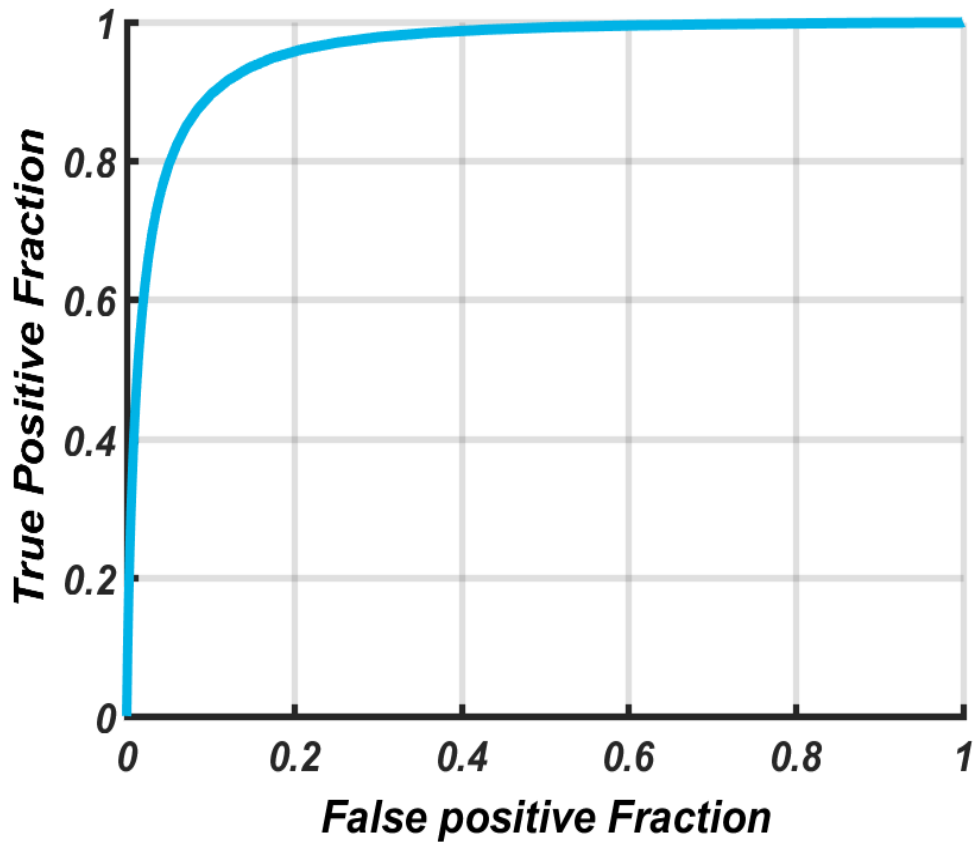


Figure 4.18: The ROC curve for the cilia dataset. Performance of Gabor filters.

Next, the Gabor filter was applied to segment the cilia images. The Figure 4.18 shows the performance of the ROC curve of the Gabor filter. The area under the curve had a value of 0.9578. The operating point with a maximum accuracy of Gabor filter was 0.9625 with a sensitivity of 0.4766 and specificity of 0.9881.

The operating point of the minimum distance of the graph in figure 4.18 to the top left corner (0, 1) had a value of 0.1449 with a sensitivity of 0.8964 and specificity of 0.8987.

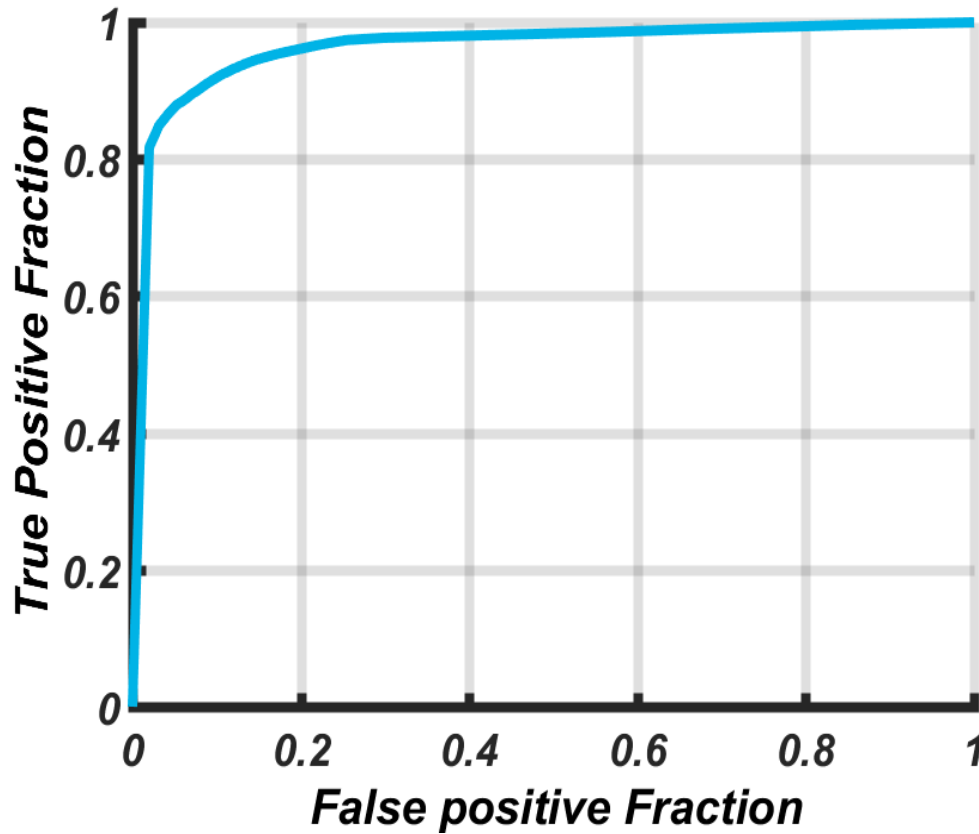


Figure 4.19: The ROC curve for the performance of the KNN classification of two training and four testing images.

K Nearest Neighbour classification was applied to cilia dataset. Figure 4.19 illustrates the ROC curve of KNN. The AUC value was 0.9625. The operation point of the maximum accuracy of this method was 0.9714 with a sensitivity of 0.8172 and specificity of 0.9801.

The minimum distance of the curve to top left corner was calculated. The operating point of the minimum distance to (0, 1) was 0.1257 with a sensitivity value of 0.9068 and specificity of 0.9157.

The results of proposed methods of operating point with maximum accuracy are also presented in Table 4.2. According to the results, Mathematical

morphology operation produces the best results at operating with maximum accuracy and higher area under the curve.

Method	Number of Images	SN	SP	AUC	operating point with max ACC
Morphology	6 Images	0.7358	0.9901	0.9721	0.9774
Gaussian	6 Images	0.4626	0.9921	0.9520	0.9656
Gabor	6 Images	0.4766	0.9881	0.9578	0.9625
KNN Classification	4 Images	0.8172	0.9801	0.9625	0.9714

Table 4.2: Illustrates the performance analysis of the best operating point base with maximum accuracy. SN(sensitivity), SP(specificity), AUC(area under the curve).

Table 4.3 restates the performance of the operating point at a minimum distance of the curve to the (0, 1). From the results, we can conclude that the performance of the mathematical morphology illustrates the high performance of AUC value of 0.9721 with a minimum distance of 0.0987.

Method	Number of Images	SN	SP	AUC	Distance point closest to (0,1)
Morphology	6 Images	0.9195	0.9429	0.9721	0.0987
Gaussian	6 Images	0.8957	0.8799	0.9520	0.1591
Gabor	6 Images	0.8964	0.8987	0.9578	0.1449
KNN Classification	4 Images	0.9068	0.9157	0.9625	0.1257

Table 4.3: illustrates the performance analysis of the best operating point with minimum distance to (0, 1). SN(sensitivity), SP(specificity), AUC(area under the curve).

To perceive the performance of the mathematical morphology method, examples of images of the best threshold with maximum accuracy and minimum distance were considered for further visual analysis.

As shown in figure 4.20, cilia images were segmented with the operating point of maximum accuracy. It illustrates that some cilia have been removed by applying this threshold value. Likewise, this value has eliminated some pixels of cilia which can be a problem in later stage when estimating the true length of the cilia. The orange arrow shows the length of the cilium that has been removed by this threshold. Red arrow depicts almost all cilium removed and only some small pixels left. Other two green arrow shows cilia were fragmented into two.

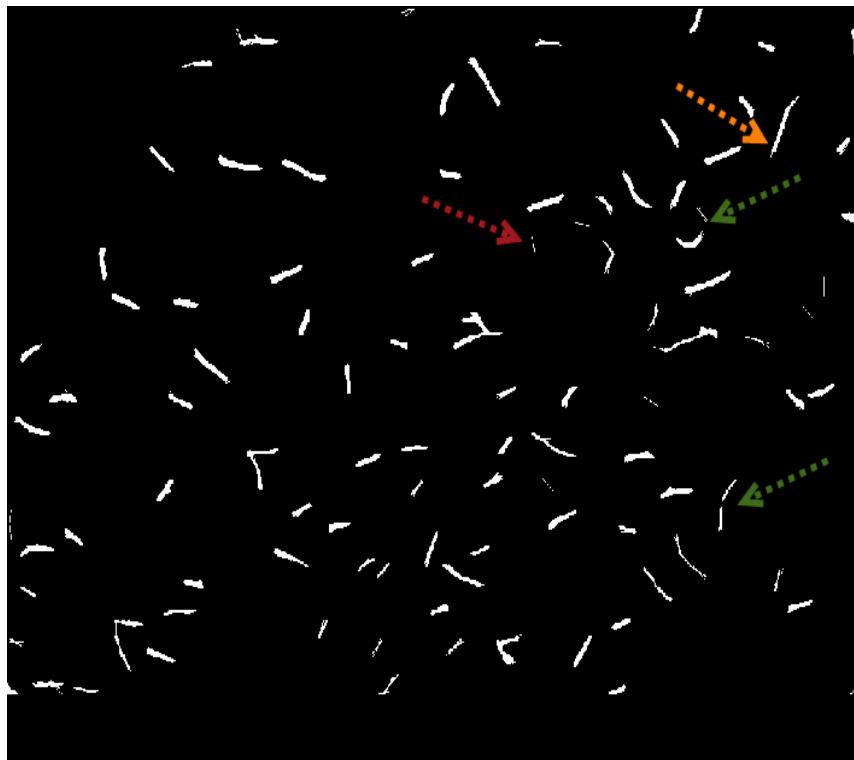


Figure 4.20: Illustrated the results of Mathematical Morphology operator with maximum accuracy.

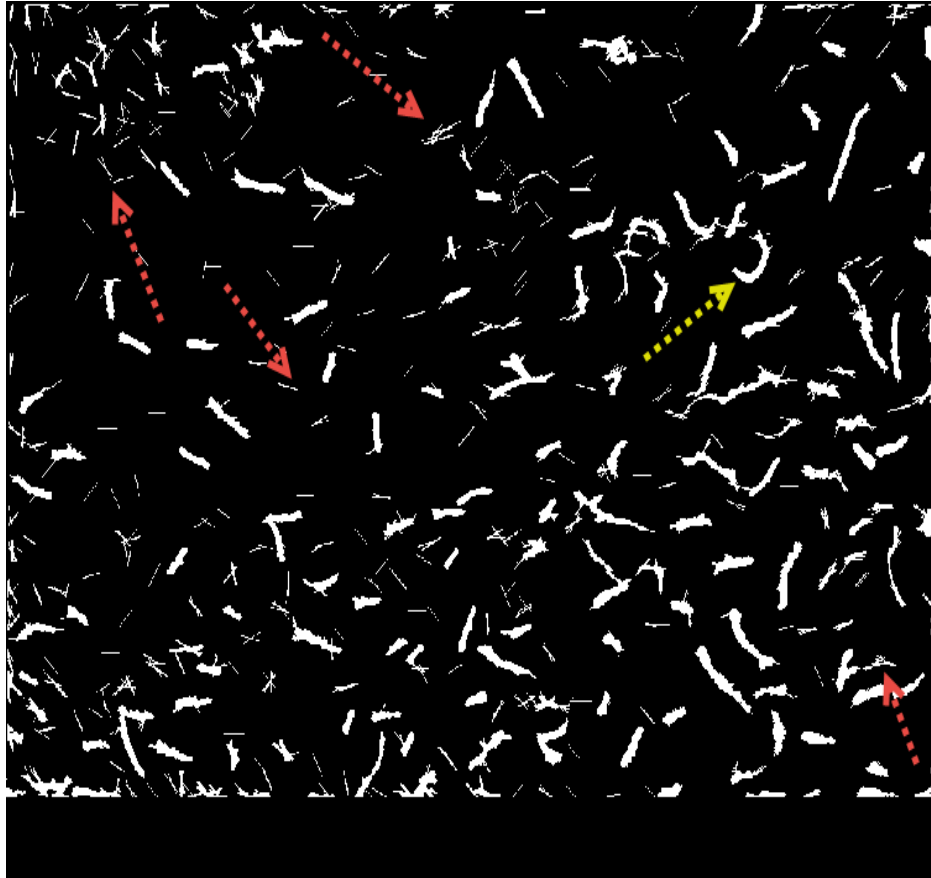


Figure 4.21: Results of Mathematical Morphology operator with the minimum distance to (0, 1).

Figure 4.21 depicts the results of Mathematical Morphology of the operating point at a minimum distance to (0, 1). The segmentation result depicts threshold values with the operating point at the minimum distance to (0, 1) picked up a lot of noise from the background.

Red arrows in this figure present the noise. The yellow arrow points to the cilia segmented with noise around it. Although operating point at the minimum distance picked noise from the background but compared to the operating point at maximum accuracy it is greatly improved. The threshold of the operating point at a minimum distance did not create the fragmented cilia but some connected noise to the length of the cilia produces fake results for further cilia quantification. Therefore; neither of these two techniques presented respectable segmentation results. Thus, the operating point value

was defined by visual assessment as it was required.

Cilia were enhanced with several enhancement methods. To find the best operating point two techniques were used; maximum accuracy and minimum distance to the top-left corner of the graph for the best threshold. According to the results of the ROC curve, Mathematical Morphology was the greatest enhancement method. Figure 4.20 and Figure 4.21 produces inconsistency in results with respect to the correct length of the cilia. Therefore, the threshold value was chosen visually. Post-processing applied to the threshold image to remove a noise and objects by touching points around the borders and setting boundaries. Figure 4.22 shows the visual results of the post-processing result. The image depicts the cilia images that were segmented by mathematical morphology and image that are exempt from any noise.



Figure 4.22: Post processing output.

4.9.2 Cilia Length

Good segmentation is important for good quantitative measurements. Once the pixel-based cilia evaluation was performed and established then the best method (mathematical morphology) is chosen to segment the cilia prior to length measurements. This section covers an evaluation of the different lengths measurements applied on to cilia segmentations for the high-resolution image dataset.

Box plots were plotted, to display the overall patterns of all methods. The box plot visualisation allows us to compare statistical measures for each category.

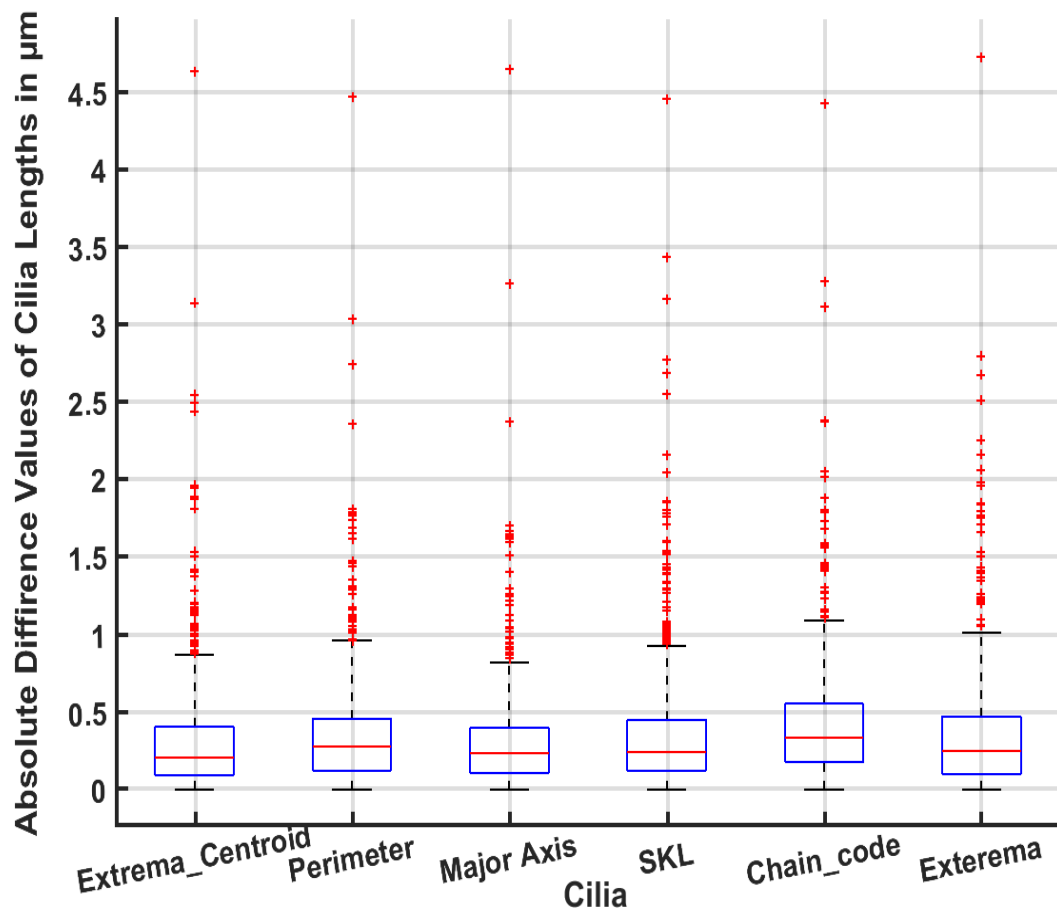


Figure 4.23: Box plot shows an Absolute difference of automated detection to their ground truth.

From graphs the absolute difference value of each individual method to the manual ground truth of all cilia. The median (red line in the box) shows there is not a significant difference between the performances of each method. Figure 4.23 demonstrates the median of Major Axis scored in the middle of the box and the median value is very close to zero. Also, the spread of the data in all other boxes are much larger and there is more variables in the other methods. The simple Major Axis had shown the best results. To justify the conclusion because 80% of cilia are straight, therefore; simple and basic method such as major axis gives a good result to measure the lengths of the cilia.

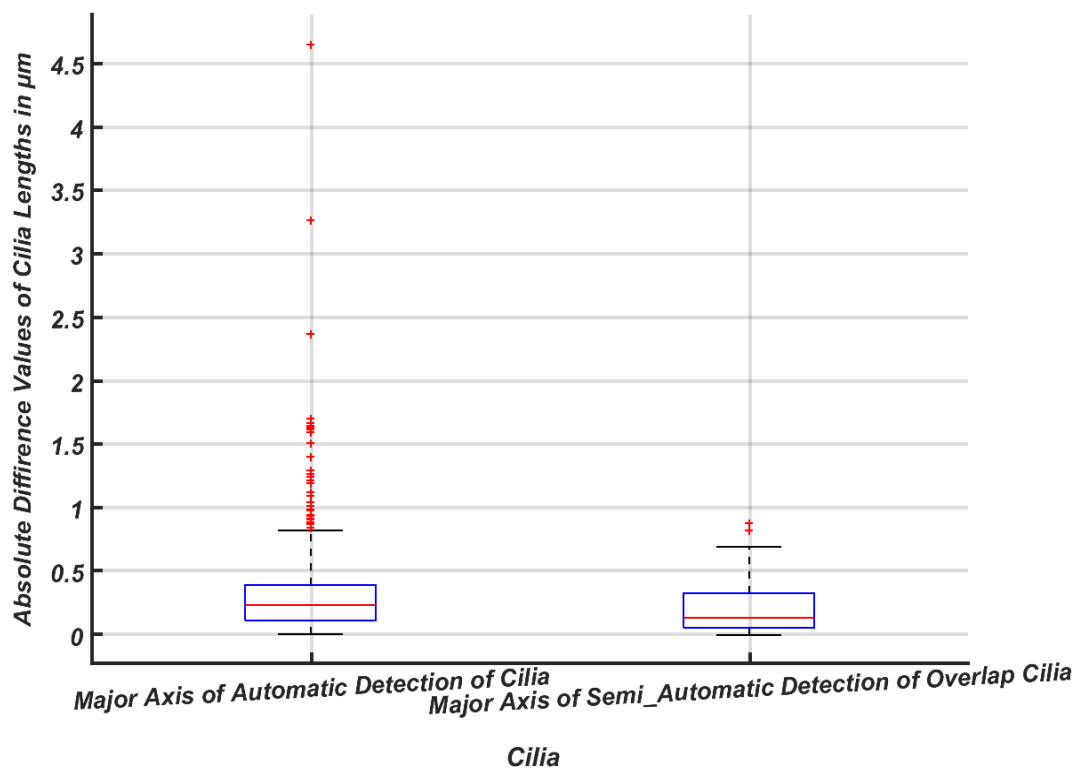


Figure 4.24: Box plot illustrates the Absolute Difference of Major Axis of Automatic detection and Semi-automatic detection of overlap cilia to manual analysis.

Automated Major Axis length measurements were giving promising results to the cilia lengths, thereafter in the semi-automatic method major axis was

used as explained in above section. Figure 4.24 illustrates the absolute difference of the Major axis in automated detection of all cilia and semi-automated detection of only overlap cilia. The major axis of the semi-automated detection of overlap cilia box plot in figure 4.24 shows the median is very close to the zero and close to manual measurements. The outliers in the semi-automated method are fewer than automatic method, range and the size of the boxes are almost the same. Therefore result shows that the semi-automated detection of cilia with the use of the long axis method is a good way of measuring the overlap cilia length and it is a trustable method.

4.9.3 Number of Cilia

This section demonstrates the calculation of the number of cilia from nodal images. Therefore, nodal cilia images were segmented by the Mathematical Morphology operation (parameters were adapted for the nodal images) in combination with the selective post-processing method. The performance evaluation of cilia number was performed against the manual ground truth in order to quantitatively analyse the performance of cilia detection and efficiency of the algorithm with respect to the background noise. The pixels of segmented cilia were compared to the corresponding ground truth pixels. If 30% of pixels of segmented cilium were matched with corresponding pixels in the ground truth, then it was established the algorithm detected that cilium correctly. The results of normal cilia images demonstrate the numbers of cilia that were detected equates to 72.02% (the average number of cilia in GT image is 200). This was at a cost of 54 false positive objects per normal image. Abnormal cilia were counted with 68.05% of the cilia objects detected with the cost of 107 false positive objects per image. The result is summarised in table 4.2.

Nodal Cilia	Normal Cilia	Abnormal cilia
Ground Truth	200	160
Proposed Algorithm	72.02%	68.05%
False Positive	54	107

Table 4.2: Number of cilia per node. Each pixel of cilium compared to the corresponding pixel in ground truth.

4.10 Summary

In this chapter, various methods were proposed to detect and segment cilia in the field of microscopic image analysis, in particular, the automatic segmentation, measurements followed by automatic/semi-automatic length measurements and the evaluation of the segmentation results were elaborated in detail.

Accurate segmentation of the cilia from SEM microscopic images is the main impediment and a challenge. It is a challenging task due to the noise and variation in the background intensity pixels. Accurate segmentation results produce the greatest quantitative measurements of cilia. Therefore due to the noisy images, the combination of an automated method followed by a semi-automated method was proposed for microscopic cilia images to increase the quality of the quantification measurement accuracy.

Preparation of cilia image was done prior to further enhance them and improve the results. Coloured cilia images are converted to a grayscale image. The median filter is then applied to estimate the background and subtracted from the grayscale image to correct the non-uniform illumination.

A number of image processing methods and how their combination affected the results of the segmentation on the cilia microscopy images were considered. The mathematical morphology operation with a standard linear structure in various directions proved to be the best method of detection for a

new application of cilia. In addition, the emphasis is put on confirming cilia are detected with the appropriate selection of parameters for cilia segmentation.

Grey-level profiles of the cross-section of the cilia in Figure 4.6 were approximated by a Gaussian-shaped curve. Then Gaussian filters which are different from the standard isotropic is applied. This was repeated a number of times and stacked to make the length of the filter which gave the filter an aspect of linearity. The value of the area under the ROC curve for the Gaussian filter was 0.9520.

Gabor filter was an algorithm used to enhance the multi-oriented thin objects such as cilia and filter out the noise background. This method was convolved with cilia images and according to the result in result section, the area under the ROC curve of the Gabor filter enhancement had a value of 0.9578.

Machine learning of the KNN classification was used to classify the cilia images as cilia and non-cilia with $K=31$. The KNN was applied to all data with the input of five features. The output of the three different proposed enhancement methods were used (as described in methodology section) as features. The other two features were the results of background subtraction and grayscale images. The performance of the KNN classification provided a ROC value of 0.9625.

Due to the lack of cilia data, a further investigation by other machine learning methods did not precede as most of those types of methods require a large dataset which was not the case in this study.

Mathematical morphology was applied to cilia images to enhance the cilia. From the results produced in result section, it is obvious that the method responded well to cilia spread in different directions on the image. The area under the ROC curve was 0.9721, with a maximum accuracy of 0.9774. Also supported by evidence, from figure 4.16 - 4.19, the area under the ROC

curve proved that the mathematical morphology operation is the best method for detection of cilia. It was shown that the algorithm enhances the cilia very well and has an ability with linear structure property to separate the thin structure of cilia from the noisy background image without manipulating the structure of the cilia. The algorithm may help to avoid false detection as well as enhancing cilia with promising results. The performance indices of sensitivity and specificity at the maximum accuracy are 0.7358 and 0.9901 respectively.

Accuracy is the normal approach to finding the best operating point. Accuracy and the minimum distance of the curve to top left corner were calculated to find the best operating point. Table 4.2 and Table 4.3 determined the results of the sensitivity and specificity of the methods. Mathematical morphology proved to produce the best results, with an operating with the highest maximum accuracy, an alternative operating point with the lowest minimum distance to (0,1) and also it achieved the highest area under the curve.

According to Table 4.2 – the specificity of the Mathematical morphology method indicates that the background pixels were detected correctly as background. And sensitivity shows cilia correctly detected as cilia but bear in mind the proportion of cilia to the background is very small. There are 95% of pixels are background pixel whereas cilia pixels are only 5% of the whole image.

Mathematical Morphology operator with the operating point corresponding to maximum accuracy. The results clarify some cilia are not detected and some are fragmented. Figure 4.21 illustrates the cilia detection results of Mathematical Morphology operator with the operating point corresponding to the minimum distance to (0, 1). It is noticeable that the segmentation results are very noisy, and noise has been detected as cilia.

Gabor and Gaussian are both filter based methods that are good at detecting the fragmented cilia but does not have a good response to the noise. In contrast to mathematical morphology, filters attempt to fit the cilia structure therefore in case of fragmented cilia it does not detect the whole structure of cilia, but the advantage is it responds well to the noise.

According to the sensitivity and specificity values and the outputs of the described operating points, led us to conclude that these outputs (cilia binary images) do not produce the desired outcome. Hence, the best operating point for cilia segmentation was chosen visually.

The best method (Mathematical Morphology operator) with best operating point used to segment the cilia, following this length measures were examined. Six different lengths measurements were applied on segmented cilia to measure their lengths. The evaluation of methods was completed and compared to manual length measurements. The absolute difference value of the methods to manual measurements were made and box plot were drawn to compare the methods visually. As shown in, figure 4.23, demonstrates the major axis plot is the smallest box which suggests that the overall automated measurements have a high level of agreement with the manual measurements. The Chain code approach suggests there are quite different measurements of the manual ground truth. Therefore; because 80% of cilia are straight then simple major axis had shown the best results to measure the lengths of the cilia.

Further to that justification, the length of major axis of the best-fit ellipse function was used to calculate the lengths of overlap cilia in pixels using a semi-automatic approach. According to the results, the semi-automatic method had the capability of measuring the lengths of overlapping cilia.

Quantitative evaluations of the results of the semi-automatic length measurements algorithm were similar to manual assessment. Therefore the

median of the absolute difference between semi-automatic and manual measurements showed the only small difference between the semi-automatic results and manual assessment. Quantitative results demonstrate the semi-automatic results were accurate, in cilia microscopy with the noisy background, even when acquisition artefacts were presented in such a manner with contrast and overlapping.

The number of cilia were counted in normal and abnormal images. A cilium was considered to be detected if 30% of the segmented pixels overlapped when compared to the corresponding pixels of cilium from the ground-truth. The algorithm detected 72.02% of the cilia objects with. This was at a cost of 54 false positive objects per normal image.

Abnormal cilia are very short and scattered in a very noisy background as sometimes they are very difficult to distinguish visually from the background noise due to their pixel intensity similarity. Therefore the algorithm counted 68.05% of the cilia objects, with the cost of 107 false positive objects per image.

4.11 Discussion and Conclusions

Cilia are small thin structures that hang from the surface of the cell. Alteration of the cilia morphology can indicate early signs of genetic disorders, and hence analysis of cilia population and lengths followed by accurate segmentation is important in early diagnosis.

Different methods have been developed to achieve this goal and in this chapter four category of segmentation, methodology have been applied based on thin structure detection with an aspect of linearity and classification methods. Although the Gaussian and Gabor with an aspect of linearity and K NN widely have been widely investigated and developed but in this case of cilia segmentation, they didn't override the problem of the noise. Because

SEM cilia images are too noisy therefore the Mathematical morphology with linear structure enhanced and segment the cilia precisely.

The length of the normal and abnormal cilia were investigated and normal cilia shown had longer lengths. The number of cilia were counted per node from normal and abnormal images. The normal images shown that they have more cilia per node compare to the abnormal cilia per node.

Chapter 5 Manual Analysis of Vessel-like structures in the Vicinity of Tumours

5.1 Introductions

Thin structures such as lines are important features in many medical imaging applications. Medical examples such as hair-like structures of cilia, thin structure of valve in heart and blood vessels in lung computed tomography (CT) scan images. Visualisation of these thin structures provides information in planning and help in diagnosing. Chapters 2, 3 and 4 have covered the segmentation of thin structures of cilia in SEM images. Morphology operation with an aspect of linearity proved to be a suitable method of thin structures of cilia segmentation. Therefore a tuned morphology operation was applied on blood vessel-like structures in the vicinity of lung tumours in lung CT images. The objectives of chapters 5 and 6 are segmenting and analysing vessel-like structures in lung CT images. This chapter begins with a discussion of the anatomy of the lung, how lung tumours develop and description of tumour characteristics and investigation of the relationship of tumours and associated vessel structures in the lung.

Blood vessel attributes such as vessel number, radius, tortuosity, and branching pattern are vulnerable to a variety of diseases from a common cold to more serious ones such as cancer. For instance, change to the vessel tortuosity could be an early sign of tumour malignancy (Bullitt *et al.*, 2005b). CT scan images are very sensitive and have become a key lung disease imaging source for lung disease diagnosis over the years. CT images are used mainly in the early detection of lung masses. Furthermore, follow-up studies of them are often used to observe the growth of a lung tumour and helps with treatment planning.

The computer-aided detection system increases the speed and accuracy diagnosis. CAD systems will assist in helping doctors to analyse the effect of the treatment prescribed and assist in therapy planning. CAD has been developing rapidly and widely and has extended to various medical imaging processes.

The objective of this chapter is to examine study vessel-like structures in areas of unilateral lung tumours compared with the equivalent contralateral lung with no tumour; the methodology involves both visual assessment and semi-automatic detection of vessel-like structure attributes in the vicinity of a tumour from lung CT scan images.

The number of clearly defined vessel-like structures directly attached to a tumour were counted and compared with the corresponding region in the contralateral lung with no evidence of a tumour (Neda *et al.*, 2016). Lengths of the vessels in the lung CT images were also measured and used in order to determine the tortuosity of the vessels; main long vessels and long branches were measured but small vessels extended from branches was disregarded. The area of the tumour of the vessels was manually delineated and calculated in terms of pixels.

5.2 Lung Cancer and Blood Supply

Abnormalities in vascular patterns, such as morphological changes in vessel shape, branching patterns, width, tortuosity, or appearance of the vessels, may be associated with the occurrence of abnormalities and disease (Lorthois, Lauwers and Cassot, 2014), (Bullitt *et al.*, 2005a). Thus, an automated quantitative analysis of changes in vessel morphology may help in early detection of such abnormalities.

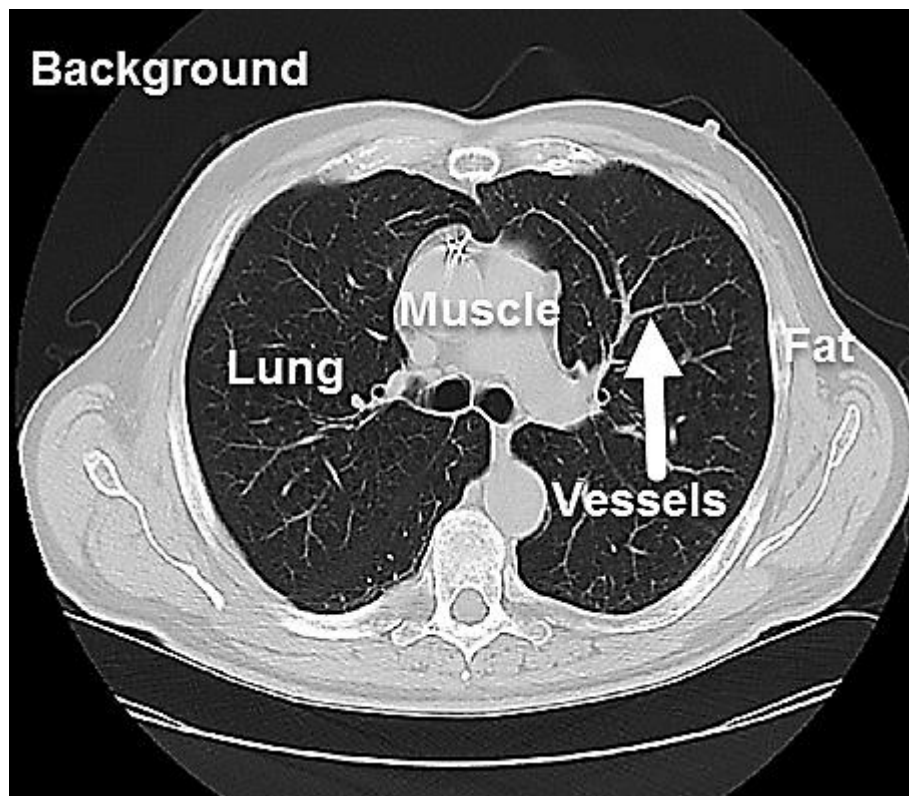


Figure 5.1: Axial lung CT image from the dataset (Lin *et al.*, 2015).

prepared by the author from image dataset to be described, shows an illustration of a lung CT image with standard lung windowing. The left and right lungs are separated by the mediastinum. The fat area contains the heart, trachea and blood vessels. Each lung consists of lobes the right lung has three lobes and the left lung has two lobes because of its smaller size. The diaphragm supports the lungs using wide long muscles that are placed under the chest cavity and separate the lung from the abdomen (Gillian *et.al*, 2004). Lung cancer is life-threatening and difficult to treat. According to the World Health Organization (WHO) lung cancer is extremely prevalent in the world with 1.59 million deaths annually (Ferlay *et al.*, 2015) Smoking has been shown to be a risk factor that damages lung tissue and increases the probability of it turning into lung cancer (American cancer society, 2018). Lung cancer is prevalent cancer in developing countries (Hirsch *et al.*, 2001). Lung cancer causes a wide range of conditions such as weight loss, chest and bone pains, fever and weakness (Birring and Peake, 2005)9,(Winston,

2018). Most lung diseases are diagnosed after a specialist doctor requests tests such as chest radiography or chest CT images. For example, cancer tumour nodules can be observed from CT scanning (Hirsch *et al.*, 2001).

A lung nodule (Patel *et.al*, 2017) is defined as a spot in the lung about three centimetres in diameter or less if it is seen on CT images of the lung, where it is larger than three centimetres it is considered a lung mass. If a mass of white tissue in the lung is smooth and round and nodules have well-defined borders, then this tissue is likely to be non-cancerous and benign. If pulmonary nodule borders are irregular and speculated, therefore, they are more likely to be cancerous (malignant) (Ha and Mazzone, 2014).

Pulmonary nodules are categorised as solid, partially solid ('sub-solid' or semi-solid), or non-solid (ground-glass opacities) (Bellomi, 2012). Cavity nodules contain an air-filled region that is termed "cavitary" (Bellomi, 2012). A solitary pulmonary nodule is defined as a discrete and well-defined margin with a rounded opacity. Their size is less than or equal to 3 cm in diameter where most of the solitary pulmonary nodules are benign (Bellomi, 2012), (Leung and Smithuis, 2007). However, they can be present in the early stage of lung cancer.

One primary indicator of cancer is spiky tissue extending from the border of the nodule (Ha and Mazzone, 2014). Figure 5.2 shows CT images of lungs with different types of the tumour from four different patients. These images are from the dataset lung1 (Grove *et al.*, 2015). Pulmonary nodules are indicated by red arrows. Image A shows the primary lung cancer nodule with a significant speculated margin. Image B indicates the cavity in the nodule with speculation shown around the edges (Primary lung cancer). Image C has a significant speculation margin. Image D is a solid benign nodule with a regular shape.

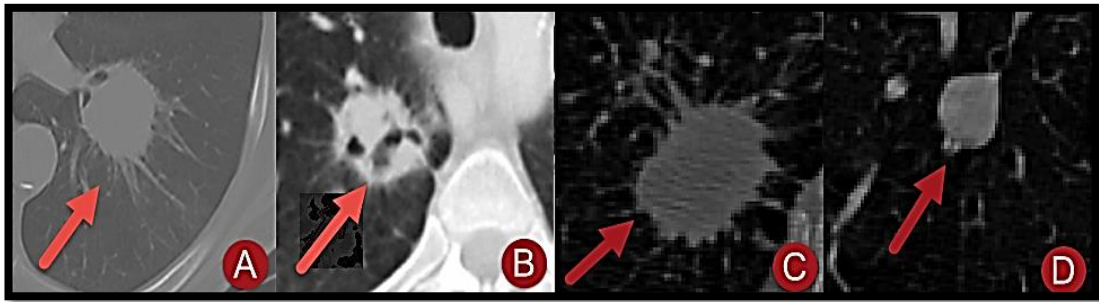


Figure 5.2: Illustrates various lung nodules on CT images from the dataset(A). The arrow indicates a nodule with significant speculation margin (Primary Lung Cancer). (B) The arrow indicates a nodule with cavities (Primary lung cancer). (C) The arrow shows a nodule with significant speculation margin (Malignance). (D) example with a solid nodule in the upper left lobe with regular, well-defined margins (Benign).

Zwirewich et al. evaluated pulmonary nodules of 85 malignant and 11 benign tumours and spicules were present in 90% of primary carcinomas as well as 5 of the 11 benign (Zwirewich *et al.*, 1991).

Adenocarcinoma is a subtype of non-small cell lung cancer. Adenocarcinoma is a formation of non-small cell lung cancer and is the most common type of lung cancer. The border of the adenocarcinoma has spicules or thin elongated pieces of tissue sticking out from its margins (Niehaus *et al.*, 2015).

Research has shown that a change in vessel attributes is caused by tumours (nodule mass) and nodules that erode the blood vessels, where this change is shown to be malignant (Bullitt *et al.*, 2005b). Although the majority of nodules are benign, early diagnosis of the presence of lung nodules is important and increases the chance of cure (Xu *et al.*, 2013).

Blood vessels play a significant role in cancerous tumours. A cancerous nodule requires a blood supply to deliver the nutrients and oxygen it needs to grow and survive (Cancer research Uk. 2014). It is thought that tumours on the blood supply they need by stimulating the foundation of new blood vessels (Cao and Langer, 2008). This process as first recorded in 1787 and called angiogenesis (Cao and Langer, 2008)(Cancer research Uk. 2014).

The process of angiogenesis is not the only way for a tumour to obtain blood, it can also extract blood from existing blood vessels co-opting them in their cancerous growth (Willis, 1934).

In 1971 Folkman (Cao and Langer, 2008) introduced the hypothesis that tumour growth is dependent on angiogenesis. The hypothesis was that once a tumour is created, every increase in tumour cell population must be preceded by an increase in new capillaries converging on the tumour (*Cancer research Uk*. 2014). Thus, angiogenesis was considered one of the hallmarks in the understanding of cancer. The lung is one of the organs in the body with the highest incidence of this type of neoplasm (Pezzella and Gatter, 2015), but so far, no data has been available on how cancer cells interact with normal lung vessels. Due to a tumour and blood vessels relationship it is important to provide accurate and comprehensive measurements of vessel features and morphology as it is important in the analysis of vascular formation and structural adaptations such as; physiological development or growth, pathophysiological conditions such as inflammation, hypertension, diabetes, obesity and cancer (Jonk *et al.*, 2007), (Levy *et al.*, 2008), (Murfee *et al.*, 2008), (Wiernsperger *et al.*, 2007).

According to Lin *et al.* there are two sources of blood supply to the lung. One source is the bronchial arteries, and the other is the pulmonary arteries. A bronchial artery usually provides the blood supply to bronchogenic carcinoma. The way the bronchial artery is connected to a malignant tumour is different from a benign tumour hence by studying these connections and changes that occur in these arteries in or near connections, can help defining the tumour nature. But this has limitations because chasing the entire path of the bronchial artery to the lung carcinoma is still a challenging task. Lin *et al.* studied the relationship between pulmonary arteries and lung tumour by CT and used this relationship to distinguish between a malignant and benign tumour. The relationship was covered as encasement, displacement, penetration, in the margin, and disconnection. The analysis of a tumour and

pulmonary arteries between benignancy and malignancy was significantly different ($p < 0.001$). Their results established that a malignant tumour has a tendency to encase and displace the pulmonary arteries, and a benign tumour has a tendency to be penetrated by the pulmonary arteries (Lin *et al.*, 2015).

Tuberculosis (TB) is the second most lethal disease worldwide (Datta *et al.*, 2015). Pulmonary granulomas are a brand of tuberculosis. Study of pulmonary tuberculosis (PTB) and lung cancer as comorbidities have shown that active PTB is noted in 2-5% of lung cancer cases, whereas lung cancer is noted in 1-2% of active PTB cases (Tamura, 2016). Large lesions develop their own vessels allowing them to continue to grow. Datta proposed that TB granuloma have similar characteristics to a solid tumour that they are associated with the abnormal vasculature. Their studies suggested that the morphology and structure of the granulomas associated with blood vessels are abnormal and showed a higher micro-vessel count around the TB lesion (Datta *et al.*, 2015). The physiological abnormalities of the abnormal associated vasculature can characterise the tumour vessels, these physiological abnormalities have been investigated (Jain, 2013).

Lung scar cancer was first classified by Friedrich in 1939. It is sometimes misdiagnosed as an old lesion, however, early detection and analysis are important for better treatment outcomes. They are mainly adenocarcinoma or peripheral lung cancer. Gao found lung scar cancers (LSC) and non-lung scar cancer showing an irregular or polygonal shape and long speculated border. They compared lung scar cancers (LSC) and non-lung scar cancer and the pre-surgical LSC images showed significant differences in speculation ($p < 0.05$) (Gao *et al.*, 2015).

The variety of different morphometric parameters of vessels such as speculation, diameter, tortuosity, and fractal dimension, border, shape, size were analysed (Bullitt *et al.*, 2005). Among vessel parameters, vessel tortuosity shows potentials for the diagnosis of many diseases (Jain, 2013).

Tortuosity is the property of the vessels being tortuous, twisted having many turns. Tortuous or twisted blood vessels (Lorthois, Lauwers and Cassot, 2014) and veins are seen in humans and animals. Mild tortuosity is a common irregularity with no symptoms but high vasculature tortuosity can be an early sign of abnormality such as tumour malignancy.

Blood vessels transport blood to other organs; however, these blood vessels may become tortuous due to abnormal development or vascular disease. Han studied that pulmonary hypertension (PH) can result in vascular pruning and increased tortuosity in the blood vessels (Han, 2012).

Bullitt et al. investigated regional changes of the vessels shape, as vessels become tortuous early during tumour development which affected initially healthy vessels and spread beyond the confines of tumour margins. Vessels tortuosity were investigated and statistical method of analysing the shapes of the vessels was performed on 34 healthy and 30 brain tumours seen on high-resolution magnetic resonance angiography (MRA) images (Bullitt *et al.*, 2005). Vessels histological evaluation and analysis were used to identifying a tumour as benign or malignant. According to Folkman's theory, unfortunately, even small cancers expressing growth can result in the alteration of the surrounding vasculature both physiologically and morphologically. Abnormal tortuosity is found in a variety of malignant tumours including those in the breast (Bullitt *et al.*, 2005), brain (Huang *et al.*, 2008), colon *et al.*, 1991), lung (Siemann *et al.*, 2002), and skin (Helmlinger *et al.*, 2002). These abnormal vessel shapes increase the geometric resistance to blood flow which in general is significantly higher in tumours than in normal tissue.

With the help of imaging technology, more tortuous vessels (Astner *et al.*, 2008) can be segmented and reported with various shapes, commonly curving, twisting, looping and kinking. Figure 5.3 demonstrates the different morphologies of the vessels that can be become tortuous.

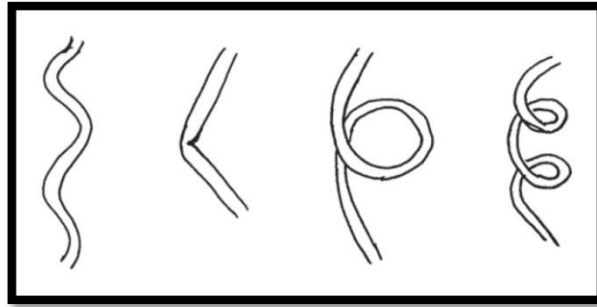


Figure 5.3: Schematics of various phenotypes of tortuous vessels. Left to right: curving, angulation/kinking, looping and spiral twisting (Han, 2012).

The ability to segment and quantify tortuosity abnormalities on high-resolution CT images presents and opens a new door for diagnosing tumour malignancies. As a further example of the usefulness of data imaging analysis the use of CT scanning images of tortuous vessels and tumours is pivotal in giving information to radiologists for further analysis which is discussed in the next section.

5.3 Material

The main important component of a medical imaging field is the set of images (datasets); therefore, the work involved in dataset collection should not be underestimated or undervalued. To illustrate the utility of the algorithm two sets of data were investigated.

The first set considered, consists of 61 lung CT-scans obtained from patients with primary lung adenocarcinoma who were treated in the Thoracic Oncology Program (Krupinski, 2004) at the H. Lee Moffitt Cancer Centre and Research Institute and the Maastricht Radiation Oncology Clinic (MAASTRO). The scans were intentionally acquired to follow up the sufficient patient cases and were acquired at the Moffitt Cancer Centre (Tampa Florida) on 16-detector CT scanner (Mx8000IDT, Philips, Best, and the Netherlands). The slice thickness is varying between 3 mm and 6 mm. The

images were completed at diagnosis and were taken prior to surgery. These images were reconstructed to 512 X 512 matrices. They are images from diagnostic contrast-enhanced CT scans. These CT scan images are 3-dimensional; each set of data contains 2-dimensional slides varying from 60 to 150 slides. From the first dataset, 10 out of 61 different patients with unilateral lung tumours were examined. From this dataset (lung one) 10 malignant manually were analysed.

An additional dataset of lung CT images (Grove *et al.*, 2015), (Armato *et al.*, 2015) called LUNGx Challenge were made available for diagnostic classification of malignant and benign lung nodules. The focus of this dataset LUNGx Challenge was the computerised classification of lung nodules as benign or malignant in diagnostic computed tomography (CT) scans. The dataset contains 10 calibration cases and 60 LUNGx Challenge cases. Most of these cases are contrast-enhanced scans. Of 10 calibration cases, five CT images were with malignant nodules and five cases with benign nodules which have been selected and confirmed by a specialist to contain a single nodule per CT scan for analysis purposes. The other 60 CT scans comprise the LUNGx Challenge test set. The location and the coordinates of the approximate centroid of each nodule (either 1 or 2) have specified with the label (malignant or benign). The nodules contained in the test set have been determined by a radiologist to be either primary lung cancer or benign based on pathologic assessment and/or follow-up imaging examinations. Images have 512 X 512 pixels per slice with the number of slices varying up to 413 slices. Their slice thickness is 1mm. These datasets are publicly available.

The MATLAB software used to analyse the cases. In each case, the image analyses were where the tumour size was greatest.

5.4 Lung Imaging Modalities

Most medical imaging techniques such as CT and MRI provide a non-invasive method for investigating the anatomy of living objects (Han,

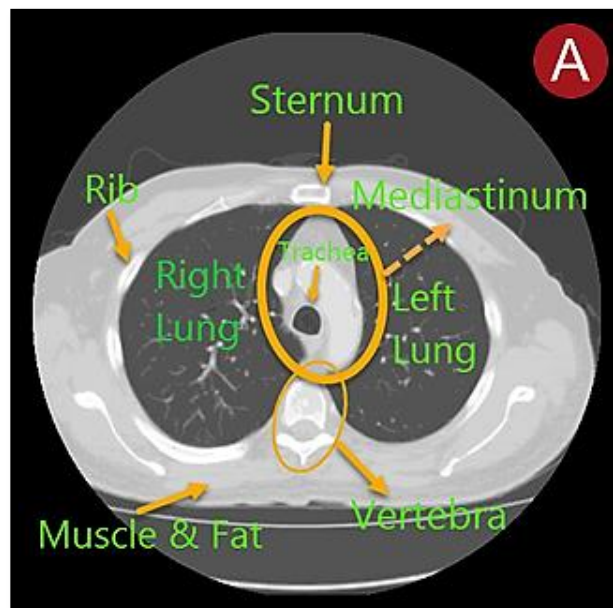
2012),(Davis, 2017). CT and MRI images allow the study of structural and functional information of the lung. The acquisition time for MRI images is around 15 to 30 minutes, which is long and considered as a disadvantage but patients are not exposed to radiation which is an advantage (Lusic and Grinstaff, 2012).

CT scanner devices use X-rays to produce visual representations of the interior of a body for clinical purposes. X-ray based CT device has been used since 1970 (Wielputz *et al.*, 2014). The chest radiograph is the oldest radiological method and is more frequently used for diagnosing disease in the lung. CT is a prevalent and significant tool with high speed and high resolution allowing the image dataset to be viewed in any plane desired (Röntgen,).The disadvantages of CT are the radiation and possible allergy to contrast agent (*CT Scan*. 2017). It combines multiple X-ray projections taken from different angles to create detailed cross-sectional images of internal tissues. These cross sections are used to evaluate the various structures of the internal tissue of lung, vessels structures and pulmonary nodules. It is also broadly used to investigate the circulatory system of the body such as blood vessels (Wielputz *et al.*, 2014).

CT scanners look like a big doughnut because the x-ray machine needs to spin around the body to make slides (*Computed Tomography (CT)*.). They consist of a radiation source and detector. The radiation source rotates around the body and the detector detects and measures the attenuation of the radiation passed through the body at different angles. Then the computer uses these measurements to generate cross-sectional images of the subject's body to provide a 3- dimensional image (3D) (*Computed Tomography* 2018). The output of such scanning devices used in radiology is digital. CT scan and MRI device generate DICOM images (McCollough and Morin, 1994) The most common images generated by CT scans have a matrix size of 512 x 512 pixels but can be generated in 1024 x 1024 and 256 x 256 sizes as well (Varma, 2012). Digital Imaging and Communications in

Medicine (DICOM) is the standard to transmit, store and display medical imaging information. Hence requires a dedicated viewer unlike other common image formats such as JPEG, JPEG 2000, TIFF, GIF (Allisy-Roberts and Williams, 2007). DICOM files contain a header storing information about the patient, acquisition process and image features (Varma, 2012). CT images are represented by pixels with CT values of the tissue which are called Hounsfield units (HU) (Varma, 2012). A Hounsfield unit is the ability to attenuate the X-ray signal by organ's tissue and is a quantitative scale for describing radiodensity in a standardised and convenient form (Allisy-Roberts and Williams, 2007),(Lusic and Grinstaff, 2012). Radiodensity of distilled water is defined as zero Hounsfield units (HU), while the air is -1000 HU. The HU of lung tissue is close to -1000 due to the high density of air in the lung and the HU for bone is +1000. The Hounsfield unit for most soft tissues is between 30 to 100 (Allisy-Roberts and Williams, 2007). Some CT scan imaging involves using a special dye called a contrast material (or contrast agent) to identify certain tissue. This contrast material blocks X-rays and appears white or black depending on processing. These contrast agents help to highlight and enhance the visibility of internal structures of the area of interest (part of the body being examined). The contrast agent is used to increase the signal attenuation in tissues with low HU to enhance them in the output image for better visualisation (Lusic and Grinstaff, 2012).

A lung scan is one of the specialised radiology methods used to identify lung conditions such as small tissue masses. Mostly there are three types of cross sections available to observe the subject under investigation for one CT scan. These are axial, sagittal and coronal sections depending on the condition of the subject and the doctor's interest (Lusic and Grinstaff, 2012). Figure 5.4 shows different cross-section slices of the lung CT scan images. In this figure 5.4 also yellow arrows demonstrate the left, right lung and other tissue appear in the CT scan images.



Axial Cross Section



Sagittal Cross Section

Coronal Cross Section

Figure 5.4: Three different views of cross sections of lung CT image. (A) Axial cross section of a lung, prepared by the author from image dataset to be described (Davis, 2016). (B) Sagittal cross-section (Lin *et al.*, 2015). (C) coronal cross section (Whiting, 2015).

Some nodules appear as a cavity, described as “cavitary”, meaning that the interior part of the nodule appears darker on CT images; they are more likely to be benign (Olson, 2017).

5.5 Methodology of Visual Analysis of Lung CT Images

This project takes advantage of human perceptual abilities in visually analysing lung CT images. Manual measurements can create highly accurate measured values of lung vessels characteristics. Using manual measurements between the tumour side and non-tumour side will be investigated. A limitation of the above investigation is that due available time. Manual measurements are first used to validate the automated method, followed by the automated method being applied to a larger dataset with the objective of supporting the results from the manual investigation (The automated system will describe in next chapter). Figure 5.5 depicts an overview of the manual investigation pipeline.

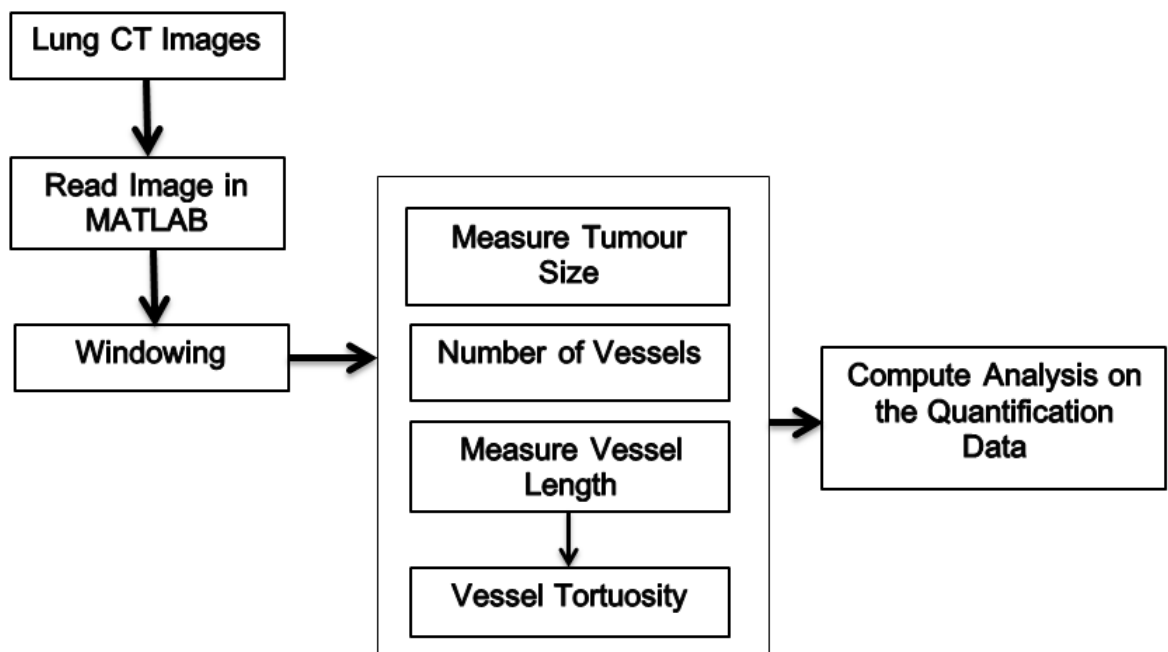


Figure 5.5: Flowchart depicting the pipeline of processing for CT scans images.

To perform visual analysis, a frame-to-frame analysis needed to be carried out. The study population consisted of 10 patients who had a tumour on either side the left or right lung but not bilateral. The objective was to investigate if there was a difference in lung vessel-like structures between the tumour side and non-tumour side.

The patients were randomly selected from a large dataset. A manual image analysis procedure was performed in MATLAB version 2015b (The MathWorks Inc., USA). Each frame was imported into the MATLAB software; the first stage of visual analysis was windowing each 2-dimension CT image from each 3-dimension dataset. The aim of windowing was to change the contrast of the 2- dimension image in order to enhance the vessels attached to a tumour and surrounding vessels on either side of the lung. This was achieved by using the image processing tool viewer called 'imtool'.

A comparison is then made between identical positions on the lung containing a tumour against the other lung without a tumour. The reason for the comparison is to examine any difference between the number of vessels in the immediate neighbourhood of a tumour on one side with the corresponding area on the other side. Subsequently, the total number and length of vessels on either side were counted and measured. Figure 5.6 illustrates the step by step of manual investigation in lung CT images. Image A is an original CT scan image of the lung read in MATLAB. Image B defines manual measurements of the tumour size with MATLAB functions. Image C is the result of manual windowing of the image A. Image D elaborates the measurement of the lengths of vessel-like structures speckles around a tumour.

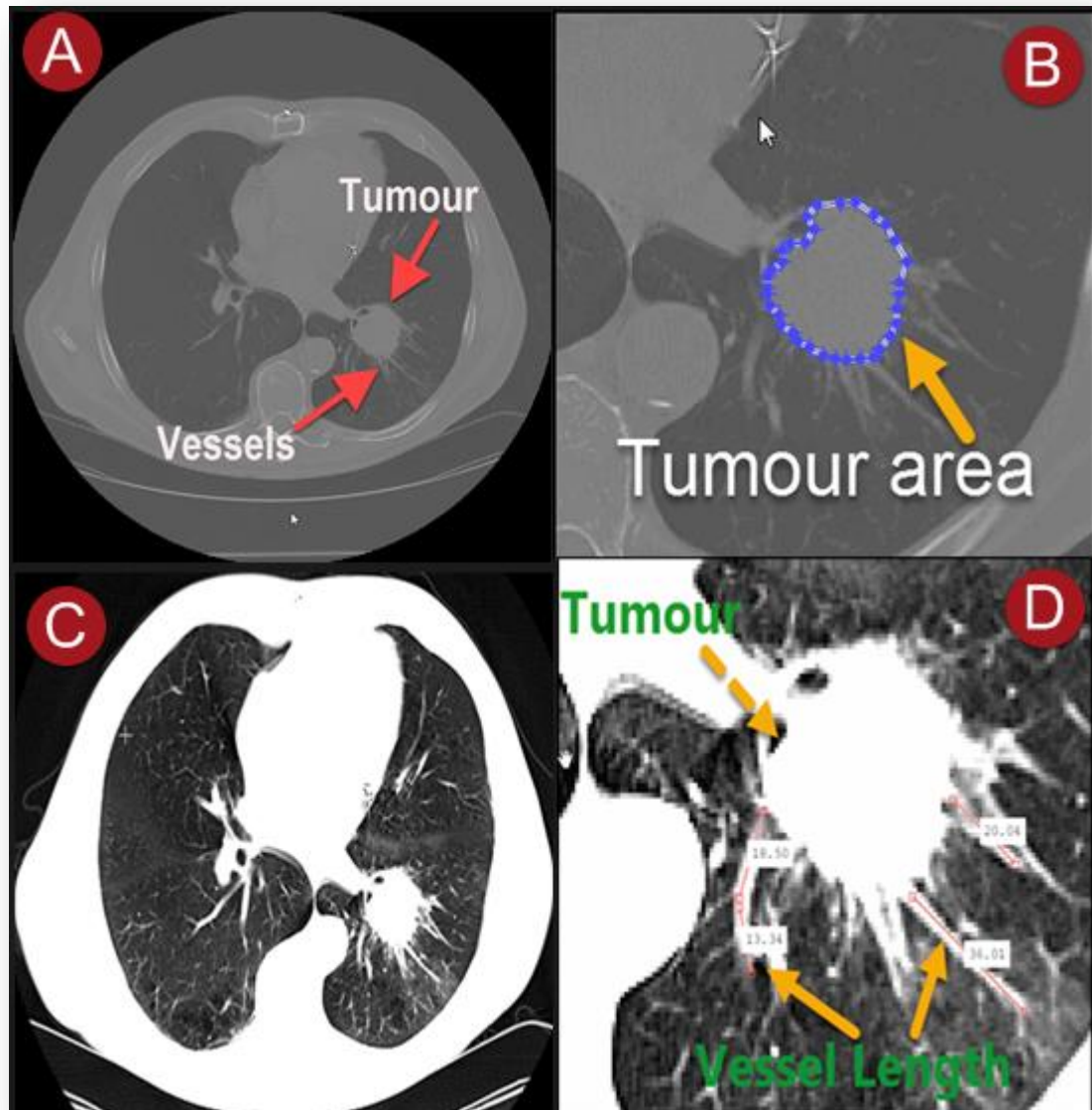


Figure 5.6: CT image from the dataset. A tumour is in the lower lobe of the left lung. (A) shows 2D contrast CT images of peripheral vessels in lung region. (B) Zoomed in image of (A) to specify a manual measurement of a tumour. (C) Shows the windowing results. (D) Zoomed in image of (C) to specify a tumour with surrounding vessels. Illustrates an example of manual vessel length measurement.

CT scan images of tumours for individual patients were segmented manually to identify the size of a tumour from all slides where a tumour was shown. This was calculated by use of a MATLAB function that creates an interactive polygonal tool, 'roipoly' to specify the area of a tumour. The distance tool button in the 'Image Viewer toolbar' assists us to manually measure the length of the vessels surrounding the tumour. This tool allowed the measurement of the length with a click-and-drag approach. Length measurements were pixel-based; the results can be converted to cm if required. Ten patients with lung tumours were examined, and the measurements of the length of the vessels on each a tumour were obtained.

In order to manually quantify the tortuous nature of vessels, the arc-cord ratio was used (Nat et al., 2014). This was performed by use of a MATLAB distance tool in measuring the length of objects, i.e. finding the distance between two endpoints of the same vessels. Therefore, the tortuosity of a vessel like structure was obtained by the ratio of the length along the curves of the vessel (L) to the Euclidean distance between two ends point of the vessel (C). It was calculated according to the equation 5.1.

$$T = \frac{L}{C}$$

Equation 5.1

5.6 Experimental Results of Visual Investigation

This section investigates the number and length of vessel-like structures to calculate the vessel tortuosity in the vicinity of a lung tumour and compare with the contralateral lung with no tumour. This was performed from slide had a maximum area plane.

5.6.1 Lung CT-Diagnosis Lung 1

Vessel characteristics were determined by visual assessment for 10 patients from the dataset from lung CT- Diagnosis (Hart *et al.*, 1997). The sets used were chosen as having unilateral lung tumours and good visual CT image quality. CT scan images of tumours for individual patients were calculated manually. The area of a tumour was measured by using 'roipoly' to specify the area of a tumour in MATLAB. The distance tool button in the 'Image Viewer toolbar' used to manually measure the length of the vessels surrounding the tumour. The area of a tumour was measured, choosing slice with the maximum area. The absolute difference value of vessels number of tumour side and the non-tumour side was calculated for each patient.

Patient Number	1	2	3	4	5	6	7	8	9	10
Number of Vessels in Vicinity of Tumour	8	8	6	6	5	8	5	10	8	6
Number of Vessels in Equivalent Area of Lung with No Tumour	2	2	1	2	1	3	3	3	8	6
Tumour size in Pixels	1205	590	1160	365	1397	1389	2063	1957	1162	322
Absolute Differences of Vessels Number	6	6	5	4	4	5	2	7	5	4

Table 5.1: Vessels number were observed in tumour side and non-tumour side with a size of a tumour in pixels. The absolute difference of a number of vessels in tumour side and number of vessels in the equivalent area with no tumour.

Table 5.1 summarises the results of the manual analysis. It lists the number of vessels near a tumour and the number of vessels in the corresponding area of the non-tumour side for the 10 patients with lung cancer. The results illustrate that the difference between the number of vessels in the vicinity of a tumour minus the equivalent area in the contralateral lung with no tumour had a median of 5 with a range of between 2 and 7; thus, in all cases there were more vessel-like structures in the vicinity of a tumour compared with the contralateral lung with no tumour. When checking the incidence of left and right sided tumours, 3 out of 10 cases had tumours in the left lung.

In all ten cases, the number of clear vessel-like structures in the immediate vicinity of the tumour was greater than that in the corresponding area in the contralateral side and the mean (standard deviation) of the difference was 5 (1.39). A Student t-test was performed to determine the statistical significance of the observed differences between the side of the tumour against the other side. There was a significant of the difference $p < 0.001$ (t-test).

In addition, vessel-like structures often appeared brighter on the side of a tumour. The results of this pilot study suggest that the number of clear bright vessel-like structures in the immediate vicinity of a lung tumour may be higher than in the corresponding area on the contralateral side.

In the following section, on bar chart graphs, blue bars show number of vessels or vessels tortuosity in the vicinity of a tumour and red bars are number of vessels or vessels tortuosity in the contralateral side with no tumour.

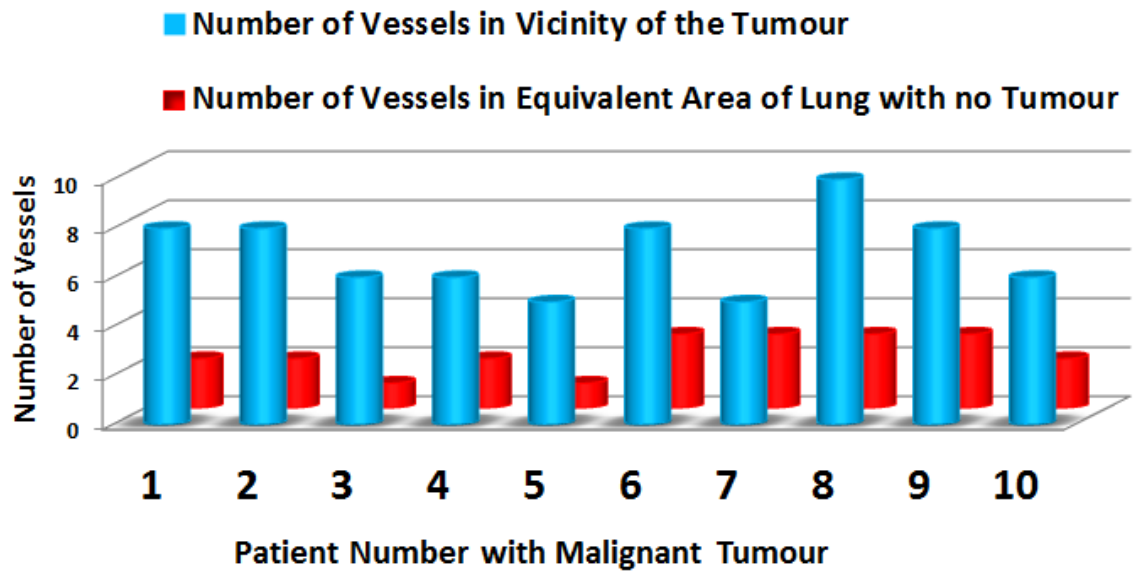


Figure 5.7: This bar chart illustrates the number of vessels in the vicinity of a lung tumour compared with the number of vessels in the contralateral lung with no tumour.

The bar chart in figure 5.7 illustrates the difference in vessel numbers in the lung with a tumour side and compared with the lung with no tumour. The x-axis represents the patient number with the primary lung cancer and the y-axis represents the number of vessels.

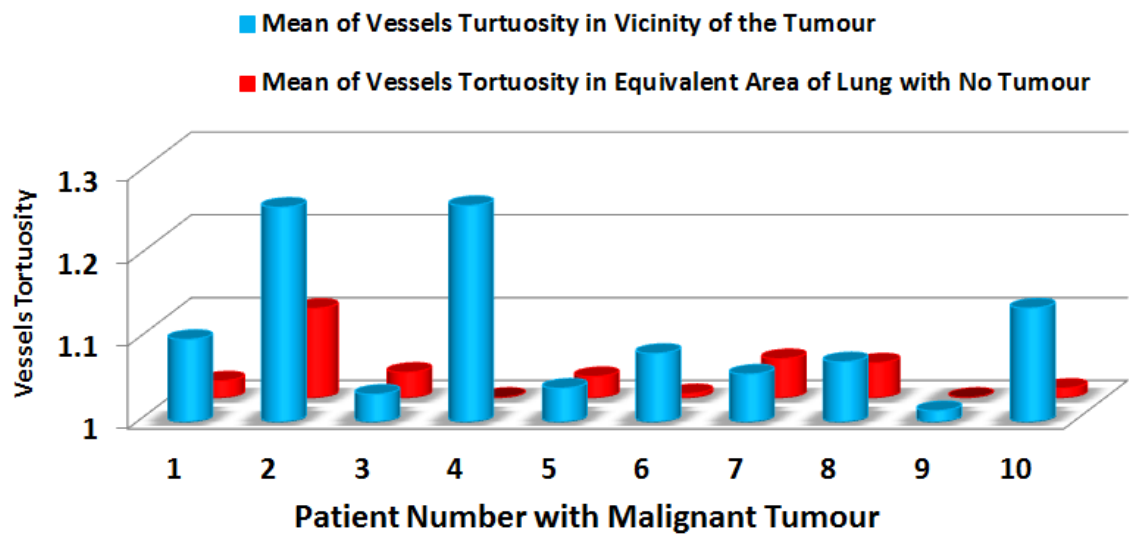


Figure 5.8: This graph shows the mean of vessels tortuosity in the vicinity of tumour compared with the mean of vessels tortuosity in contralateral lung with no tumour.

Measurement of vessel length enables calculation of vessel tortuosity in lungs; this was applied to unilateral lung tumours enabling comparison with the equivalent area in the contralateral lung without tumour. The bar chart in figure 5.8 shows the mean of the tortuosity on the tumour side compared with lung with no tumour. The x-axis describes the number of cases with primary lung cancer whereas the y-axis describes the mean of the vessel tortuosity in a range of 1 to 1.26.

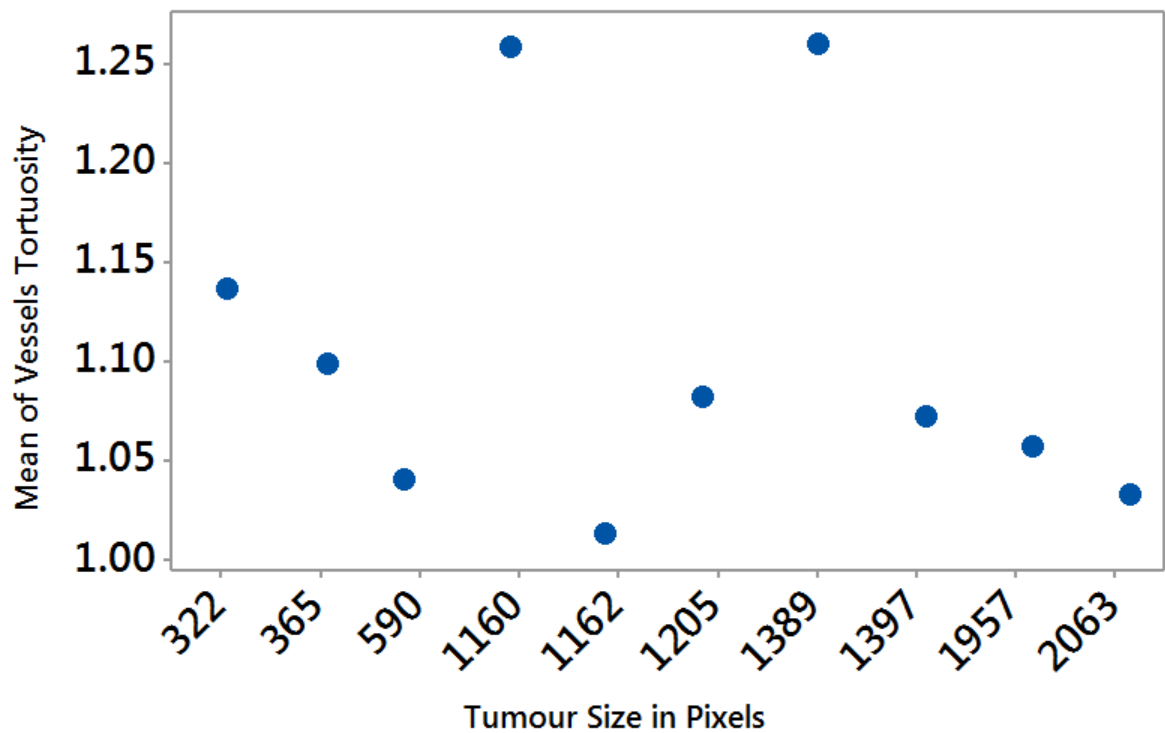


Figure 5.9: The individual value of tumour size and vessel tortuosity applied on lung CT- Diagnoses images.

Figure 5.9 shows the individual value plot, relating the patient tumour size with the mean of vessel tortuosity around it. The y-axis presents the mean of vessel tortuosity in a range of 1 to 1.25. The x-axis presents the area of a tumour in pixels. This plot indicates no clear relation between tumour size and the vessels' tortuosity.

5.6.2 SPIE-AAPM-NCILung Nodule Classification Challenge- LUNGx Lung 2

In this section, the method of manual investigation is applied to dataset 2 images LUNGx Challenge images (Grove *et al.*, 2015). The number of vessels in the vicinity of a tumour was counted in the unilateral side and compared with the corresponding contralateral area with no tumour. Twenty-three testing cases in the dataset were analysed. From the LUNGx challenge images, 12 cases and with malignant primary lung nodule and 11 cases of benign lung nodules were evaluated.

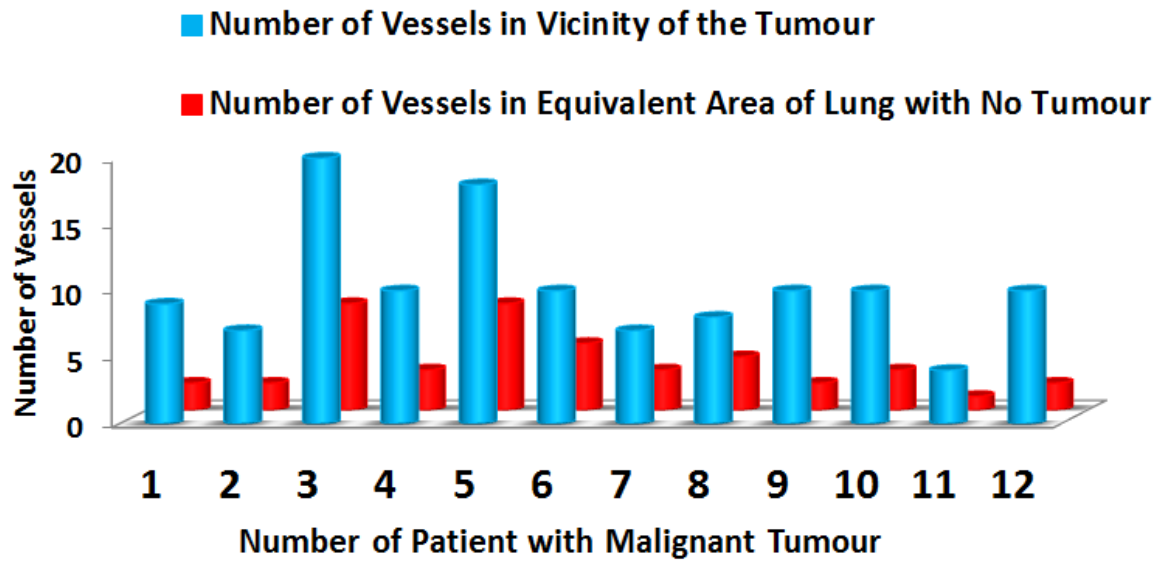


Figure 5.10: This bar chart demonstrates the number of vessels in the vicinity of lung tumour compared with the number of vessels in corresponding area of the lung with no tumour. The results are from LUNGx challenge patient with malignant tumour.

The bar chart in figure 5.10 illustrates the number of vessels in the vicinity of a lung tumour compared with the number of vessels in corresponding area of the lung with no tumour. It can be seen that the number of vessels of all 12 cases in the vicinity of a tumour is significantly higher than the corresponding area of the lung with no tumour.

There was a significant difference between the number of vessels like structure in the vicinity of a tumour compared with the contralateral lung with no tumour ($p < 0.001$ t-tests) with a mean (sd) difference of 10(4.5).

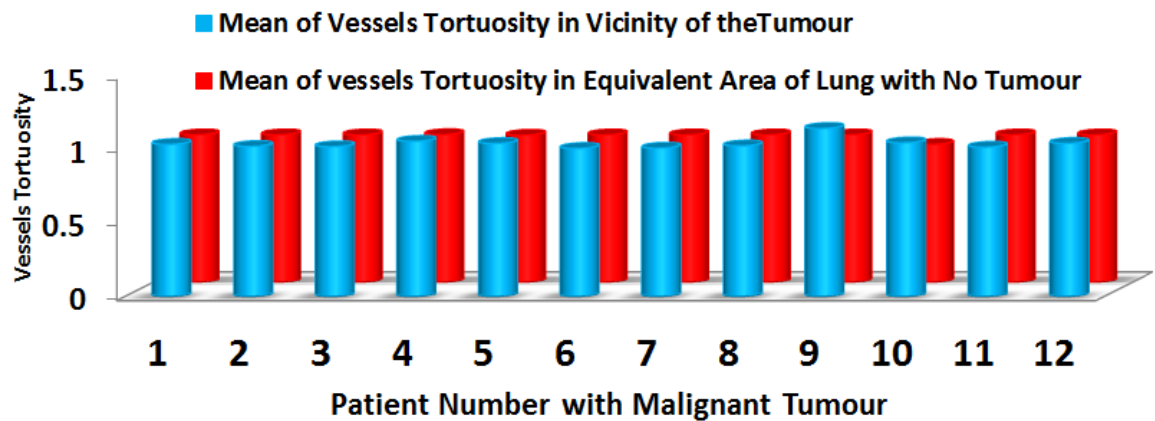


Figure 5.11: The graph bar chart represents the mean of the tortuosity in the vicinity of malignant lung tumours.

The graph in figure 5.11 represents information of the mean of the tortuosity of the vessels like-structures in the vicinity of lung tumour of patients with malignant tumour. It can be observed that the mean of the vessels tortuosity in the vicinity of a lung tumour is almost equivalent to the mean of the tortuosity of the vessel-like structures in the contralateral lung with no tumour.

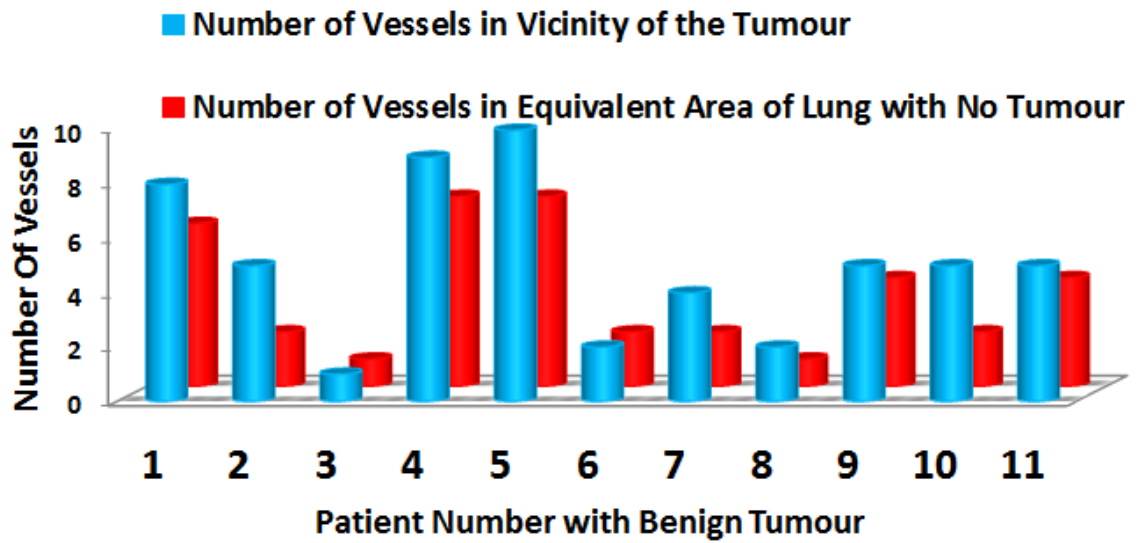


Figure 5.12: The bar chart shows the number of vessels in the vicinity of lung tumour compared with the number of vessels in contralateral lung with no tumour. The results are from LUNGx challenge images with benign tumour.

In figure 5.12 the bar chart describes the number of vessels in the vicinity of lung tumours compared with the number of vessels in corresponding area of the lung with no tumour. The results of 11 CT scan images of benign tumours indicated; it is slightly different between the numbers of vessels in the vicinity of lung tumour in comparison with the corresponding area of the contralateral lung with no tumours. The t-test confirmed there was no significant difference in the number of vessels in the vicinity of benign tumour and corresponding area of the contralateral side with no nodule.

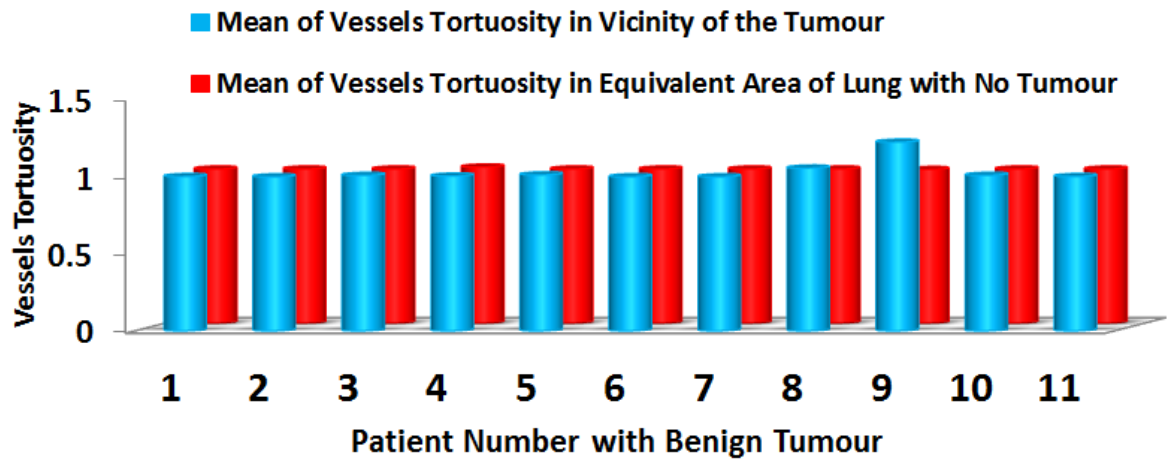


Figure 5.13: The graph presents the mean of the vessels tortuosity in the vicinity of benign lung tumour compared with the mean of vessels tortuosity in contralateral lung with no tumour.

The mean tortuosity of the vessels like structures in the vicinity of the benign nodule was calculated and compared with the vessel-like structures of the contralateral lung with no nodule. It can be noticed from figure 5.13 that in all but one case, the mean of the vessels tortuosity on the side of tumour is very close to the mean of the tortuosity of the vessels like structure on the opposite side with no tumour. The mean of the vessel tortuosity in nodule side of the only different case was 1.029 whereas the non- nodule side was 1. By observing the graph, it can be concluded that in benign cases, the mean of the vessels tortuosity in the vicinity of a tumour was similar to the contralateral lung.

Dataset lung 2 (Armato *et al.*,2015) contained 10 training cases and 60 testing cases. The following results show the investigation of 5 malignant cases and 5 benign cases from training dataset.

Patients	Diagnosis	Protocol Name	Tumour size in pixels	Number of Vessels in Vicinity of Tumour	Number of Vessels in Equivalent Area of Lung with No Tumour
1	Malignant	Thorax	8737	11	4
2	Malignant	Thorax	130	8	2
3	Malignant	Thorax	178	10	2
4	Malignant	Thorax	858	13	3
5	Malignant	Thorax	682	15	4
6	Benign	Thorax	65	5	4
7	Benign	Abdomen	2763	4	4
8	Benign	Thorax	495	6	5
9	Benign	Thorax	512	5	4
10	Benign	Thorax	612	9	8

Table 5.2: Shows the results of vessels number in five benign and five malignant tumours. Tumour size figures are pixels based.

As illustrated in table 5.2, the number of vessels in vicinity of lung tumour counted and compared with the number of vessels in corresponding area of contralateral lung. Ten tumour cases of five malignant and five benign were analysed. The size of a tumour was measured and depending on the purpose of the investigation, the protocols of each case were revealed. The number of vessels, however, was higher in the vicinity of lung tumour, as cases 1,2,3,4 and 5 were noted for the malignant tumours in the Table. However, the opposite trend was seen for benign tumour, with the number of vessels in the vicinity of lung tumour were near or similar to the number of vessels in contralateral lung with no tumour.

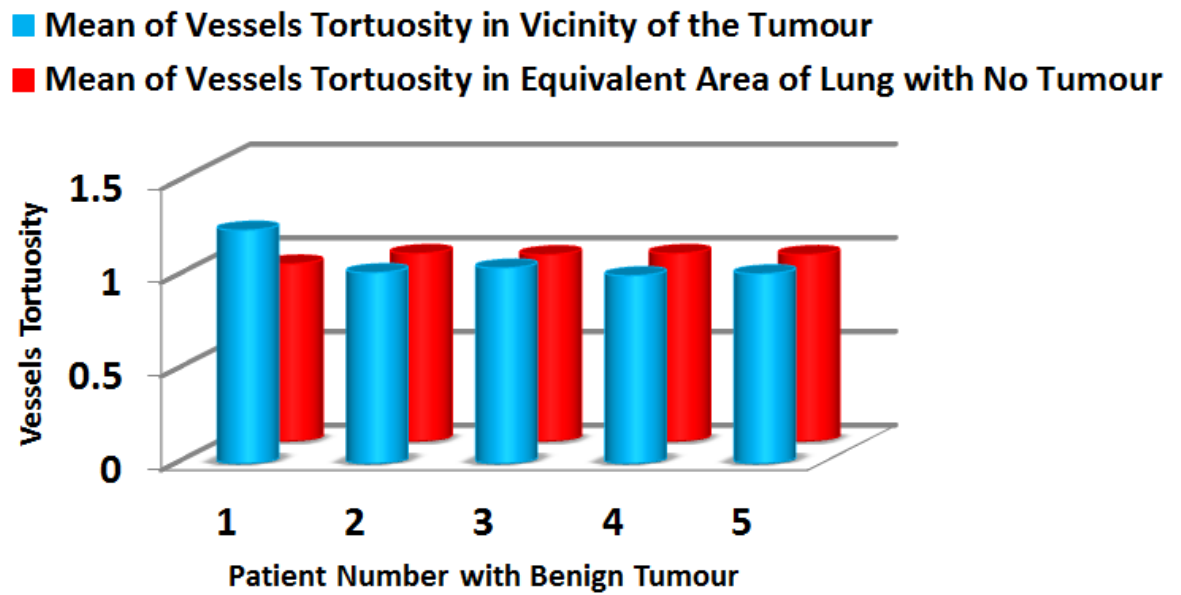


Figure 5.14: The mean of vessels tortuosity in the vicinity of benign lung tumour compared with mean of vessels tortuosity of contralateral lung with no tumour.

The bar chart in figure 5.14 demonstrates the mean of the tortuosity of the vessel-like structures in the vicinity of lung tumour. The mean of the tortuosity in the tumour side was similar to the mean of the vessel tortuosity in contralateral lung.

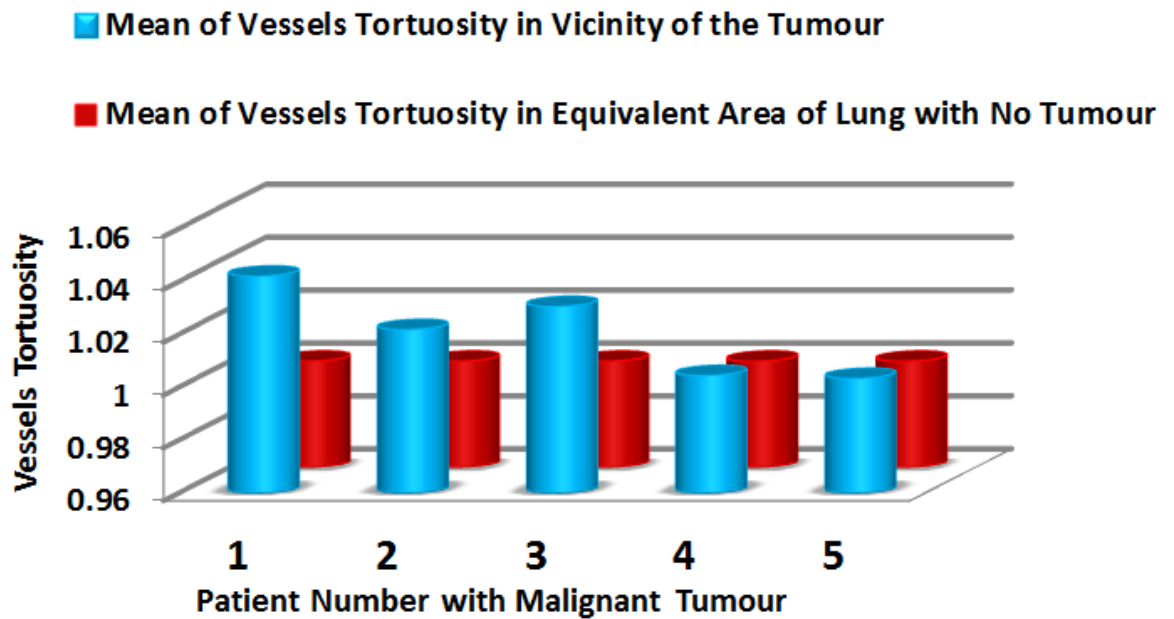


Figure 5.15: Illustration of the mean of vessels tortuosity in vicinity of malignant lung tumour compared with contralateral lung with no tumour.

The bar chart in figure 5.15 shows the mean of the tortuosity of the vessel-like structures in the vicinity of lung nodule. In cases of four and five, the mean of the tortuosity in the nodule side was close to the mean of the vessel tortuosity in contralateral lung with no tumour. In the first three cases, the tortuosity of vessels in the vicinity of lung tumour was higher compared with contralateral lung.

5.7 Summary

Lung cancer is the third most common cancer in the UK according to Cancer Research UK. This cancer is more common in males than females and is considered a major cause of cancer death (Nat, 2014). Tumours continue to create more vessels around them. However, in these cases with primary lung cancer, the proportion of vessels around the tumour side increased sharply.

This Chapter focuses on the investigation of vessel attributes using manual analysis in Lung CT images. However, the main objective was to investigate

the number of vessels in areas of unilateral lung tumours and to compare this with the equivalent contralateral lung without tumour. The size of tumour, vessels number and vessels length in order to calculate the tortuosity were measured using 2-dimensional slides of Lung CT images.

Two different types of lung CT scan datasets; Lung CT-Diagnosis and LUNGx Challenge were used. MATLAB software (The MathWorks Inc., USA) was used in order to display and analyse the DICOM images. Windowing was performed manually to clearly highlight and display the tumours as well as surrounding vessel-like structures.

Using the software, images were analysed and the number of clearly defined vessel-like structures in the vicinity of the tumour was counted and compared with the corresponding region in the contralateral lung with no evidence of a tumour; small vessel like structures and branches were not included. The area of a tumour was manually delineated and calculated in terms of pixels.

Ten sets of Lung CT-Diagnosis termed dataset1 with primary lung cancer were initially investigated. For each set of these CT images, one image was used where the tumour size was greatest. In all ten cases, the number of clear vessel-like structures in the immediate vicinity of a tumour was greater than that in the corresponding area on the contralateral side, mean and standard deviation of the difference were 5 and 1.39 respectively, and there was a significant difference $p < 0.001$. The mean of the vessel tortuosity of these ten cases with primary lung cancer on the side of a tumour was slightly higher with the value of 1.10 and 1.02 on opposite side.

For dataset lung 2, the LUNGx Challenge, formally known as the SPIE-AAPM-NCI Lung Nodule Classification Challenge the set consisted of 12 malignant and 11 benign cases were used. Investigation of these datasets revealed that the number of the vessels in the vicinity of a malignant tumour was significantly higher than that in the corresponding area on the contralateral side with no tumour with a significant difference $p < 0.001$ (t-test).

The mean of the vessels tortuosity of the tumour side and non-tumour side in twelve cases with primary lung cancer were 1.39 and 0.99 respectively, whereas the mean of vessels tortuosity of the tumour side and non-tumour side in eleven benign cases were 1.029 and 1 respectively.

5.8 Conclusions and Discussion

The primary concern for this chapter was the investigation of vessel attributes using visual analysis. This objective was to investigate the number of vessels in areas of unilateral lung tumours and to compare this with the equivalent contralateral lung without a tumour. The size of the tumour, vessels number and vessels length in order to calculate the tortuosity were measured using 2-dimensional slides of Lung CT images. Two different type of public dataset were used. Measurements from both datasets elaborated the significant results; as suggested the number of clear bright vessel-like structures in the immediate vicinity of a lung tumour may be higher than in the corresponding area on the contralateral side. The mean vessel tortuosity is slightly higher near a tumour compared to non-tumour side. This research merits further study to investigate if this approach may help enable early detection of lung tumours.

Chapter 6 Quantifying Vessel-like Structures in Lung CT Images

6.1 Introduction

THE final chapter in this thesis investigates and applies the image segmentation methodology to the blood vessels in lung CT images in order to facilitate the counting of the blood vessel and measuring their lengths and quantifying their tortuosity of the vessels.

As described in chapter 4 a mathematical morphology operation with linear structures was first applied to the thin structures of microscopic cilia images. This is now adapted to the similar features of vessel-like structures in the vicinity of lung tumours in CT images. The segmentation methodology has been applied to 2D slices of lung CT images that contain a tumour. Initially, the method enhances and segments the blood vessels then calculates the number and measures their lengths in order to find the tortuosity of the vessels.

Using such a computerized system will save time and allow clinicians to process a larger number of images. In this chapter, a semi-automatic algorithm is applied to illustrate a potential solution for the segmentation and quantification of lung vessel attributes.

The results of the manual analysis were then used to evaluate the semi-automatic segmentation of the algorithm. The ability to investigate the number of vessel and vessel tortuosity on high-resolution CT images may offer a new approach for early diagnosis of malignancy.

6.2 Literature Review

Different methods and vessel segmentation have been widely developed previously. In practice, a fast and accurate algorithm for blood vessel segmentation in CT images is still a challenging task in many applications (Han, 2012). Interactive segmentation plays a significant role in the analysis of medical images where users can import their expert knowledge as an additional source of information into the system (Rudyanto *et al.*, 2014).

Kiraly *et al.* proposed a lung vessel segmentation method by applying a global threshold operation to the lung region. Their intention was to find the location of pulmonary emboli and to investigate the characteristics of a local arterial tree and analysis of arterial sub-trees which are affected by pulmonary emboli. They segmented the entire lung vasculature by using global thresholding and labelling all connected component and eliminating small object (Kiraly *et al.*, 2004).

A simple morphological operation was another approach of blood vessel segmentation described by Eiho in 1997 (Eiho and Qian, 1997). Their aim was to obtain information about the shape and the place of the coronary artery tree. A top-hat operator was used to enhance the structure of blood vessels. Morphological erosion and half thresholding were used to remove the background. Finally, the vessel tree shape was extracted based on interactive user input that provided the specification of the root.

The common Hessian-based enhancement filter has been examined for the purpose of developing a blood vessel enhancement filter. This method enhances the vessels which look for local geometrical structures similar to tube-like structures by modelling the eigenvalues of the Hessian matrix, however, this algorithm was time-consuming in computing the data and the performance was poor along bifurcations (vessel branches). Frangi introduced a matched filter on thorax chest CT images. They proposed this new method because of Hessian-based filters, which are found to be

sensitive to noise, fail to detect smaller vessels and sometimes gives discontinuous vessels due to junction suppression. They applied matched filters in different directions, and local entropy thresholding, to gain more accurate analysis in noisy images to correctly extract the entire vessels. They extracted the lung region of an image based on grey level thresholding and morphological operations (Frangi *et al.*, 1998).

A parametric deformable (Terzopoulos *et al.*, 1987) model such as snake and level set models have been described. Approaches in this category may have difficulties in handling of finding the initial points, bifurcation and discontinuity of blood vessels. Therefore Yim described the graph searching technique based on an ordered region growing algorithm. The blood vessels tree structure was traced by specifying the endpoint and the origin of the vessel tree or by pruning the graph with a seed point. Ambiguities in vessel branching due to vessel overlap are effectively resolved by heuristic methods that incorporate a prior knowledge of bifurcation spacing (Yim *et al.*, 2000).

Valli *et al.* revealed a set of linear filters, which comprise the combination of the Gaussian distribution. They considered the blood vessel as a bar-like structure thus the enhancement was based on linear operators in various directions and widths. Their aim was to provide an algorithm for real-time vessel enhancement and they applied the method to real coronary arteriograms and synthetic images. To gain suitable results, the parameter space of the filters must be selected carefully. Their experimental results were shown following noise rejection and showed good sensitivity for the vessel detection (Valli *et al.*, 1997).

Zana *et al.* described a different method of morphology for detection of vessel-like objects in 2-D images. They defined blood vessels as a bright pattern, piecewise connected and locally linear. The method combined a rotating linear morphological operation followed by a cross-curvature analysis. Their aim was to segment the vessels from the background pattern (Zana *et al.*, 2001).

To extract segmented blood vessels, Chaudhuri et al. applied matched filters to segment the blood vessels in retinal images. The aim of the method was to examine the effect of the topological changes in the retinal vasculature on the hemodynamic distribution in the retinal circulation. The matched filter kernel was applied in 12 directions over 180° . The final resulting image was computed by taking the maximum response of the 12 filters at each location. They used the final threshold image results for producing a binary segmentation of the vasculature. The outcomes of the segmentation assist in partitioning the vessels to measure the tortuosity. Their results showed that tortuosity leads to an increase in the pressure drop and decrease in the blood velocity (Chaudhuri *et al.* 1989).

Ricci and Perfetti proposed the line operator to be applied to the green channel of the RGB retinal image. It was based on the evaluation of the mean grey level along lines with fixed length passing through the target pixel at different orientations. They also calculated the mean value of short orthogonal lines in order to reduce false positive. Finally, they used these values along the pixel intensity values to create features for a support vector machine to perform a supervised classification (Ricci *et al.*, 2007).

6.3 2-Dimensional Datasets

The objective is to segment the blood vessels in the vicinity of a lung tumour using the following steps. The proposed algorithm for image feature extraction and quantification of lung blood vessels were implemented in *MATLAB* (The MathWorks Inc., USA). To demonstrate this approach, a set of 80 cases of chest CT Images, which were described in chapter 5, containing pulmonary nodules were examined. 40 cases from lung1 and total of 40 cases from lung2 (20 cases with benign and 20 cases with a malignant tumour) were observed in summary the process consisted of:

Pre-processing followed by:

- ✚ *Windowing*
- ✚ *Extraction of lung region using a mask*
- ✚ *Vessel enhancement*
- ✚ *Thresholding*
- ✚ *Skeletonisation*
- ✚ *Branch removal*
- ✚ *Vessel refinement*
- ✚ *Endpoint identifications*
- ✚ *Vessel quantification*

6.3.1 Windowing (Histogram Adjustment)

Manual windowing was performed in order to highlight the blood vessel structure in the vicinity of lung tumours. CT images are represented by pixels with CT number in the approximate range of -1000 to 3000 for example 4000 levels of grey (Chaudhuri *et al.*, 1989). Hence a mapping of CT numbers into the values that are meaningful to the application is required. This was performed by a common technique in digital imaging called windowing. The windowing technique was used to highlight the vessels-like structure around a tumour, excluding the unwanted objects in the lung CT image. This was achieved manually by using the image processing tool viewer 'imtool' in MATLAB. Figure 6.1 illustrates the original CT image of a patient with a tumour in the left lung which was surrounded by many blood vessels. Image 6.1 (B) shows an example of manual windowing application to the image 6.1(A).

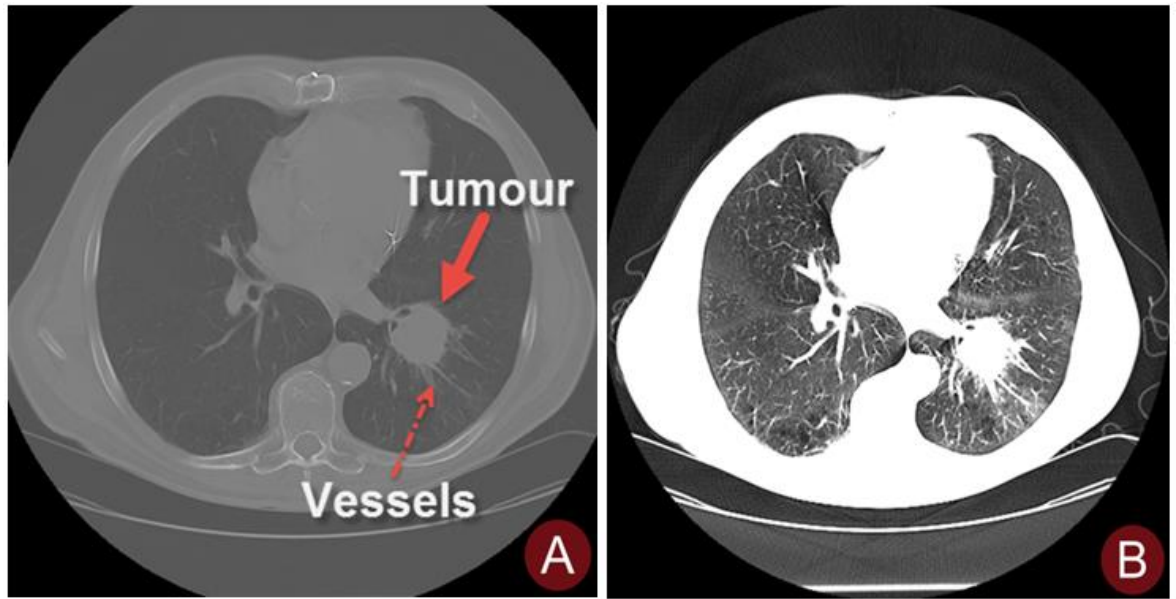


Figure 6.1: (A) Shows 2D contrast-enhanced CT images showing vessel-like structures in the lung (the image is from the original dataset). (B) Shows an enhanced view of vessel-like structures following specific windowing.

6.3.2 Extraction of Lung Region

To better detect vessel-like structures, a mask was created to aid the segmentation of the lung region. To segment, the lung region, a 2-dimensional slice of lung CT images was masked by thresholding at a level of 400, the pixel value of images had a range of value between 0 and 4094. Morphological operations, dilation and erosion are then applied on the segmented image in order to fill the holes appearing in the lung region and to remove the blood vessels in each image. At this point, the mask for each side was created by selecting the biggest object on each side of the image. Figure 6.2 illustrates mask result step by step procedure of how to achieve the mask.

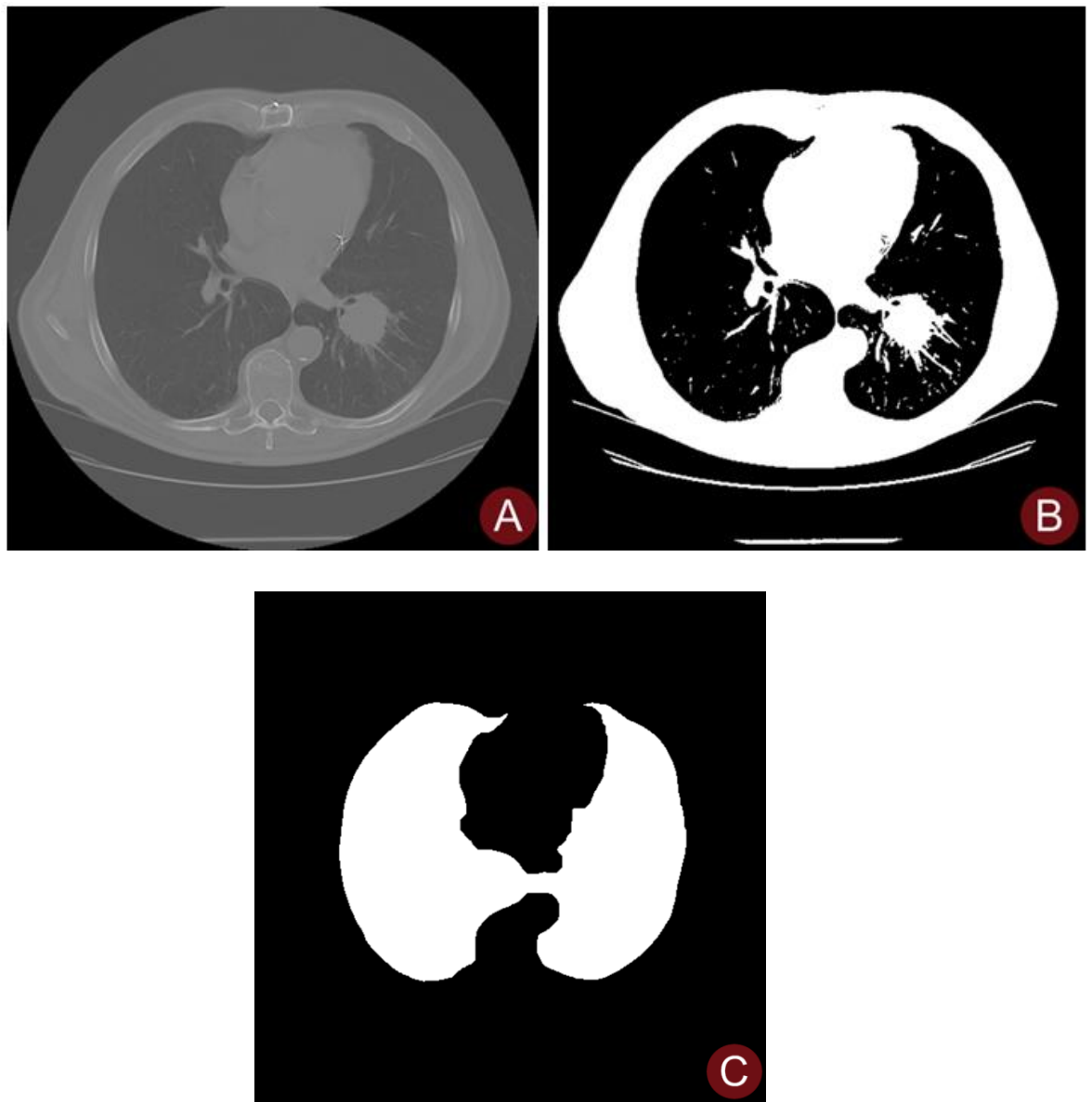


Figure 6.2: Extraction of processing of lung mask A) An axial slice of a chest CT image. B) Threshold image. C) mask image without any vessels.

6.3.3 Lung Vessel CT Image Enhancement

Enhancement algorithms are used to minimize image noise and increase the contrast of regions of interest. In this case, the enhancement technique assists in clarifying the vessel-like structures with higher contrast. Intensity variations in the background across the image deteriorate the performance of

the segmentation system. To remove this illumination gradient in the background, a shade correction technique was applied (Allisy-Roberts and Williams, 2007),(Niemeijer *et al.*, 2005). The shade correction technique was accomplished by estimating the background image and subtracting that from the original image. The background image was produced by filtering the windowed image, using a median filter. The value of the median filter was empirically chosen after trying a range of values. A kernel size of 10 x 10 was applied.

The opening of an image f is simply the erosion of image by structuring element $\$$, followed by the dilation of the result by structuring element. The opening of an image is defined as in equation 6.1 where f is an image and $\$$ is a structuring element.

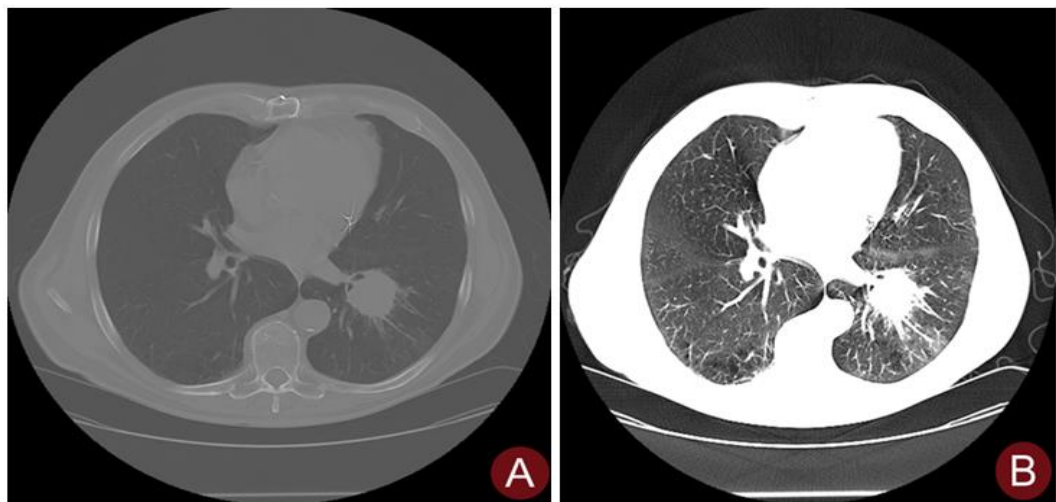
$$f \circ \$ = (f \ominus \$) \oplus \$$$

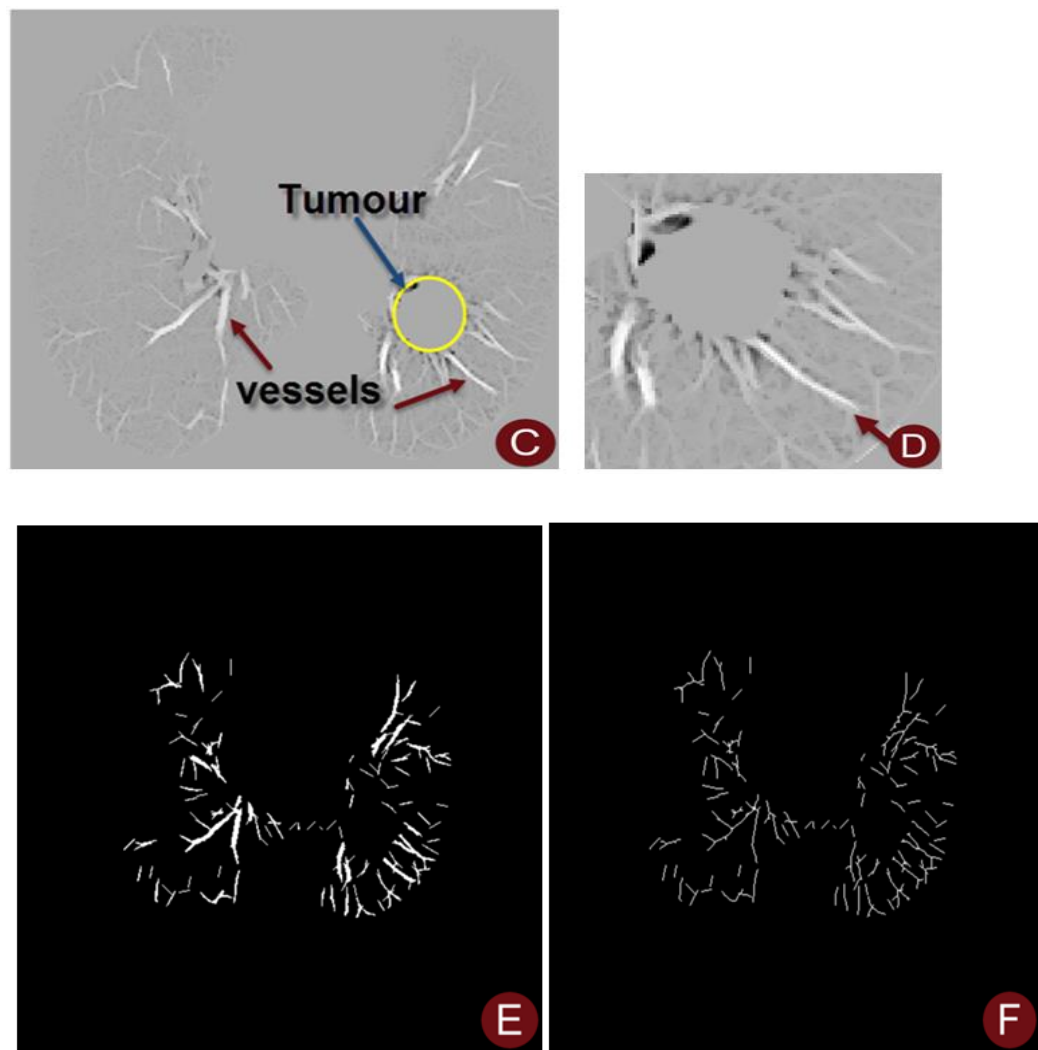
Equation 6.1

Once the background image has been estimated and removed, vessels are ready for further enhancement. A linear structuring element was used to enhance the vessels, that can be considered piecewise linear. A vessel enhancement method was performed by deploying a basic morphological operation using a linear structure and applied along vessels at different orientations. A basic morphological operation (Zwiggelaar, Parr and Taylor, 1996) of erosion followed by dilation gives a high degree of discrimination between circular and linear features of vessel-like structures (Frame *et al.*, 1998). This operation was applied to a structuring element oriented at 12 angles with 15 degrees angular resolution. This linear structuring element with the length of 12 pixels was then applied to perform the morphological operations. In each of the 12 images in different orientations, only those parts of the vasculature in which the linear structuring element can fit remain. The final resulting image was computed by taking the maximum response of the

12 filters at each location, with no nodular mass features present. Therefore, objects smaller than the linear structuring elements are diminished in intensity and those that can fully contain the structuring element are enhanced in intensity. The results identified an image containing mainly elongated structures of vessel-like structures in all orientations (Frame *et al.*, 1998).

Figure 6.3 shows the representation of this step by step procedure of the algorithm, windowing, basic morphological operation, segmentation, skeletonisation and endpoints. Figure 6.3 (C) shows the basic morphological operation of peripheral vessels in lung region of CT images. The results show vessels in the lung region have been enhanced with reasonable accuracy.





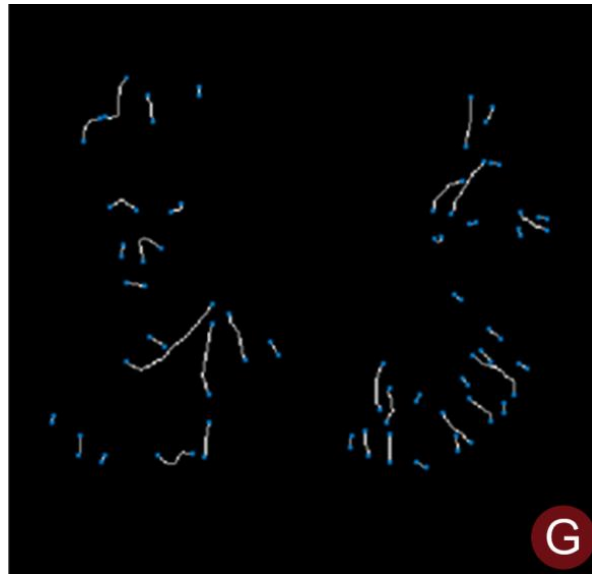


Figure 6.3: (A) 2D CT original image of peripheral vessels in the lung region. (B) highlights the blood vessels structure results obtained from windowing of (A). (C) Mathematical Morphology Enhancement of (B). (D) Zoomed-in image of (C). Tumour and enhanced vessels from a tumour. (E) Segmented image of (C). (F) Skeletonisation of (E). (G) Illustrates the endpoints of blood vessels with blue points.

Thresholding - An empirically derived threshold was found and applied to the enhanced image to produce a segmentation of vessels in lung CT images. The threshold was chosen in order to ensure that as many vessels as possible would be detected. The intention is to remove objects that are spurious and small vessels and branches for later analysis. The result in Figure 6.3 (E), illustrates; the segmentation of an enhanced image of figure 6.3(C). The vessels have been segmented appropriately, consequently, their features, such as a number of vessels in the vicinity of a tumour, length and tortuosity could be analysed. The length and the tortuosity can be calculated once the endpoints of the vessels are recorded.

Skeletonisation (Spencer *et al.*, 1996) is the result of the thinning process, which peels the contour of the vessel until a medial one-pixel width. **Skeletonisation** of vessels was performed enabling identifying points in the image where vessels cross and where vessel branching occurs. Branch

points and crossover points are located and removed from the skeleton network; this generates a number of blood vessel segments.

Segments less than 5 pixels are considered as noise and are removed. Thus measures of length and tortuosity can be calculated from the vessel segment. In order to reduce error from the measurements, small branches and spurs projecting from main vessels are removed without breaking up the vessel they branch from. Thus a step for spur removal was added prior to the removal of branch and crossover points. The skeletonisation results and end points are demonstrated in figure 6.3, (F) and (G) respectively. Results from the images of figure 6.3(F) and (G) assist in the further measurement of vessel features.

6.4 Semi-Automatic Quantification of Blood Vessel Attributes

A semi-automatic method was designed to speed up the user interaction while still performing most of the other tasks automatically. In the process of segmentation and branch removal, occasionally vessels are disconnected from their branch points. To produce accurate vessel lengths for tortuosity calculation the whole length of the vessel is required. This is based on the user's input which can then refine the vessel lengths. In this framework, the user only needs to select the endpoints of the vessels, and then the algorithm automatically reconstructs the disconnected vessels by using these points. The goal is to improve the performance of the segmentation to find the true length of the vessels. The algorithm reconstructs the vessel by using a popular cubic spline (Gonzalez and Woods, 2008.) technique. The spline constructed of piecewise third-order polynomials pass numerical data to create a smooth and continuous function.

A cubic spline was incorporated, uses the user input (points) to smoothly repair the disconnected vessels which they were disconnected by branch removal technique. Figure 6.3(G) shows the result of reconstructing the vessels by the spline technique. Endpoints of the vessels are shown by blue dots for a visual demonstration.

Chain code- The vessel lengths were calculated by applying a chain code (Bartels et al.,1987). The chain code is a boundary-based representation scheme composed of a connected sequence of straight-line segments of specified length and direction. The direction code of the chain code uses an eight-connectivity number scheme, as defined in figure 6.4.

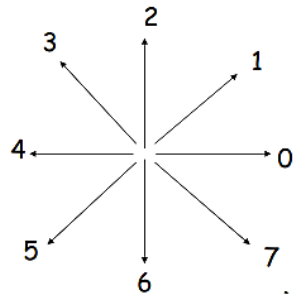


Figure 6.4: Chain code representation of 8 connections.

Tortuosity- Furthermore, measuring of the vessel tortuosity in the segmented image was calculated by the prevalent method called *arc to chord ratio*, is defined as equation 6.2:

$$T_{ortuosity} = \frac{Vessel\ Length}{Euclidiean\ distance}$$

Equation 6.2

The distance between two endpoints is calculated by using the Euclidean distance.

6.5 3D Visualisation of Vessels in Lung CT Images

Development in the medical image processing field has brought in the necessity of developing the capability of digital medical imaging modalities to 3D along with powerful digital imaging reconstruction and visualisation to help with better diagnosing and early treatment. 3-D visualisation helps specialists to choose their area of interest for scanning and this reduces the patient radiation exposure (Gonzalez *et al.*, 2008.).

The aim is to examine vessel-like structures including spicules in the vicinity of lung tumours using 3-dimensional visualisation including investigating the vicinity of a tumour in comparison with areas with no tumours. In order to examine the vessel-like structures in 3-dimensions, the bright structures corresponding to ribs were removed using software developed in MATLAB. Thus the technique was applied to 2-dimensional DICOM images of the lung in order to create new DICOM images which display the lung region including a tumour and vessels inside the region. To optimise the 3-dimensional visualisation of a lung tumour and vessels in its vicinity at different angles, the method extracted the lung region and removed the tissues outside the lung region. Therefore, initially, 2-dimensions lung CT images were imported into the MATLAB software and were thresholded to create the mask. The Mathematical Morphology operators, dilation follow by erosion were used to alter the mask to remove the tissues around the lung region. Finally, the manipulated 2-dimensional lung CT images are reassembled to illustrate a 3-dimensional presentation of a lung anatomical structure without any tissues outside of the lung. The 3-dimension visualisation of the lung images was performed with Amira version 6.3 (Thermo Fisher Scientific, USA).

Identification of lung's areas of interest was achieved by following steps;

- ✚ Import the series of 2-dimensional Dicom images.

```
X(:,:,1,p) = dicomread(filename);  
metadata= dicominfo(filename);
```

- ✚ Thresholding the image based on greyscale intensity to create a lung mask and filled the small holes.

```
B=X(:,:,1,p)>=400;  
tt=imfill(B,'hole');
```

- ✚ Apply mathematical morphology closing (dilation followed by erosion) to alter the mask.

```
dilate=imdilate(tt,strel('disk',16));  
bwarea=bwareaopen(dilate,600);  
erode_mask=imerode(bwarea,strel('disk',20));
```

- ✚ Save the modified image into Dicom image with the previous Dicom tags.

```
oo=int16(erode_mask).*int16(X(:,:,1,p));  
dicomwrite(oo(:,:,1,p),[FOLDER,filename,'.'],metadata);
```

The purpose of the preliminary processing is to remove the edge information not related to the lung area to reduce the complexity for better and further visualisation of 3-dimensional models. This process started with image thresholding according to the equation Equation 6.3.

$$J(x,y) = \begin{cases} 0 & \text{for } I(x,y) < T \\ 1 & \text{for } I(x,y) \geq T \end{cases}$$

Equation 6.3

Where:

$I(x,y)$ – The original Dicom image

$J(x,y)$ – *binary image resulted after thresholding to create a mask*

T – *Threshold value*

To remove the complexity of lung borders a sequence of the mathematical operations (with structuring element) were used as below;

- *Imfill* to fill the holes
- Dilation with a structuring element of disk
- Erosion with a structuring element of disk

The following images demonstrate an example of the step by step process for removing the edge of the lung areas. This was followed by the use of Amira software to construct the 3-dimensional model of the series of 2-dimensional lung images without lung areas border. Figure 6.5B shows a 2-dimensional image of the lung region following removal of the ribs. 6.5 A is an original image from the dataset, B displays the lung region without any surrounding tissues, C and D show a 3-dimensional visualisation of the data.



Figure 6.5: Illustrates the method applied to the series of 2-dimensional images of the lung. Image A shows an example of 2-dimensional original lung image. Image B presents the result of the threshold. Image C and D show the mask image and image without

tissues around the lung (applied masked on the original image). Image E and F are the results of a 3-dimensional model of the lung.

6.6 *Experimental Evaluation*

6.6.1 *Materials*

In this study, the algorithm was applied to two different sources of Lung CT images. These images are identical to those detailed in the previous chapter (section 5.4). The first dataset (lung 1) has 61 image sets of patients with primary lung adenocarcinoma. From this dataset 40 cases of them were analysed. The second dataset (lung 2) contains 70 image sets for the diagnostic classification of malignant and benign lung nodules. From the second datasets also 40 cases containing 20 benign tumours and 20 malignant tumours were analysed.

6.6.2 *Performance Measurements*

The performance of the algorithm was assessed on a larger database. Dataset one, patients with primary lung adenocarcinoma (Lung CT-Diagnosis) *dataset one*, for each set of CT images, one image was used where the tumour size was greatest; dataset two, LUNGx Challenge *dataset two*; the slide with a maximum size of a tumour was observed.

The algorithm was evaluated against the manual measurements. The algorithm enhanced and segmented the thin structure of vessels in order to count the number of vessels and calculate the vessels tortuosity in areas of unilateral lung tumours and to compare the results with the equivalent contralateral lung without tumour. The aim was to investigate the vessel-like structures in unilateral lung tumours and compare results between the lung with a tumour and the contralateral lung with no tumour. For each specific feature, the quantitative data of all cases was calculated in areas of unilateral

lung tumours and compare with the equivalent contralateral lung with no tumour.

The summary of the results of the algorithm applied on datasets obtained and represented by graphs. Bar charts, frequency distribution and scatter plot graphs were used. The Ryan-Joiner test was applied in Minitab v17 (Minitab Inc., USA) to examine the Normality of data. To prevent a repetition of the descriptions, blue bars and red bars on graphs refer to the tumour side and non-tumour side respectively. The number of vessels and vessels tortuosity were calculated in two separate areas; in the surrounding area of a tumour and entire lung region. These were then compared to the results of the corresponding side of the lung with no tumour.

6.7 Results

The validation about to be presented is investigated the system for detection of vessel-like structures of lung CT images. The validation was performed to compare the algorithm versus manual study in respect of the number of vessels detected in the vicinity of a lung tumour. The total number of vessels was counted, and the number of vessels detected by the algorithm in the vicinity of a lung tumour was counted corresponding to the visual analysis (Sadri *et al.*, 2017) The number of vessel-like structures from manual analysis compared with those detected by the algorithm. Therefore scatter graphs were plotted to compare the methods on CT images for 40 patients.

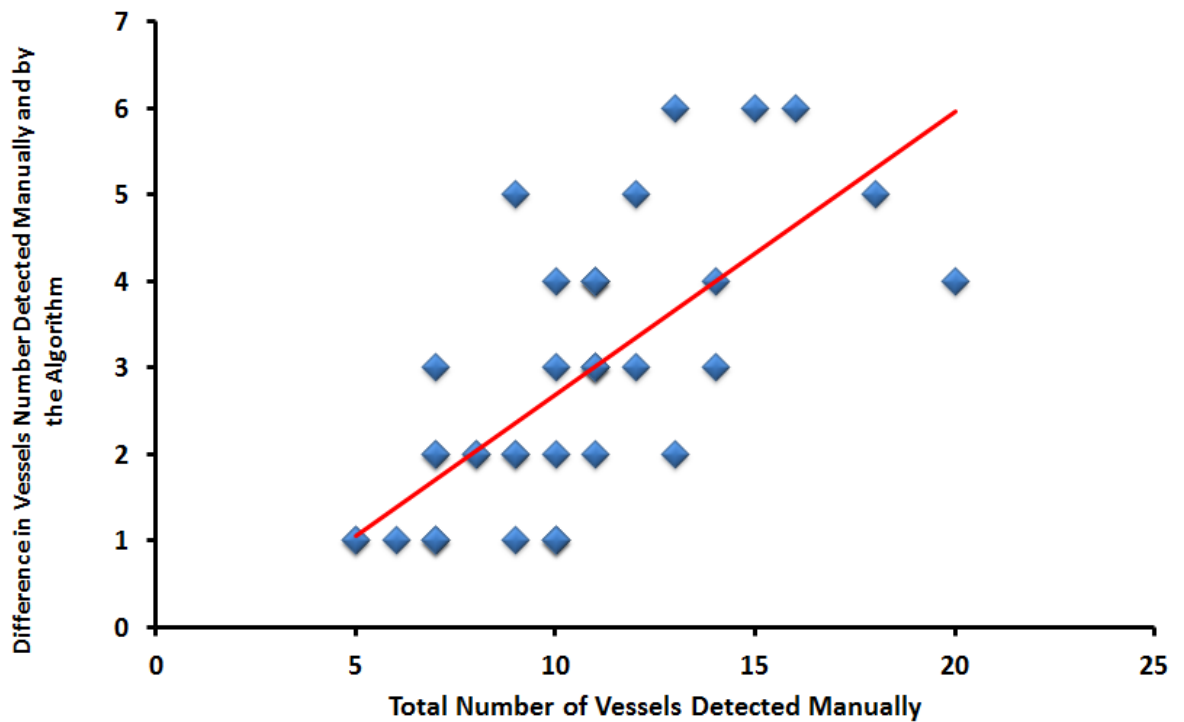


Figure 6.6: The scatter plot demonstrates the comparison between the difference of the number of vessel-like structures detected by the algorithm and visual analysis against the total number of vessels. The graph shows that there is an increasing and increased the number of vessels not detected with the total number of vessels.

The plot in figure 6.6, shows an apparent relationship between the difference in the vessel-like structures detected manually and those detected by the algorithm compared with the total number of vessels in the vicinity of a lung tumour. This shows the number of vessels not correctly detected increases with the total number of vessels ($r=0.69$) as might be expected.

6.7.1 Lung CT-Diagnosis in Tumour Area Dataset Lung1

The following sections demonstrate the results obtained from the algorithm.

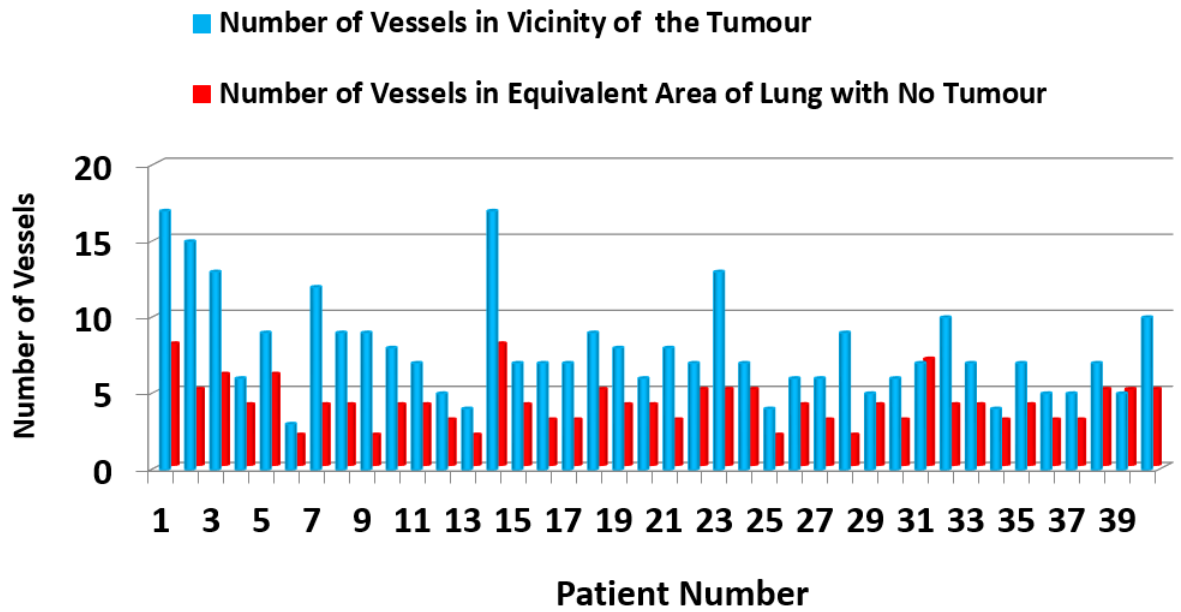


Figure 6.7: The bar chart displays the number of vessels in the area of the tumour. The blue bars are the number of vessels in the vicinity of a malignant tumour. The red bars are a number of vessels in the corresponding area of contralateral lung with no tumour.

The bar chart in figure 6.7 illustrates the population of vessels in the lung with a tumour and the lung with no tumour. The x-axis represents the number of cases of primary lung cancer and the y-axis represents the number of vessels detected in the vicinity of a tumour. Blue bars are consistently higher than the red bars in all but two of the 40 cases. In majority cases, blue bars are twice the value of the red bars, hence suggesting that the tumour area has more vessel-like structures.

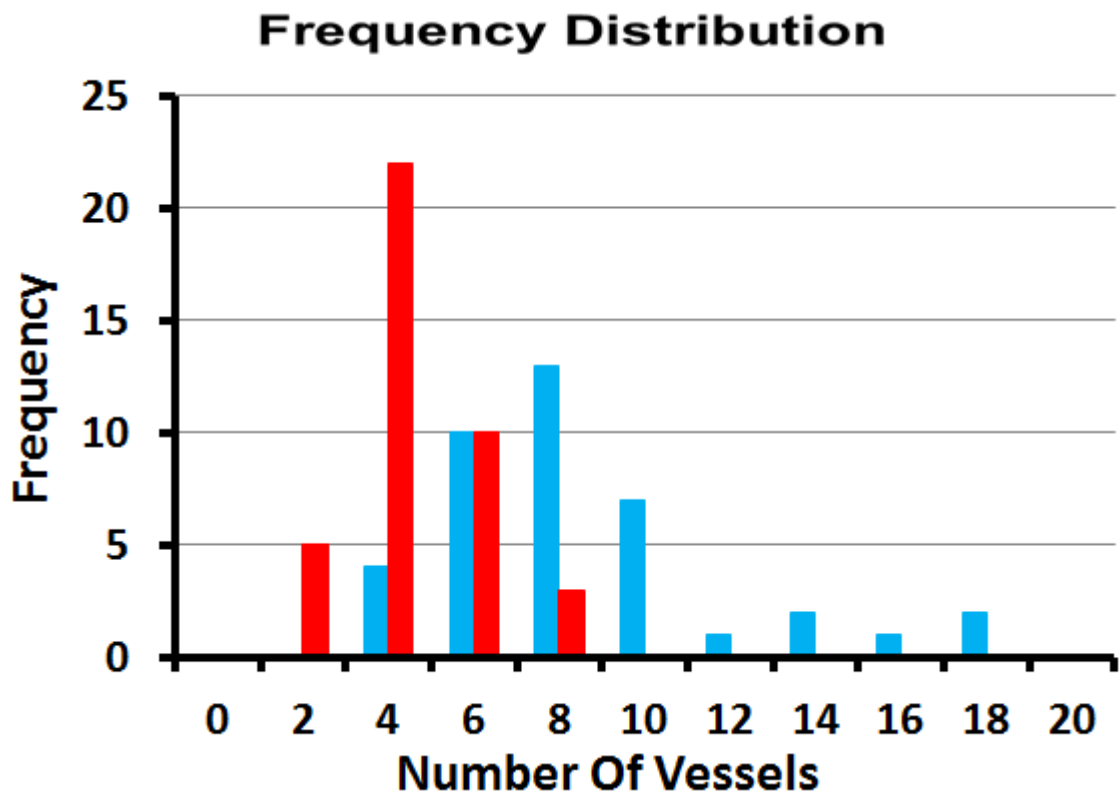


Figure 6.8: Frequency distribution graph illustrates the number of vessel-like structures in the immediate vicinity of a tumour (blue bars) and the corresponding area of the other lung with no tumour (Red bars).

The frequency distribution chart visually represents the distribution of a number of vessels in the immediate vicinity of a tumour and non-tumour side for the patients. In this figure 6.8, the x-axis is the number of vessels and the y-axis is the frequency (number of patients). The graph shows there is a difference between two distributions. The graph shows the distributions are shifted, which indicates the higher number of vessels on the side of a tumour.

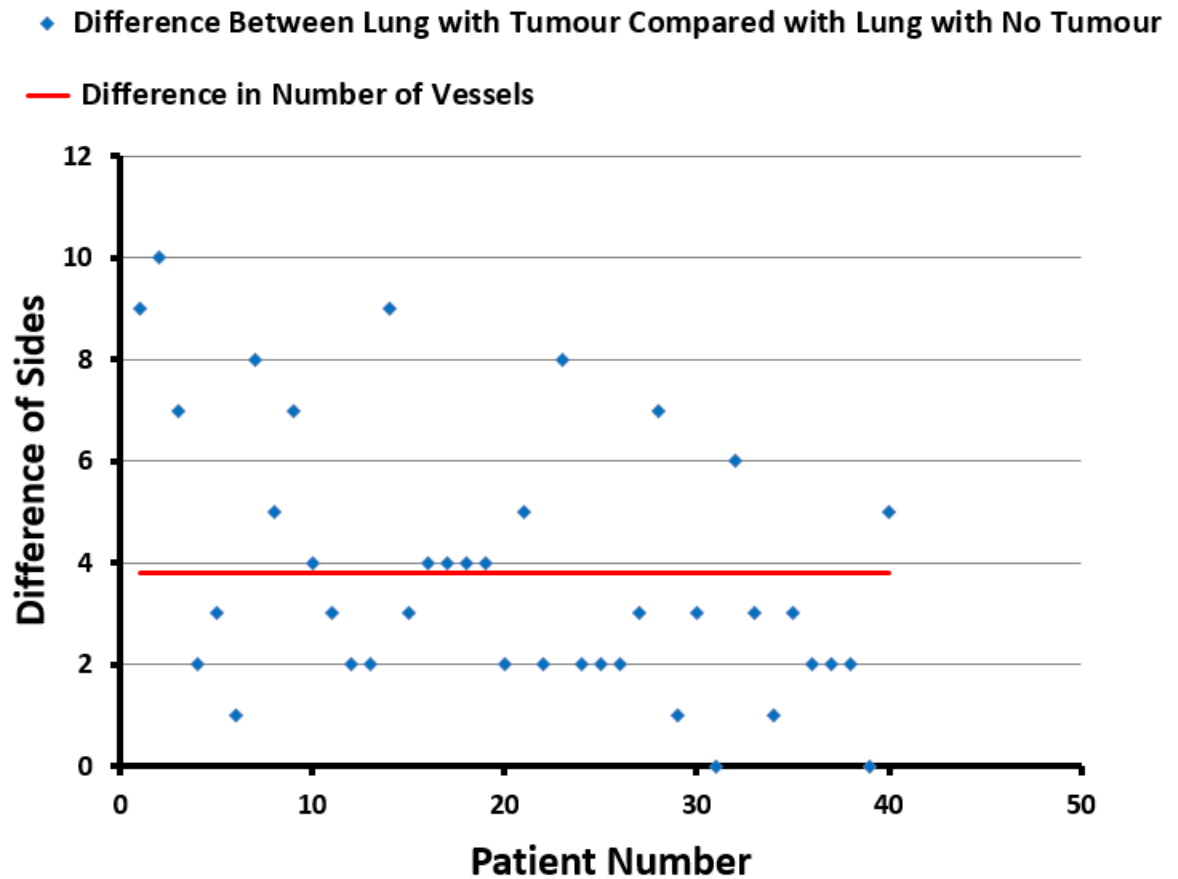


Figure 6.9: Scatter plot of the difference in a number of vessels in the immediate area of a tumour and the number of vessels in the equivalent area in the lung with no tumour. Redline is a mean of the differences.

As is also evident from figures 6.7 and 6.9 in the vast majority of cases there is a difference in the number of vessels between the tumour side and non-tumour side, with the tumour side having a higher number of vessel-like structures. Blue dots represent the difference between vessels in tumour side and non-tumour side for each patient. This plot was created to investigate these differences, and it can be seen that there is some variation and suggesting high variability. This is understandable considering factors such as what side the tumour is (right lung is bigger than the left lung) and the size of a tumour. The study shown from 40 patients with a malignant tumour, 19 tumours were in the left lung and 21 tumours were in the right lung.

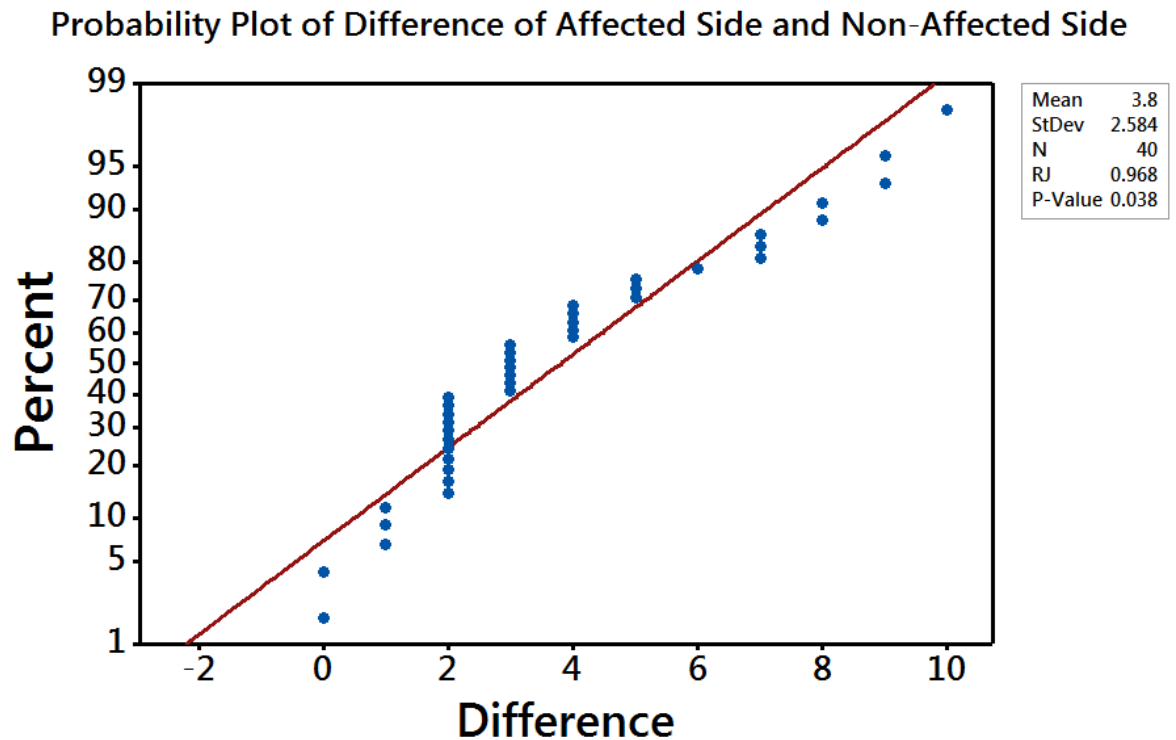


Figure 6.10: Normality plot of the difference of a number of vessels in the area of tumour and the number of vessels on the side of non- tumour.

The Ryan-Joiner test was applied in Minitab v17 (Minitab Inc., USA) to examine the normality of data. The difference of the population between the number of vessels in the area of a tumour in tumour side and non-tumour side are not normally distributed according to the figure 6.10. In this case, the p-value that was calculated was less than 0.1, therefore, a non-parametric test that is the Wilcoxon signed-rank test was used. The Wilcoxon signed-rank test indicated the number of vessel-like structures in the area of tumour was significantly different to the corresponding area of the non-tumour side $p < 0.001$.

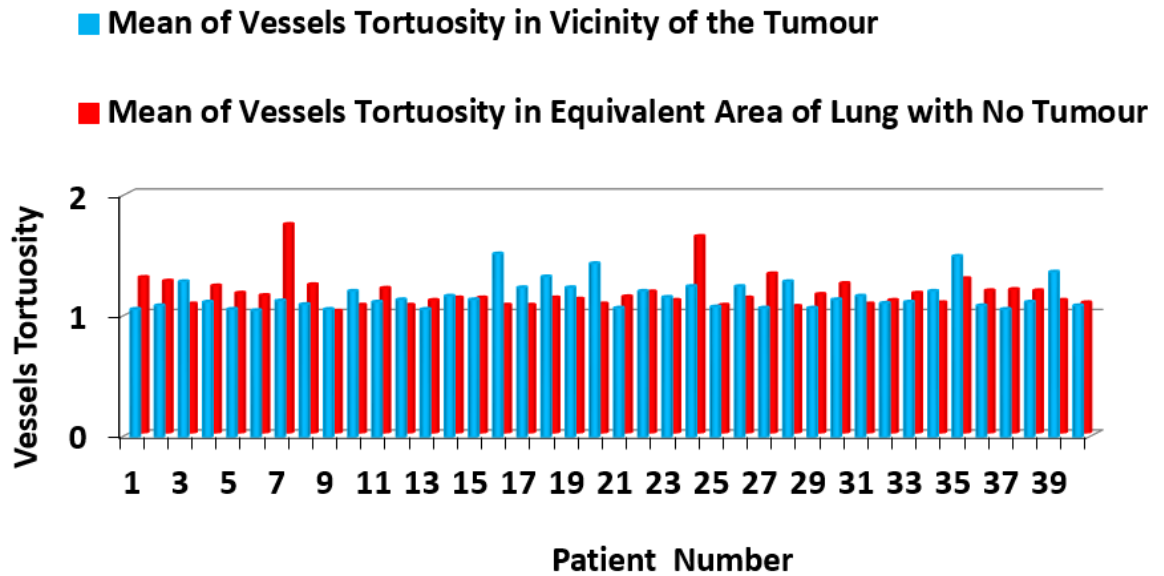


Figure 6.11: The mean of vessel tortuosity. Blue bars are mean of vessels tortuosity in the vicinity of a tumour and red bars are mean of vessels tortuosity in the corresponding area of contralateral lung with no tumour.

The bar chart in figure 6.11 demonstrates the tortuosity of vessels between the side with tumour and corresponding area of the opposite side with no-tumour. The x-axis presents the number of patients with the primary lung cancer and the y-axis represents the tortuosity of vessels. Blue and red bars display vessels tortuosity in the area of tumour and in the corresponding area of the opposite side with no tumour, suggesting similar tortuosity in the area of tumour and its corresponding area on the other side with no tumour.

The data were found to be consistent with a normal distribution and hence a t-test was applied. Using a t-test, there was no significant difference in vessel tortuosity in the area of tumour compared to the side with no tumour $p = 0.74$.

6.7.2 Lung CT-Diagnosis from Complete Lung Area Dataset Lung1

The previous section assessed the tumour area of the unilateral tumour side and corresponding area in the contralateral side with no tumour. That assessment was done in the small area around a tumour and revealed certain patterns. In this section, vessel structures were examined in the whole lung region. The system is designed in order to apply analysis to the entire lung region and quantify the vessel properties in both lungs. In this section, data are analysed from the region of the lung with a tumour and compared with an equivalent area in the contralateral side with no evidence of a lung tumour.

The algorithm was applied to the whole lung region in order to segment and quantify the vessel-like structure features of the lung.

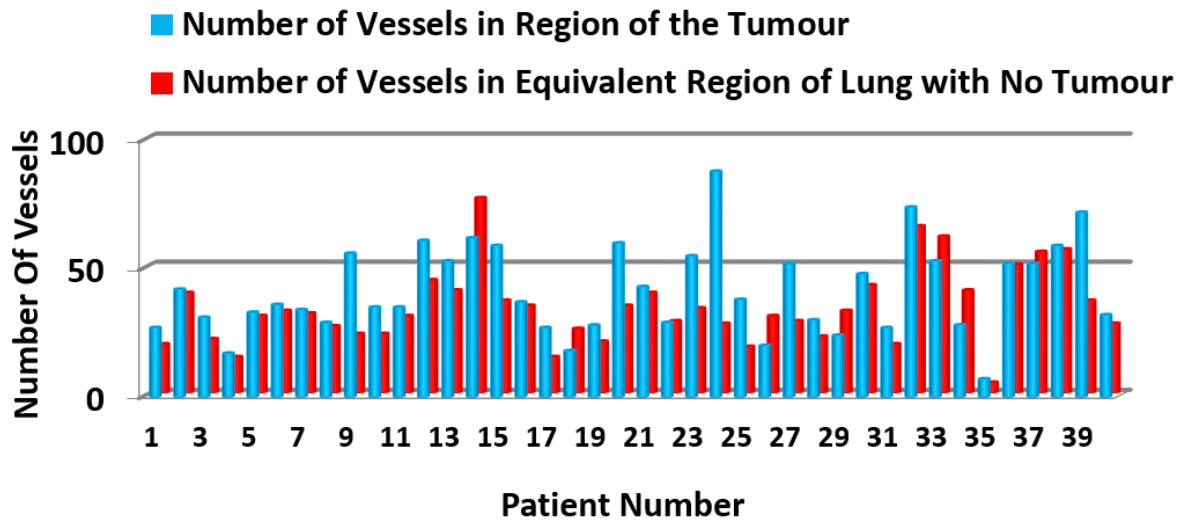


Figure 6.12: The bar chart displays the number of vessel-like structures. The blue bars are the number of vessels in the lung region of a malignant tumour. The red bars are a number of vessels in the corresponding area of contralateral lung with no tumour.

Figure 6.12 bar chart demonstrates the number of vessels in the entire region of tumour side compared to the region of opposite side with no-tumour for each case. The blue and red bars display vessels number in the entire region of lung with tumour and vessels number in the other region of opposite side with no tumour respectively; which shows the number of vessels in the whole region of the lung with a tumour is higher than the opposite side of the lung without any tumour.

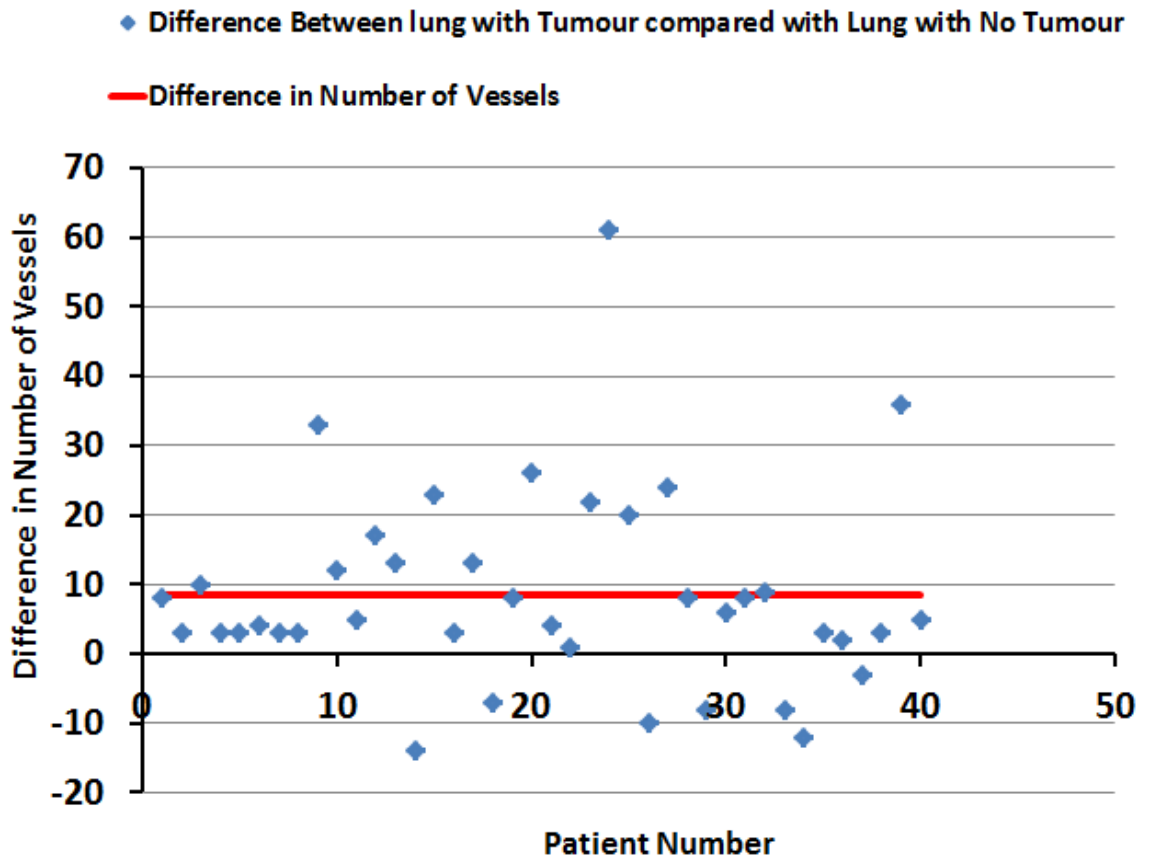


Figure 6.13: Scatter plot of the difference of a number of vessels in the region of lung tumour and the number of vessels in contralateral lung with no tumour. The red bar is a mean of the difference.

As seen also in the bar chart figures 6.12 and 6.13, demonstrate that for the vast majority of cases there are more vessels in the entire lung image and compared with the contralateral lung with no tumour. The tumour side has a higher number of vessels. This graph was plotted to acknowledge whether there was any consistency in these differences, however as it is clearly shown on the plot, the scattered data is not in close proximity to the mean line, suggesting high variability. There are a few negative values which indicate the numbers of vessels in the non-tumour side are greater than the tumour side. Ideally, everything should have been positive but considering factors such as what side the tumour is (right lung is bigger than the left lung) and the size of a tumour.

The data were found to be non-consistent with a normal distribution and hence a non-parametric Wilcoxon signed-rank test was used. It indicated that the number of vessel-like structures in the region of tumour was significantly different to the corresponding area of the non-tumour side with $p < 0.001$.

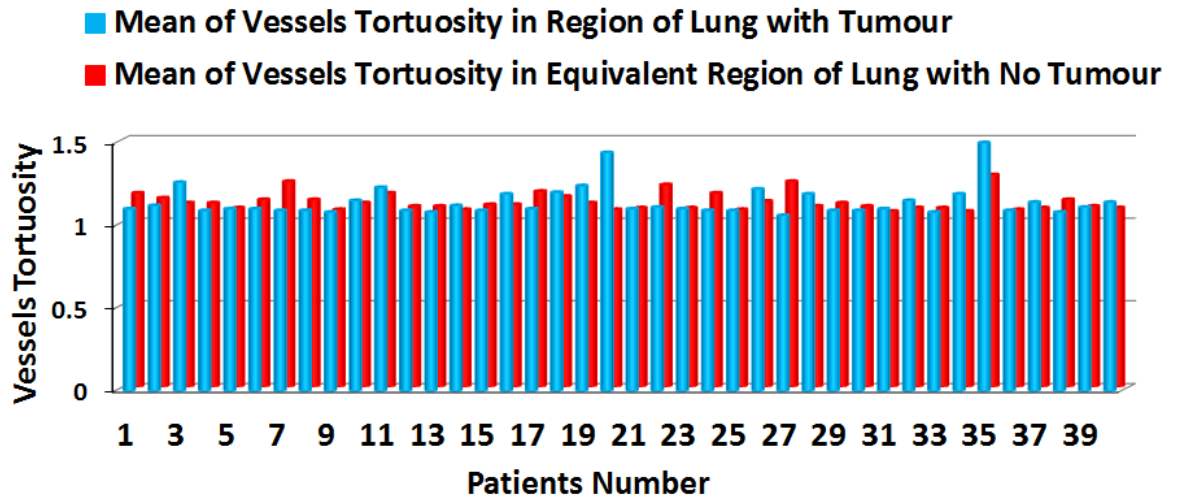


Figure 6.14: Vessels tortuosity in the entire region of lung in the tumour side (blue bars), vessels tortuosity in corresponding contralateral lung region with no tumour.

Figure 6.14, bar chart shows the tortuosity of the vessels in the entire region of tumour side and non-tumour side are following almost the same patterns. They all have a close range of tortuosity value. That means the vessels in tumour side of the lung region and non-tumour side are not tortuous due to the fact that those true lengths of the vessels are not visible to measure in 2-D.

The difference of the population between the mean of the vessels tortuosity in the region of lung tumour in tumour side and non-tumour side are not normally distributed. In this case, the p-value that was calculated was less than 0.1. Therefore, a nonparametric test that is the Wilcoxon signed-rank test was used. The test indicated the mean of the tortuosity of vessels in the region of a lung tumour was not significantly different to the corresponding region of the non-tumour side $p > 0.001$.

6.7.3 Lungx Challenge of Tumour Area – Dataset Lung 2

So far, the algorithm applied to the lung CT images of patients who had an only cancerous tumour. In order to expand and established the pattern achieved from previous results; the algorithm was applied to a set of data labelled by a specialist as a malignant or a benign tumour.

This section describes the results have been obtained in the area of the tumour of benign and the malignant tumours. To prevent repetition, the blue bars and the red bars are representing the tumour side and non- tumour side in all plots respectfully.

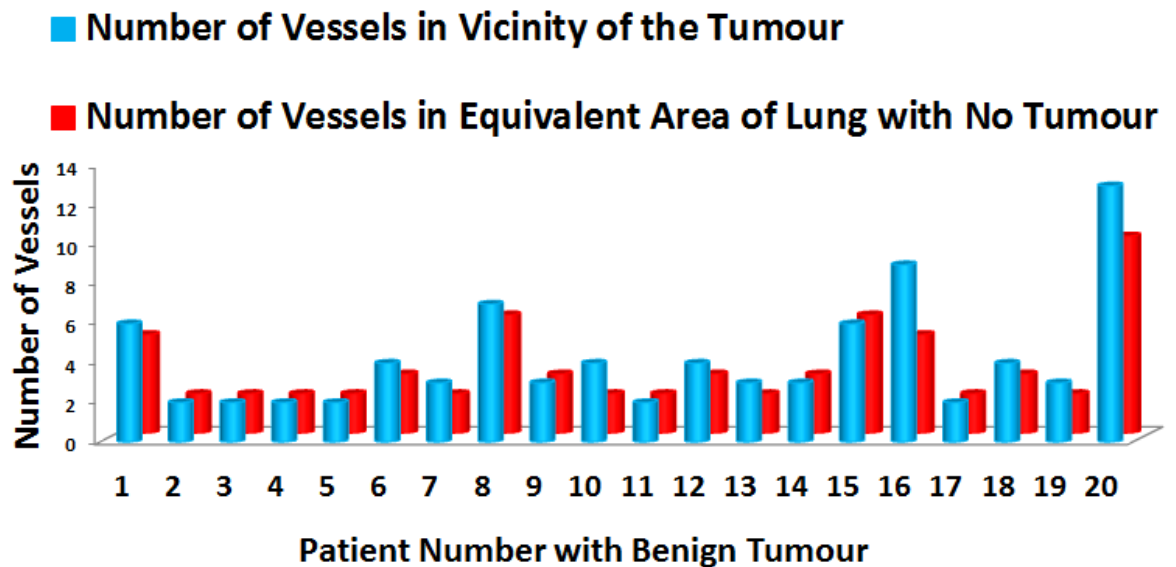


Figure 6.15: The bar chart displays the number of vessels. The blue bars display the number of vessels in the vicinity of a benign tumour and red bars show number of vessels in corresponding area of the lung with no tumour.

The graph in figure 6.15 illustrates a bar chart for the comparison of the number of the vessels in the area of tumour and non-tumour of 20 benign tumours. It can be seen that there is a little variance between the vessel-like structures in the vicinity of lung tumour compared with the contralateral lung with no tumour.

- ◆ Difference Between Lung with Tumour Compared with Lung with No Tumour
- Difference in Number of Vessels

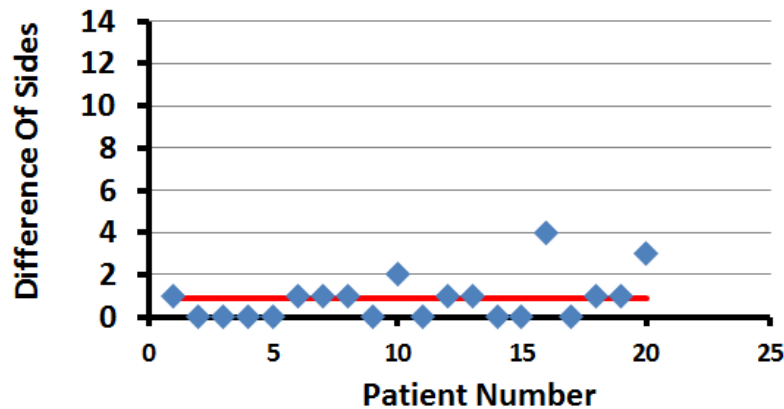


Figure 6.16: Scatter plot of the difference of a number of vessels in area of tumour (Benign) and the number of vessels in the equivalent area in the lung with no tumour. Redline is a mean of the difference.

Each data point in the scatter plot in figure 6.16 shows the difference between the number of vessels in affected side and non-affected side. The red line is the mean of the difference of vessels on both sides. These data points shown with blue dots are distributed close to the red mean line in the benign cases. Therefore, this distribution around the red line indicates there is not much difference between number of vessels in the vicinity of benign tumour and number of vessels in the corresponding area of contralateral lung with no tumour.

The data were found to be consistent with a normal distribution. Therefore, using a t-test, there was no significant difference in vessels number in the area of tumour in benign cases compared to the side with no tumour with $p=0.002$.

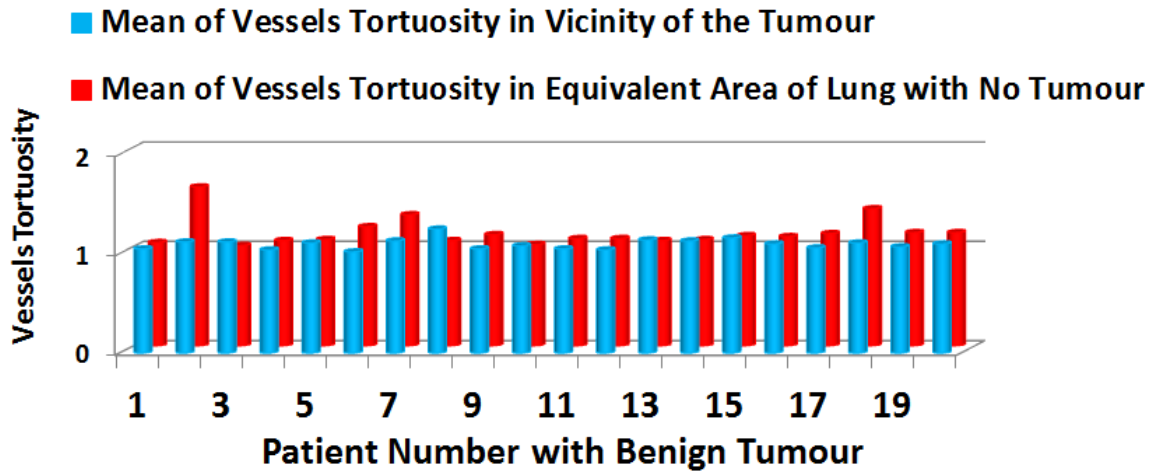


Figure 6.17: Bar chart displays the mean of vessels tortuosity. Blue bars are the mean of vessels tortuosity in the vicinity of benign lung tumour. Red bars are the mean of vessels tortuosity in contralateral lung with no tumour.

The mean of the vessels tortuosity in the area of tumour side and non-tumour side of benign cases demonstrated in figure 6.17 with no great difference. This indicated that there is no difference between the mean of the vessels tortuosity in the vicinity of benign tumour and the mean of vessels tortuosity in the corresponding area of contralateral lung with no tumour.

The difference between the mean of the vessels tortuosity in tumour side and the non-tumour side was not normally distributed. The p-value that was calculated was less than 0.1; therefore a non-parametric Wilcoxon signed-rank test was used. The Wilcoxon signed-rank test indicated the mean of vessels tortuosity in the benign tumour area were not significantly different to the mean of the vessels of corresponding area of non-tumour side $p > 0.001$.

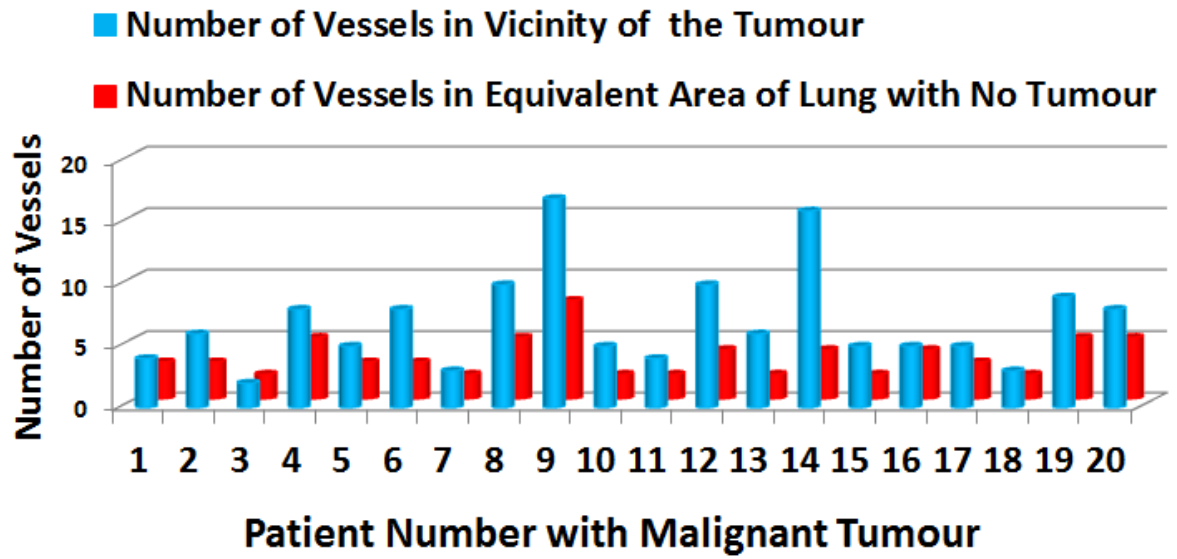


Figure 6.18: Bar chart displays the number of vessels in the area of malignant tumour (blue bars) and the number of vessels in corresponding area of contralateral lung with no tumour (red bars).

Figure 6.18 indicates the considerable variation of number of vessels in the vast majority of cases; there is a difference between the number of vessels in the vicinity of malignant tumour and number of vessels in the corresponding area of contralateral lung with no tumour. This was also correspondingly evident from figure 6.7 of lung1. Therefore the malignant tumours have a higher number of vessels in their affected area than contralateral side.

◆ Difference Between Lung with Tumour Compared with Lung with No Tumour
 — Difference in Number of Vessels

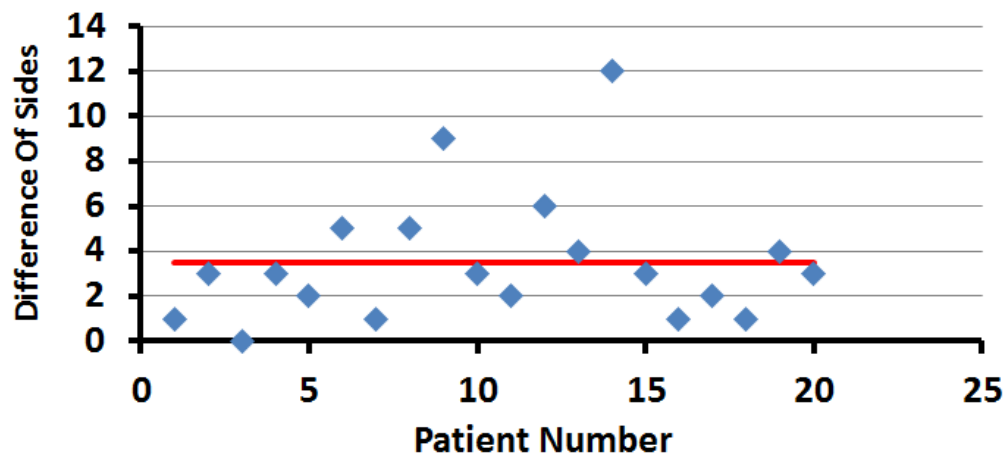


Figure 6.19: Scatter plot displays the difference of number of vessels in the area of a tumour (Malignant) and the number of vessels in the equivalent area in the lung with no tumour. Redline is a mean of the difference of vessels in tumour side and non-tumour side.

As likewise obvious from figure 6.18, Figure 6.19 demonstrates that for the clear majority of cases there is a difference in the number of vessels between the sides of tumour compared to the side of non-tumour, with the tumour side having a higher number of vessels. However, it can be seen from the data the difference of the vessels number in the affected area and the non-affected area is not in close proximity to the mean line, suggesting high variability.

The number of vessels in tumour side and the non-tumour side was not normally distributed. The p-value that was calculated was less than $p < 0.1$. Then the Wilcoxon signed-rank test was used. That indicated the number of vessel-like structures in the area of tumour in the tumour side was highly significantly different to the corresponding area of the non-tumour side with the $p < 0.001$.

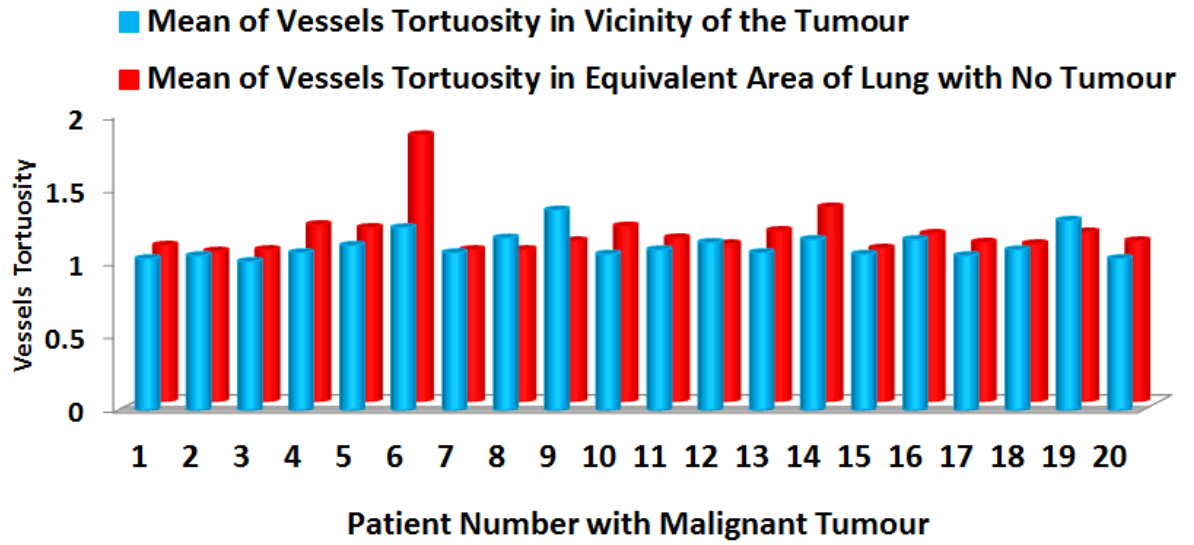


Figure 6.20: Bar chart displays the mean of vessels tortuosity in tumour side (blue bars) and non-tumour side in malignant cases (red bars).

The mean of tortuosity of vessel-like structures in the area of tumour in malignant cases was calculated as shown in figure 6.20, for many patients there was no big difference between the mean of tortuosity of tumour side and non-tumour side.

The difference between the mean of vessels in tumour side and the non-tumour side was not distributed normally. In this case, the p-value that was calculated was less than 0.1. Therefore non-parametric Wilcoxon test used and indicated no significant difference to the mean of the vessels tortuosity in tumour side compared with mean of vessels tortuosity in corresponding area of the non-tumour side with $p > 0.001$.

6.7.4 LUNGx Challenge from Complete Lung Area-Lung 2

Graphs following from this point on; are concerned with the whole lung region of tumour side and non-tumour side.

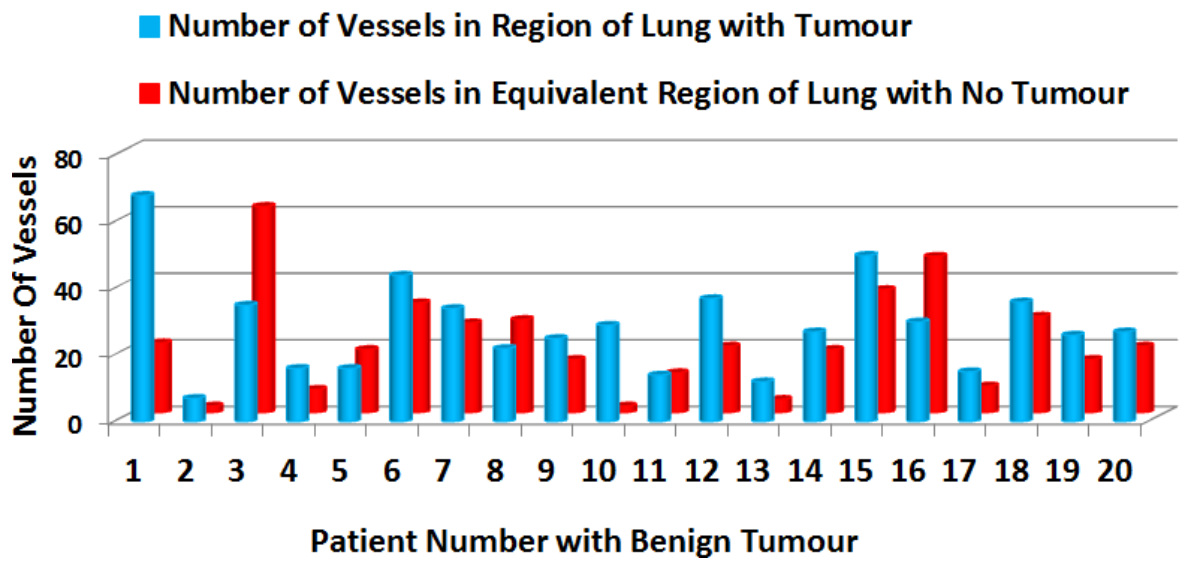


Figure 6.21: Bar chart shows the number of vessel-like structures of benign cases of the region of lung tumour (blue bars) and number of vessel-like structures in the corresponding region of contralateral lung with no tumour (red bars).

Figure 6.21 bar chart does not show any great difference in vessel-like structures in the region of benign lung tumour and number of vessel-like structures in the contralateral lung with no tumour.

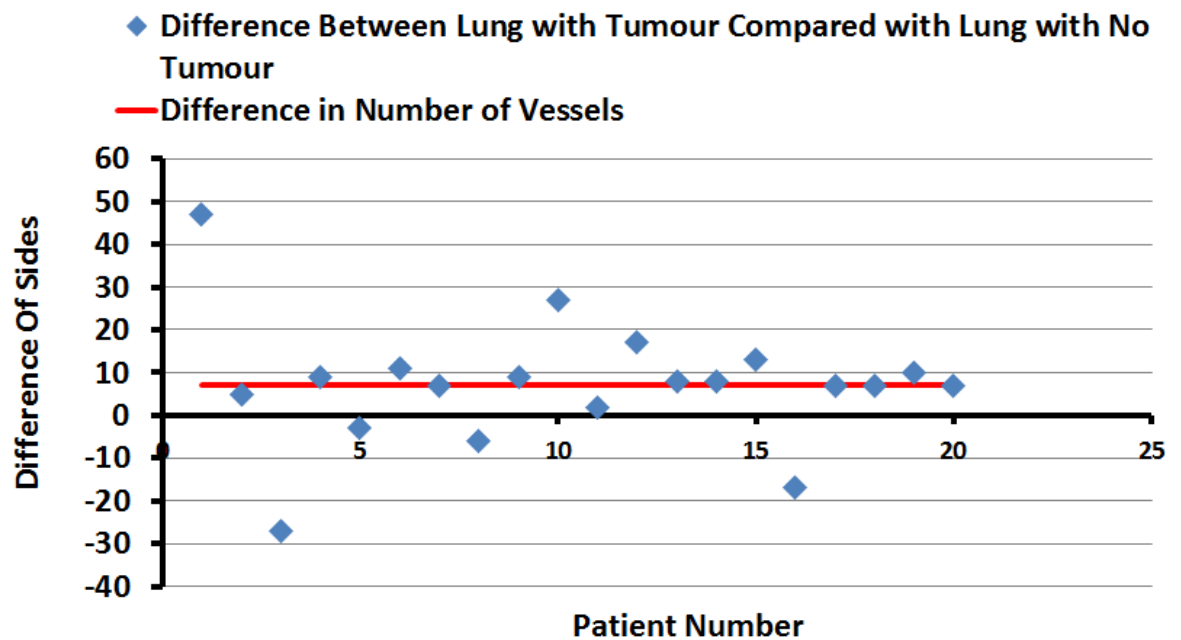


Figure 6.22: Scatter plot of the difference of number of vessel-like structure between tumour side and non-tumour side. Redline is a mean of difference.

In figure 6.22, scatter plot, the values obtained is the difference between the number of vessels between tumour side and non-tumour side of lung region in benign tumour. They presented a relatively even distribution either side of the red mean line. Also the difference between the number of vessels between tumour side and non-tumour side was presented in figure 6.15 and 6.16 in the vicinity of benign tumour that suggested the similar results. Therefore, to conclude that there is very inconsiderable variation between the sides of a tumour compared to the contralateral side with no tumour in benign cases.

The data were not distributed normally. Therefore, a non-parametric test that is the Wilcoxon signed-rank test was used. The Wilcoxon test result indicated the number of vessel-like structures in the lung region of a benign tumour was not significantly different to the corresponding area of the contralateral lung with no tumour $p > 0.001$.

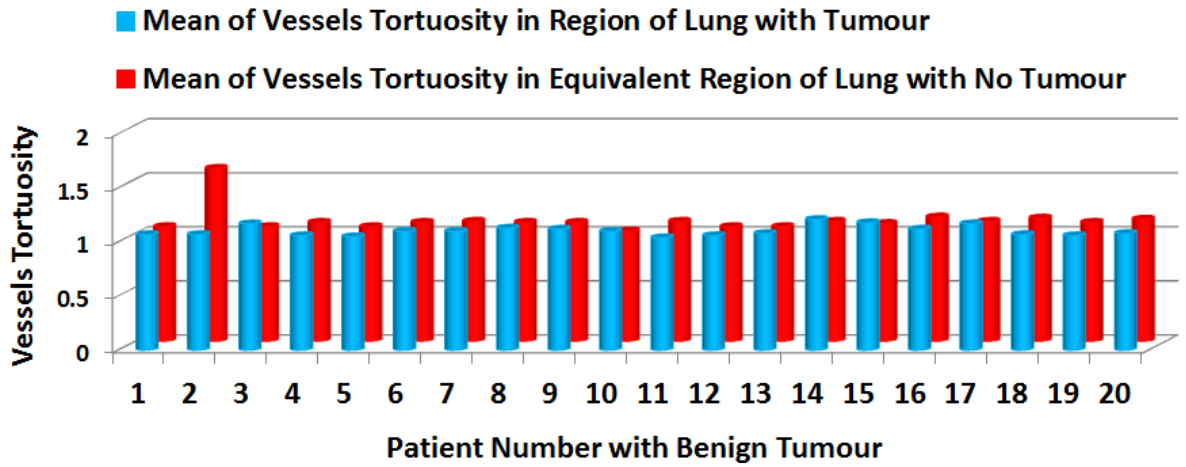


Figure 6.23: The bar chart describes the mean of the tortuosity of the tumour side of entire lung region (blue bars) and contralateral lung region with no tumour (red bars) in benign cases.

Figure 6.23, this graph shows there is no relevant discrepancy of the mean of vessel-like structures tortuosity in the entire lung region of the tumour side and non-tumour side in 20 benign cases. This is again another evidence to previous figure 6.17; that the mean of tortuosity in the area of tumour or lung region in tumour side is similar compared to the contralateral side with no tumour.

The difference of the mean of vessel-like structures was not normally distributed. Therefore, non-parametric Wilcoxon sign rank used, and the test was shown the mean of the vessels tortuosity in the region of entire lung tumour was not different to the mean of vessels tortuosity in the contralateral lung with no tumour with $p > 0.001$.

Now on the following graphs and explanations will be concentrated on the malignant tumour of the entire lung region.

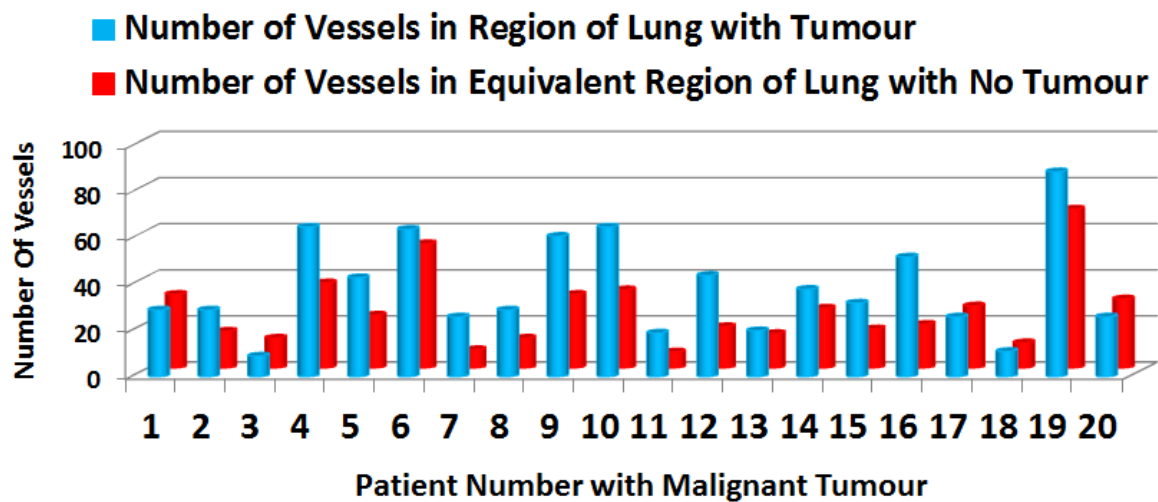


Figure 6.24: The bar chart illustrates the number of vessel-like structure in the entire of lung region of tumour side (blue bars) and corresponding contralateral lung with no tumour (red bars) in malignant cases.

According to the bar chart in figure 6.24 and bar chart in figure 6.18 (in the vicinity of tumour only) the number of vessel-like structures in the region of a lung tumour is higher compared with the corresponding region in contralateral lung with no tumour.

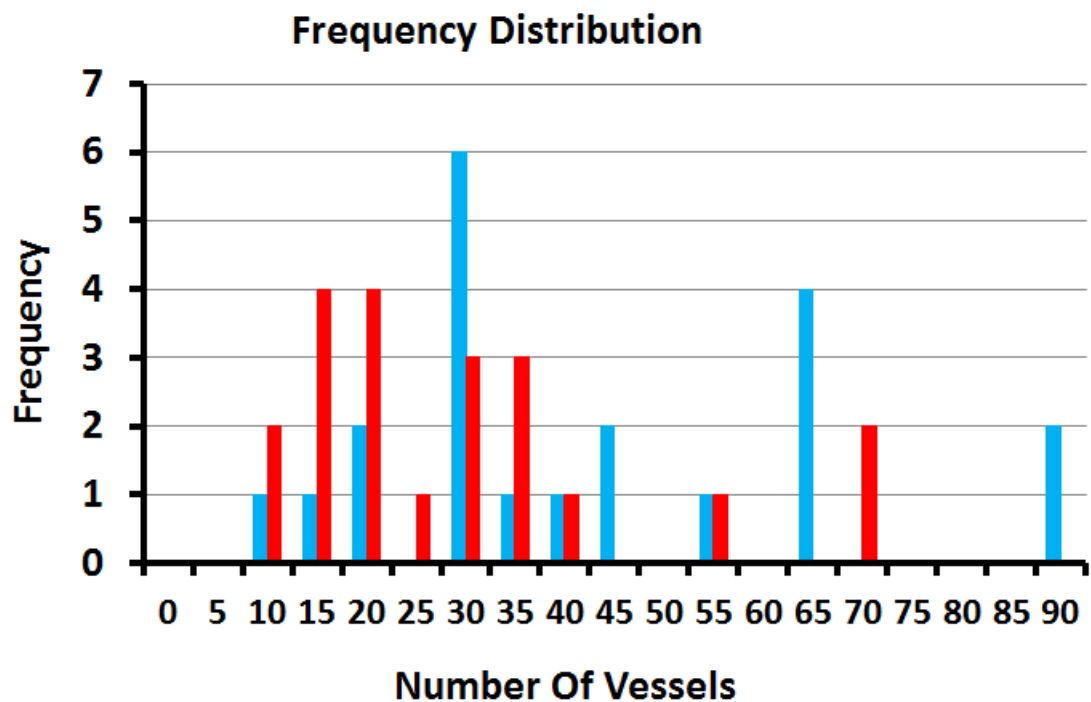


Figure 6.25: The frequency distribution of the number of vessel-like structures in the region of malignant tumour (blue bars) and opposite side with no tumour (red bars).

from the graph in figure 6.25, the frequency distribution number of vessel-like structures in the region of the lung with a malignant tumour shows the considerable distribution on the side of tumour (blue bars). As has shown the blue bars are moved along side of the x-axis. This suggests that the number of vessel-like structure in the lung region of malignant tumour was higher than the equivalent region in the lung with no tumour.

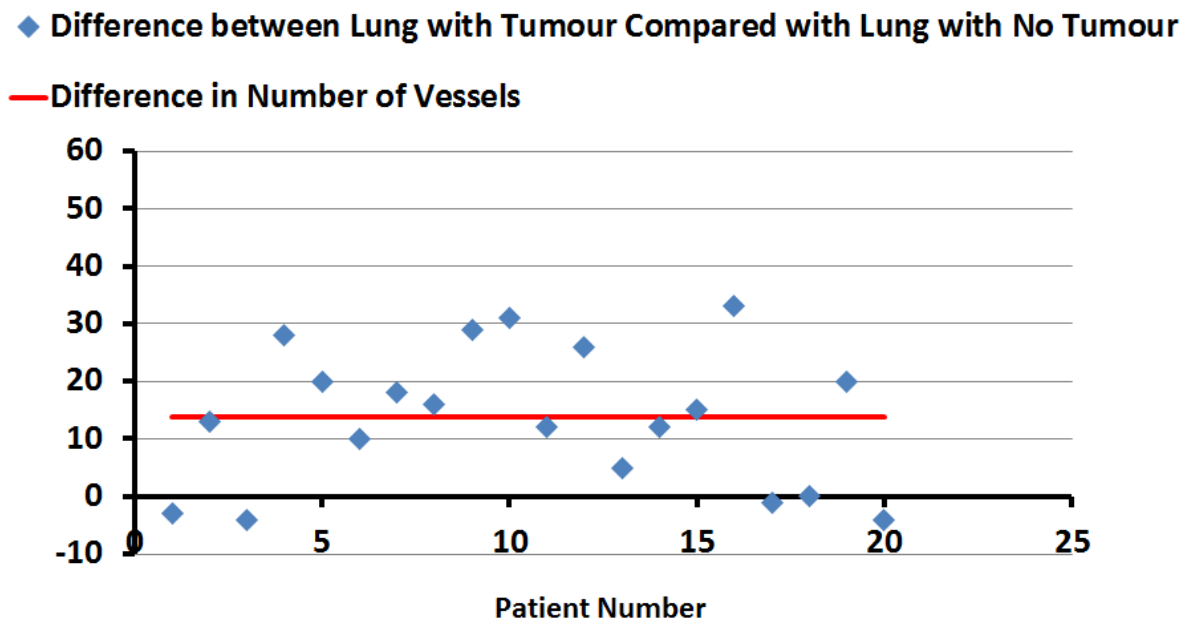


Figure 6.26: The scatter plot of the difference in number of vessels in the entire region of a lung tumour and number of vessels in the equivalent area in the lung with no tumour. Redline is a mean of differences.

The scatter plot in figure 6.26 illustrates the significant variation above and below the red mean line. Blue dots represent the difference between vessels in tumour side and non-tumour side for each patient. This indicated there is a difference in the number of vessels between the tumour side and non-tumour side, with the tumour side having a higher number of vessel-like structures in malignant cases.

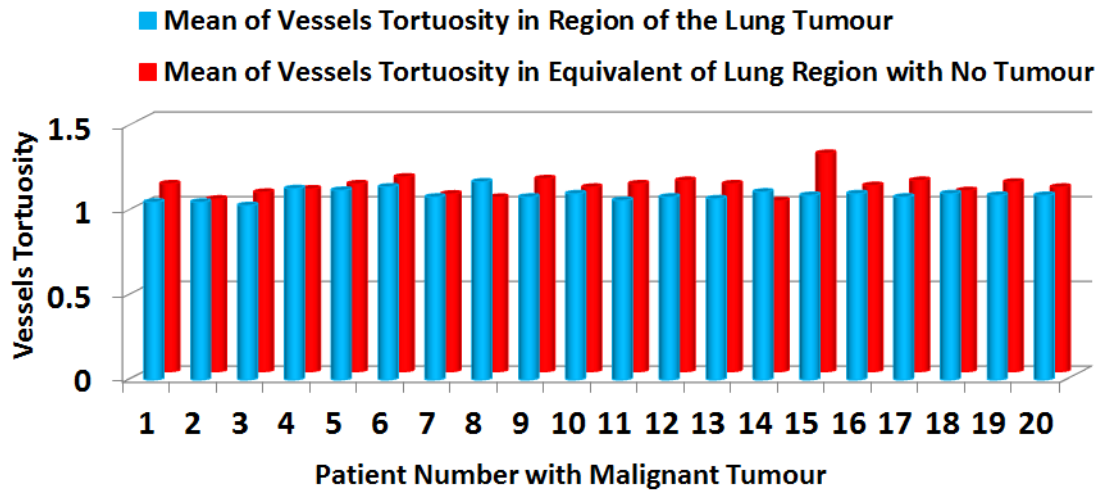


Figure 6.27: The bar chart plot shows the mean of the vessels tortuosity of lung region (blue bars) in tumour side and non-tumour side (red bars).

The bar chart in figure 6.27 indicating that mean of tortuosity of vessel-like structures in the lung region of a malignant tumour compared with contralateral lung with no tumour was not a great variation.

The non-parametric Wilcoxon sign rank test was used because the difference of the mean of tortuosity of vessel-like structures in the lung region of tumour in tumour side and non-tumour side are not normally distributed. In this case, the p-value that was calculated was less than 0.1. The Wilcoxon signed-rank test calculated and indicated the mean of vessel-like structures in the region of lung tumour compared to the corresponding area of the non-tumour side was not significantly different with the $p > 0.001$.

6.7.5 Experimental Results of 3-Dimensional Visualization

The proposed mathematical morphology operator was used and applied on series of 2- dimensional lung CT images with tumour. This was performed to remove the surrounding neighbouring area of the lung region for visual investigation. 3-dimensional visualization was performed on a whole series image of patient addition to the 2-dimensional analysis. This was performed by the algorithm was developed in MATLAB. The aim was to visually investigate the vessel-like structures in the lung associated with a tumour. Results of 3- dimensional were corroborated similar pattern to the 2-dimensional dataset.

The figure 6.28 illustrated the 3-dimensional visualization of the 2-dimensional series of a particular patient in a different angle. A tumour is in the left lung, showing the vessel-like structures in the vicinity of a tumour. It can be confirmed that the number of vessel-like structures and spicules in the vicinity of a lung tumour are much higher compared with the non-tumour side.

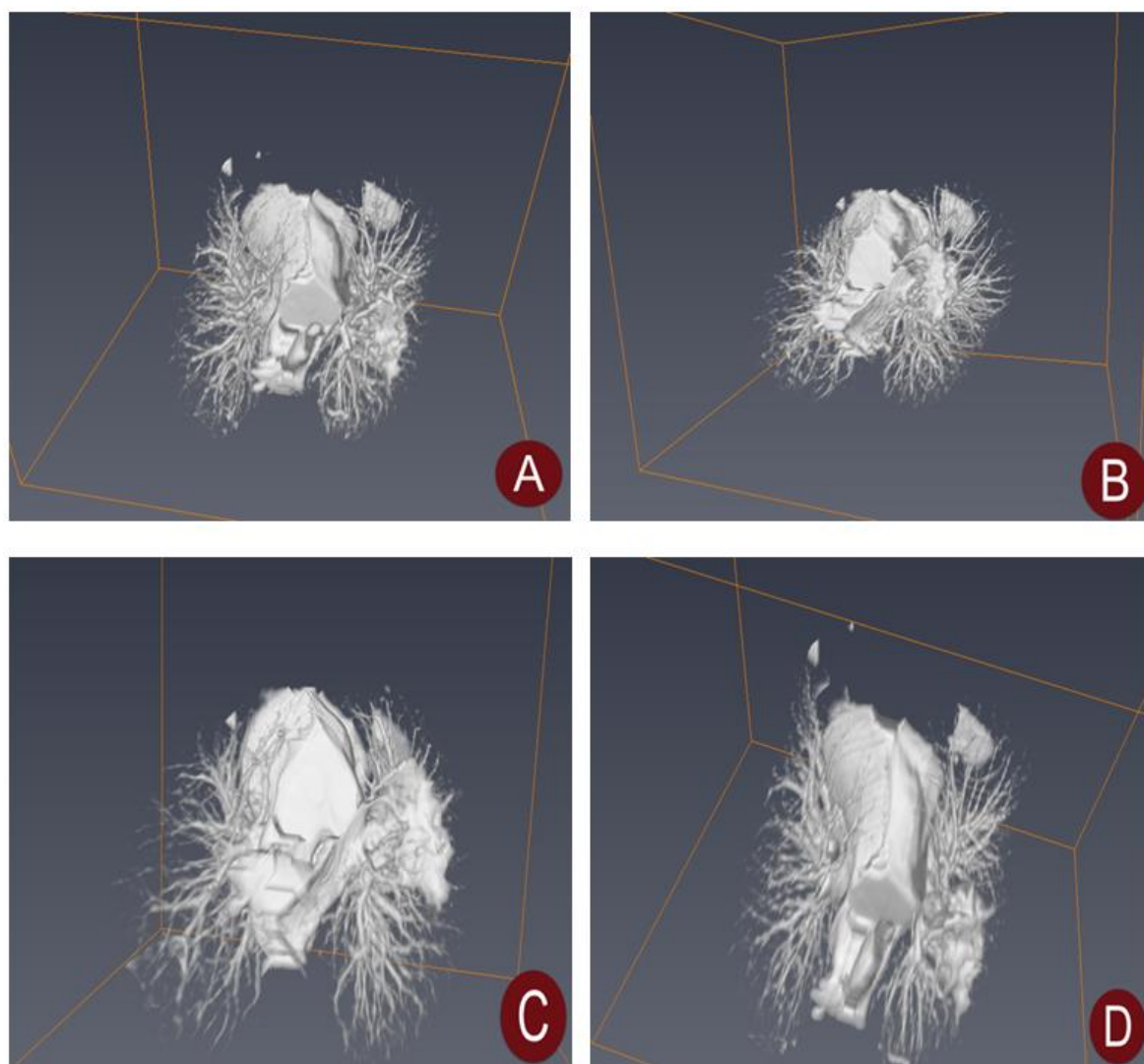


Figure 6.28: 3-dimensional visualisation of a patient with a malignant tumour at different angles.

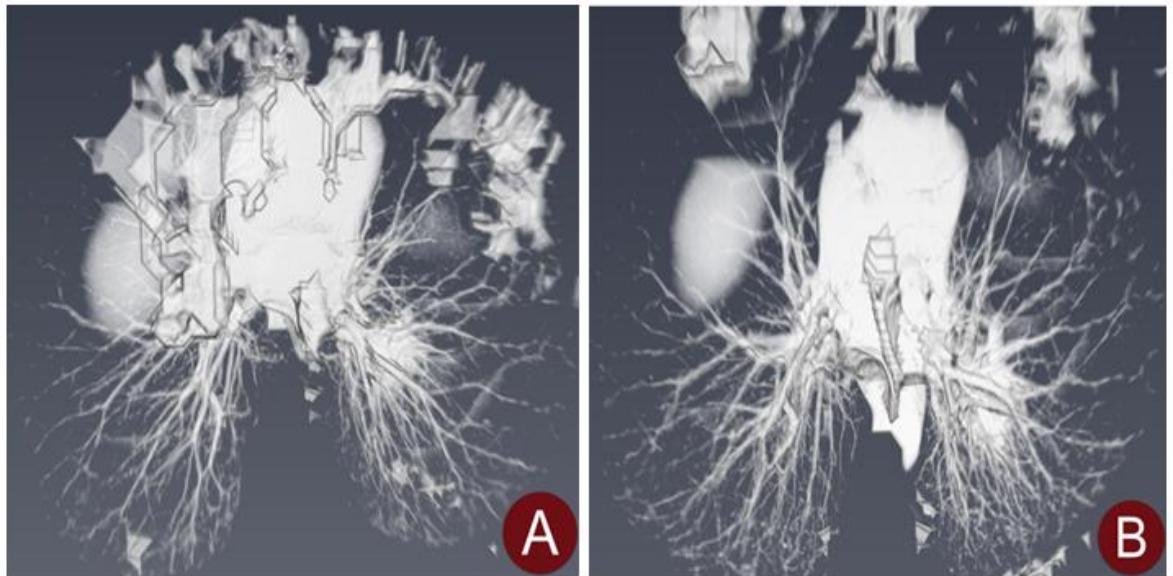


Figure 6.29: 3-dimensional visualisation of another patient with a malignant tumour at different angles.

The figure 6.29 shows the 3-dimensional model of another patient with malignant tumour. A tumour is on left lung and the number of vessels in the vicinity of a tumour in left lung compare to the right lung is much greater.

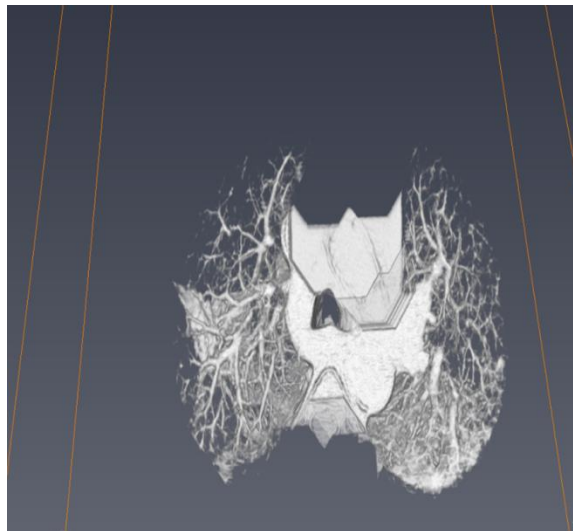


Figure 6.30: A 3-dimensional model of a patient with a tumour presented at the right lung.

Figure 6.30 demonstrated the 3-dimensional image of a patient that the tumour is presented in the right lung. This image shows the numbers of

vessel-like structures in the vicinity of lung tumour in right lung compares to the number of vessels in the equivalent area of left lung are greater.

6.8 Summary

Lung cancer is a prevalent disease that has a poor prognosis. Lung cancer may be present as a straightforward speculated mass. A nodule size >3 cm is associated with malignancy (Landini L., Positano V. and Santarelli M.F, 2008). If a tumour is speculated as malignant although 11% of malignant nodules do have distinct margins (Zerhouni *et al.*, 1986). A tumour plays an important role in changing the feature of the blood vessels (Viggiano, Swensen and Rosenow, 1992). Therefore, investigation and observation of lung blood vessels feature is vital and can help in early diagnosing of lung disease. These vessels feature investigation may help to predict the early stage of a tumour. Detecting vessels may help specialist to predict of the early stage of a tumour before a tumour is off sizeable amount to be detected outright.

Cross-sectional of imaging is the main radiological assessment of lung mass. Prior to diagnosing and treatment, specialists must read a large amount of lung CT images, and they are likely to overlook some vessels in the vicinity of a tumour, because of detection error or interpretation error. In this circumstance, computer-based automatic blood vessel segmentation is an efficient way to segment the lung blood vessels near a tumour.

In this chapter, the algorithm proposed was applied to the lung CT images of patients with a malignant and benign tumour. The objective of this research was to investigate the property of the lung vessels such as a number of vessels and the tortuosity of the vessels in the vicinity of a tumour in the unilateral side of the tumour and compare it to the corresponding area of the contralateral side with no tumour.

The semi-automatic algorithm enhanced and segmented the blood vessels used for mathematical morphology with linear structures in different directions. The algorithm was evaluated against the manual investigation respect to the number of vessel-like structure. The results showed there is a linear relationship between the vessel-like structures and the total number of vessels in the vicinity of a lung tumour. This suggests the fraction of vessels correctly detected is a stable amongst the dataset.

Segmented vessel-like structures images used in order to count and calculate the lengths. The results of the vessels length are used to calculate the tortuosity of the vessels. The quantification of the vessel-like structure was obtained in the area of a tumour and entire lung region. The affected side of a tumour was in both cases of tumour area or lung region was compared with the corresponding area of the contralateral side with no tumour. The algorithm was applied on the lung CT images of 40 patients who had only malignant lung tumour (lung1) and as well as patients have a benign (20 patients) and malignant (20 patients) tumour (lung2). The results from graphs obtained showed the number of vessel-like structures and the tortuosity of the vessels like structures in the vicinity of a tumour or the entire lung region compared to the corresponding area of the opposite side of lung with no tumour was not different in benign cases.

In contrast, malignant tumours show the number of the vessel-like structures in the vicinity of the unilateral side of tumour was significantly higher compared to the number of the vessel-like structures on the contralateral side with no tumour. The number of the vessel-like structures in the vicinity of the unilateral side of entire lung region also was significantly higher compared with the corresponding region of contralateral side with no tumour. The tortuosity of the vessels was not shown any differences in the tumour area compared to the non-tumour area in malignant tumour. Maybe due to the 3-dimensional CT images as the true length of vessels was not clearly presented in per image of the 2-dimensional image was assessed.

Visualisation and analysis of 3-dimensional lung CT images were performed. The visual results were clearly demonstrated that the numbers of vessels like structures and spicules in the vicinity of a tumour were higher compared with the side of no-tumour.

It is apparent that the developments in these areas are still at an early stage. The potential of this research is its use for the early stage of lung tumours detection. If a tumour detected and resected at an early stage survival may be improved.

6.9 Conclusion and Discussion

Segmented vessel-like structures images used in order to count, calculate the lengths and tortuosity of the vessels. According to the results, the number of vessel-like structures in an area of a lung tumour was higher compared with the contralateral side with no tumour in the case of malignant tumours. This was seen in 3-dimensional visualisation which was also applied to data from the dataset investigated. This involved removing the surrounding neighbouring area corresponding to ribs in order to focus on the lung region. Software was used to generate a 3-dimensional model of the lung. This advanced visual analysis helps to visually investigate the vessels around a tumour. This confirmed that the number of vessel-like structures and spicules in the vicinity of a lung tumour were higher compared with the contralateral side with no tumour. In contrast the results showed the number of vessel-like structures and the tortuosity of the vessels like structures in the vicinity of a tumour or the entire lung region compared to the corresponding area of the opposite side of lung with no tumour was not different in benign cases.

Chapter 7 Conclusion and Future Work

7.1 Introduction

IN this research study the development of methods for detection of thin structures in medical images such as cilia in microscope images and vessel-like structures from CT images has been presented. This chapter includes a summary of the project, results, final conclusions and possible future work.

7.2 Summary

It is considered useful to investigate disorders of structure or function in humans at an early stage. Diseases are more likely to be treated successfully and early stage and survival may be improved. Therefore this dissertation has investigated and analysed the structures from different biomedical images. This investigation was achieved by visual assessment along with development of a semi-automatic method for detection and analysis of thin structures from biomedical images. The data were analysed and quantified by use of graphs and statistical tests.

This thesis focused on two different medical application that is SEM images of cilia and lung CT images.

A) Microscope images of cilia

Visual analysis and semi-automatic segmentation of cilia from SEM microscope images were performed in order to quantify the thin structures of cilia. The 2-dimensional datasets included normal and abnormal cilia with different magnifications. The visual and semi-automatic assessment was performed on both normal and abnormal cilia.

Manual Analysis: The results obtained from manual assessment show the mean lengths of normal cilia were 2.3 μ m and mean lengths of abnormal cilia were 1.6 μ m. The number of clear and visible cilia was counted in the node. These results suggested that the lengths and number of cilia in the normal cilia were higher than the abnormal cilia (Goggolidou *et al.*,2014)

Development of a semi-automatic segmentation Algorithm: A median filter was applied to estimate the background and subtract it from the grayscale image to correct non-uniform illumination. A mathematical morphology operation with standard linear structure in various directions proved the best method of detection for detection of cilia. In addition, the emphasis was put on confirming the detection of cilia with the appropriate selection of parameters for cilia segmentation from high resolution images. The best parameters for cilia segmentation were found. The major-axis method was found to be best to measure the length of segmented cilia. The semi-automatic method best-fit-ellipse function was used to calculate the lengths of overlapping cilia. The median of the absolute difference between semi-automatic and manual measurements showed only small differences between the semi-automatic results and manual assessment.

The number of cilia was counted in normal and abnormal cilia images. 30% of the segmented pixels of each cilium were compared to the corresponding pixels in the labelled ground truth images.

B) Detection of Vessel-like structures in lung CT images

The main objective was to investigate the number of vessels in the vicinity of unilateral lung tumours and to compare this with the equivalent contralateral lung without tumour. The size of tumour, vessel number and vessel length in order to calculate the tortuosity were measured using 2-D slides of Lung CT images. Two different types of lung CT scan datasets were studied. MATLAB software (The MathWorks Inc., USA) was developed and applied in order to display and analyse the DICOM images.

Manual Analysis: In order to analyse the vessel-like structures and associated vessels in lung CT images, a process was required to highlight the vessel-like structures (Allisy-Roberts *et al.*, 2007). The brightness and contrast were adjusted using software in MATLAB. This also helped remove the other sections of image that were not required.

10 cases of unilateral primary lung cancer were investigated. In all ten cases, the number of clear vessel-like structures in the immediate vicinity of a lung tumour was greater than the corresponding area of the contralateral side with no tumour. In this manual analysis, there was more vessel in the vicinity of a tumour compared with the contralateral side with no tumour ($p < 0.001$) (Sadri *et al.*, 2016). The mean vessel tortuosity of these ten cases with primary lung cancer on the side of a tumour was slightly higher compared to the contralateral side with no tumour.

From the second dataset studied, 12 malignant and 11 benign cases were manually investigated. The number of vessels in the vicinity of the benign tumours was slightly higher compared to the contralateral side with no tumour but statistical results indicated no significant difference in the number of vessels. The mean of the vessel tortuosity in the vicinity of the benign tumours was similar to the contralateral side with no tumour.

In malignant tumours, the results showed the number of the vessels in the vicinity of a tumour was significantly higher compared with the corresponding area on the contralateral side with no tumour ($p < 0.001$).

The number of clear bright vessel-like structures in the immediate vicinity of a lung tumour may be higher than in the corresponding area on the contralateral side. The mean of the vessel tortuosity is slightly higher near a tumour compared to non-tumour side. These results were used to evaluate the algorithm.

Developed Algorithm: The semi-automatic algorithm was developed and applied to lung CT images to detect vessel-like structures in unilateral lung

tumour images. A Mathematical morphology algorithm with linear structure in various directions enhanced and segmented the vessel-like structures in order to count the vessels and calculate their lengths. Occasionally vessels appear are disconnected from their branch points. Therefore the semi-automatic algorithm reconstructs the vessel by using a cubic spline. The results of the vessels length were used to calculate the tortuosity of the vessels.

The system was validated against manual investigation for detection of vessel-like structures. The number of vessel-like structures for 40 cases from manual analysis compared with those detected by the algorithm (Sadri *et al.*, 2017).

Quantification of the vessel-like structures was obtained in the vicinity of a tumour and the entire lung region and was compared to the contralateral lung with no tumour. The algorithm was applied on lung CT images of 40 patients who had malignant lung tumours and also applied on a second dataset with 40 patients consisting of 20 cases of benign and 20 cases of malignant lung tumours.

The number of vessel-like structures and the vessel tortuosity in the vicinity of the lung tumour and the entire region of the lung compared to the contralateral side did not show any significance difference for benign tumours.

There was a clear difference between the malignant tumour results and benign tumour results. The number of vessel-like structures in the vicinity of the malignant lung tumours compared to the contralateral side with no tumour for both datasets was significantly different ($p < 0.001$). The mean of the vessel tortuosity in the vicinity of a lung tumour was not significantly different compared to the contralateral side with no tumour. Similar results were shown in the complete region of the lung.

The results from the second dataset either in the vicinity of a lung tumour or complete lung region were similar. The number of vessel-like structures in the vicinity of a lung tumour was higher compared with the contralateral side with no tumour ($p < 0.001$). The mean vessel tortuosity on the tumour side and the non-tumour side were similar.

7.3 Conclusion

The system was successfully applied to detect cilia from electron microscopy images and a novel semi-automatic algorithm for the detection and quantification of thin structures in medical images has been developed and applied to the new application of microscope images of cilia and lung CT images. This semi-automatic algorithm able to count and measure the lengths of thin structure of cilia and vessel-like structures.

In consequence according to the results, the number of vessel-like structures in an area of the lung tumour was higher compared with the contralateral side with no tumour in the case of malignant tumours.

3-dimensional visualisation was also applied to data from the dataset investigated. This involved removing the surrounding neighbouring area corresponding to ribs in order to focused on the lung region. Software was used to generate a 3-dimensional model of the lung. This advanced visual analysis helps to visually investigate the vessels around a tumour. This confirmed that the number of vessel-like structures and spicules in the vicinity of the lung tumour were higher compared with the contralateral side with no tumour.

Early tumour detestation and resection may increase survival rates. Thus this research merits further study in order to investigate if this approach may help enable early detection of lung tumours.

7.4 Achievements

Key results from the study include:

- a. Visual investigation of cilia in SEM Microscope images.
- b. Development of a method for semi-automatic segmentation and quantification of thin structures that was applied to SEM cilia images and lung CT images.
- c. Visual investigation of vessel-like structures associated with unilateral lung tumours demonstrated increased vessel like-structures in the vicinity of tumours. This was not seen in benign lung tumour images.
- d. The semi-automatic method was applied for detection of vessel-like structures in the vicinity of lung tumours and compared well with manual analysis.

References

American Cancer Society, (2018), <https://www.cancer.org/cancer/non-small-cell-lung-cancer/causes-risks-prevention/what-causes.html>. Accessed: 01/08/2017.

Cancer Research Uk. (2014). <http://www.cancerresearchuk.org/health-professional/cancer-statistics-for-the-uk>. Accessed: 10/07/2017.

Computed Tomography(CT) (2018). <https://www.webmd.boots.com/a-to-z-guides/what-is-a-ct-scan>. Accessed: 12/06/2017

Abdullah-Al-Wadud, M., Kabir, M. H., Dewan, M. A. A. and Chae, O. (2007) 'A dynamic histogram equalization for image contrast enhancement', IEEE Transactions on Consumer Electronics, 53 (2), pp. 593-600.

Adams, R. and Bischof, L. (1994) 'Seeded region growing', IEEE Transactions on Pattern Analysis and Machine Intelligence, 16 (6), pp. 641-647.

Agam, G., Armato, S. G. and Wu, C. (2005) 'Vessel tree reconstruction in thoracic CT scans with application to nodule detection', IEEE Transactions on Medical Imaging, 24 (4), pp. 486-499.

Ahmadi, K., Karimi, A. and Fouladi Nia, B. (2016) 'New Technique for Automatic Segmentation of Blood Vessels in CT Scan Images of Liver Based on Optimized Fuzzy-Means Method', Computational and Mathematical Methods in Medicine.

Allisy-Roberts, P. and Williams, J. R. (2007) Farr's physics for medical imaging. Elsevier Health Sciences, Saunders Ltd, pp 216.

Altman, D. G. and Bland, J. M. (1994) 'Diagnostic tests. 1: Sensitivity and specificity', BMJ (Clinical Research Ed.), 308 (6943), pp. 1552.

Armato, S. G., Hadjiiski, L., Tourassi, G. D., Drukker, K., Giger, M. L., Li, F., Redmond, G., Farahani, K., Kirby, J. S. and Clarke, L. P. (2015) 'Guest editorial: Lungx challenge for computerized lung nodule classification: reflections and lessons learned', Journal of Medical Imaging, 2 (2), pp. 020103-020103.

Astner, S., Dietterle, S., Otberg, N., Röwert-Huber, H., Stockfleth, E. and Lademann, J. (2008) 'Clinical applicability of in vivo fluorescence confocal microscopy for noninvasive diagnosis and therapeutic monitoring of nonmelanoma skin cancer', Journal of Biomedical Optics, 13 (1), pp. 014003-014003-12.

Baker, K. and Beales, P. L. (2009) Making sense of cilia in disease: the human ciliopathies. Wiley Online Library.

References

- Bartels, R. H., Beatty, J. C. and Barsky, B. A. (1987) An introduction to splines for use in computer graphics and geometric modeling. Morgan Kaufmann.
- Whiting FRCA FFICM P, N Singatullina FRCA EDIC and JH Rosser FRCA FFICM (2015), Computed tomography- chest, BJA Education, pp 299-304
- Bellomi, M. (2012) 'A classification of pulmonary nodules by CT scan', *Ecancermedalscience*, pp. 260.
- Bezdek, J. C. (2013) Pattern recognition with fuzzy objective function algorithms. Springer Science & Business Media.
- Bhatia, N. (2010) 'Survey of nearest neighbour techniques', ArXiv Preprint arXiv:1007.0085.
- Birring, S. S. and Peake, M. D. (2005) 'Symptoms and the early diagnosis of lung cancer', *Thorax*, 60 (4), pp. 268-269.
- Bullitt, E., Zeng, D., Gerig, G., Aylward, S., Joshi, S., Smith, J. K., Lin, W. and Ewend, M. G. (2005a) 'Vessel tortuosity and brain tumor malignancy: a blinded study1', *Academic Radiology*, 12 (10), pp. 1232-1240.
- Burger, Peter C, Bernd W Scheithauer, Francis Stephen Vogel (1991) 'Surgical pathology of the nervous system and its coverings'.
- C. Kirbas and F. K. H. Quek. (2003) Vessel extraction techniques and algorithms: a survey, in *Third IEEE*, pp. 238-245.
- Canny, J. F. (1983) Finding Edges and Lines in Images., Artificial Intelligence Lab Publications AITR-720.
- Cao, Y. and Langer, R. (2008) 'A review of Judah Folkman's remarkable achievements in biomedicine', *Proceedings of the National Academy of Sciences of the United States of America*, 105 (36), pp. 13203-13205.
- ÇELEBİ, Ö., Cengiz (2016) Neural Networks and Pattern Recognition Tutorial. New York: http://celebisoftware.com/Tutorials/neural_networks/Index.aspx Wiley-Intercedence Publication.
- Cervantes-Sanchez, F., Cruz-Aceves, I., Hernandez-Aguirre, A., Aviña-Cervantes, J. G., Solorio-Meza, S., Ornelas-Rodriguez, M. and Torres-Cisneros, M. (2016) 'Segmentation of Coronary Angiograms Using Gabor Filters and Boltzmann Univariate Marginal Distribution Algorithm', *Computational Intelligence and Neuroscience*.
- Chaudhuri, S., Chatterjee, S., Katz, N., Nelson, M. and Goldbaum, M. (1989) 'Detection of blood vessels in retinal images using two-dimensional matched filters', *IEEE Transactions on Medical Imaging*, 8 (3), pp. 263-269.

References

Cover, T. and Hart, P. (1967) 'Nearest neighbor pattern classification', IEEE Transactions on Information Theory, 13 (1), pp. 21-27.

Gabor D. (1946) 'Theory of communication. Part 1: The analysis of information', Electrical Engineers - Part III: Radio and Communication Engineering, Journal of the Institution of, 93 (26), pp. 429-441.

Datta, M., Via, L. E., Kamoun, W. S., Liu, C., Chen, W., Seano, G., Weiner, D. M., Schimel, D., England, K., Martin, J. D., Gao, X., Xu, L., Barry, C. E., 3rd and Jain, R. K. (2015) 'Anti-vascular endothelial growth factor treatment normalizes tuberculosis granuloma vasculature and improves small molecule delivery', Proceedings of the National Academy of Sciences of the United States of America, 112 (6), pp. 1827-1832.

Davies, J. (2018) British Lung Foundation., <https://www.blf.org.uk/>.

Davis, L. M., (2017), CT Scan Introduction., https://www.emedicinehealth.com/ct_scan/article_em.htm Medicine health.

Deswal, S., Gupta, S. and Bhushan, B. (2015) 'A Survey of Various Bilateral Filtering Techniques', International Journal of Signal Processing, Image Processing and Pattern Recognition, 8 (3), pp. 105-120.

Dixon, R. and Taylor, C. (1979) Automated asbestos fibre counting, in Inst Phys. Conf. Ser, pp. 178-185.

Duda, R. O., Hart, P. E. and Stork, D. G. (2012) Pattern classification. Second Edition John Wiley & Sons.

Dunn, J. C. (1973) 'A fuzzy relative of the ISODATA process and its use in detecting compact well-separated clusters', Journal of Cybernetics, Volume 3, Issue 3, pp 3257.

Eiho, S. and Qian, Y. (1997) Detection of coronary artery tree using morphological operator. IEEE, pp. 525-528.

Erdman, N. (2018) JEOL USA Electron Optics Documents, <https://www.jeolusa.com>.

Ermakov, A., Stevens, J. L., Whitehill, E., Robson, J. E., Pieleles, G., Brooker, D., Goggolidou, P., Powles-Glover, N., Hacker, T., Young, S. R., Dear, N., Hirst, E., Tymowska-Lalanne, Z., Briscoe, J., Bhattacharya, S. and Norris, D. P. (2009b) Mouse mutagenesis identifies novel roles for left-right patterning genes in pulmonary, craniofacial, ocular, and limb development. John Wiley & Sons, Inc. 238 (3), pp. 581-594.

Gillian Lieberman, Esguerra, A. (2004) Interactive Radiological Tutorials, Yale school of medicine. <http://eradiology.bidmc.harvard.edu/interactivetutorials/>.

Ferlay, J., Soerjomataram, I., Dikshit, R., Eser, S., Mathers, C., Rebelo, M., Parkin, D. M., Forman, D. and Bray, F. (2015a) 'Cancer incidence and

References

mortality worldwide: sources, methods and major patterns in Globocan', *International Journal of Cancer*, 136 (5), pp. E359-E386.

Frame, A. J., Undrill, P. E., Cree, M. J., Olson, J. A., McHardy, K. C., Sharp, P. F. and Forrester, J. V. (1998) 'A comparison of computer based classification methods applied to the detection of microaneurysms in ophthalmic fluorescein angiograms', *Computers in Biology and Medicine*, 28 (3), pp. 225-238.

Frangi, A. F., Niessen, W. J., Vincken, K. L. and Viergever, M. A. (1998) Multiscale vessel enhancement filtering. *International Conference on Medical Image Computing and Computer-Assisted Intervention*, pp. 130-137, Springer.

Fraz, M. M., Remagnino, P., Hoppe, A., Uyyanonvara, B., Rudnicka, A. R., Owen, C. G. and Barman, S. A. (2012) 'Blood vessel segmentation methodologies in retinal images – A survey', *Computer Methods and Programs in Biomedicine*, 108 (1), pp. 407-433.

Gao, F., Ge, X., Li, M., Zheng, X., Xiao, L., Zhang, G. and Hua, Y. (2015) 'CT features of lung scar cancer', *Journal of Thoracic Disease*, 7 (3), pp. 273-280.

Goggolidou, P., Stevens, J. L., Agueci, F., Keynton, J., Wheway, G., Grimes, D. T., Patel, S. H., Hilton, H., Morthorst, S. K., DiPaolo, A., Williams, D. J., Sanderson, J., Khoronenkova, S. V., Powles-Glover, N., Ermakov, A., Esapa, C. T., Romero, R., Dianov, G. L., Briscoe, J., Johnson, C. A., Pedersen, L. B. and Norris, D. P. (2014) 'ATMIN is a transcriptional regulator of both lung morphogenesis and ciliogenesis', *Development (Cambridge, England)*, 141 (20), pp. 3966-3977.

Gonzalez, R. C. and Woods, R. E. (eds.) (2008.) *Digital Image Processing*, Third Edition, edn. Principal Hall,

Grove, O., Berglund, A. E., Schabath, M. B., Aerts, H. J., Dekker, A., Wang, H., Velazquez, E. R., Lambin, P., Gu, Y. and Balagurunathan, Y. (2015) 'Quantitative computed tomographic descriptors associate tumor shape complexity and intratumor heterogeneity with prognosis in lung adenocarcinoma', *PloS One*, 10 (3), pp. e0118261.

Ha D. M., P. J. Mazzone, 2015, "Pulmonary Nodules, American Thoracic Society ", vol. 30, pp. 881-889.

Han, H. C. (2012) 'Twisted blood vessels: symptoms, etiology and biomechanical mechanisms', *Journal of Vascular Research*, 49 (3), pp. 185-197.

Hart, W. E., Goldbaum, M., Cote, B., Kube, P. and Nelson, M. R. (1997) 'Automated measurement of retinal vascular tortuosity', *Proceedings : A Conference of the American Medical Informatics Association. AMIA Fall Symposium*, pp. 459-463.

References

- Hassanat, A. B., Abbadi, M. A., Altarawneh, G. A. and Alhasanat, A. A. (2014) Solving the problem of the k parameter in the KNN classifier using an ensemble learning approach, ArXiv Preprint arXiv:1409.0919.
- Helmberger, M., Pienn, M., Urschler, M., Kullnig, P., Stollberger, R., Kovacs, G., Olschewski, A., Olschewski, H. and Bálint, Z. (2014) 'Quantification of tortuosity and fractal dimension of the lung vessels in pulmonary hypertension patients', Plos One, 9 (1), pp. e87515.
- Helmlinger, G., Sckell, A., Dellian, M., Forbes, N. S. and Jain, R. K. (2002) 'Acid production in glycolysis-impaired tumors provides new insights into tumor metabolism', Clinical Cancer Research: An Official Journal of the American Association for Cancer Research, 8 (4), pp. 1284-1291.
- Hernandez, M., Frangi, A. F. and Sapiro, G. (2003) Three-dimensional segmentation of brain aneurysms in CTA using non-parametric region-based information and implicit deformable models: Method and evaluation. Springer in International Conference on Medical Image Computing and Computer - Assisted Intervention, pp 594-602.
- Hirsch, F. R., Franklin, W. A., Gazdar, A. F. and Bunn, P. A., Jr (2001) 'Early detection of lung cancer: clinical perspectives of recent advances in biology and radiology', Clinical Cancer Research: An Official Journal of the American Association for Cancer Research, 7 (1), pp. 5-22.
- Holtzman-Gazit, M., Kimmel, R., Peled, N. and Goldsher, D. (2006) 'Segmentation of thin structures in volumetric medical images', IEEE Transactions on Image Processing, 15 (2), pp. 354-363.
- Huang, S., Chang, R., Moon, W. K., Lee, Y., Chen, D. and Suri, J. S. (2008) 'Analysis of tumor vascularity using three-dimensional power Doppler ultrasound images', IEEE Transactions on Medical Imaging, 27 (3), pp. 320-330.
- Jain, R. K. (2013) 'Normalizing tumor microenvironment to treat cancer: bench to bedside to biomarkers', Journal of Clinical Oncology, 31 (17), pp. 2205-2218.
- Jonk, A. M., Houben, A. J., de Jongh, R. T., Serne, E. H., Schaper, N. C. and Stehouwer, C. D. (2007) 'Microvascular dysfunction in obesity: a potential mechanism in the pathogenesis of obesity-associated insulin resistance and hypertension', Physiology (Bethesda, Md.), 22 pp. 252-260.
- Kande, G. B., Subbaiah, P. V. and Savithri, T. S. (2010) 'Unsupervised fuzzy based vessel segmentation in pathological digital fundus images', Journal of Medical Systems, 34 (5), pp. 849-858.
- Kang, W., Kang, W., Li, Y. and Wang, Q. (2013) The segmentation method of degree-based fusion algorithm for coronary angiograms in Measurement, Information and Control, International Conference. IEEE.

References

- Karssemeijer, N. and te Brake, G. M. (1996) 'Detection of stellate distortions in mammograms', *IEEE Transactions on Medical Imaging*, 15 (5), pp. 611-619.
- Kass, M., Witkin, A. and Terzopoulos, D. (1988) 'Snakes: Active contour models', *International Journal of Computer Vision*, 1 (4), pp. 321-331.
- Kaur, J. and Sinha, H. (2012) 'Automated detection of retinal blood vessels in diabetic retinopathy using Gabor filter', *International Journal of Computer Science and Network Security*, 4 (12-14), pp. 109-116.
- Kaur, S. (2015) 'Noise types and various removal techniques', *International Journal of Advanced Research in Electronics and Communication Engineering (IJARECE)*, 4 (2), pp. 226-230.
- Kharghanian, R. and Ahmadyfard, A. (2012) 'Retinal blood vessel segmentation using gabor wavelet and line operator', *International Journal of Machine Learning and Computing*, 2 (5), pp. 593.
- Kikinis, R., Gleason, P. L., Moriarty, T. M., Moore, M. R., Alexander III, E., Stieg, P. E., Matsumae, M., Lorensen, W. E., Cline, H. E. and Black, P. M. (1996) 'Computer-assisted interactive three-dimensional planning for neurosurgical procedures', *Neurosurgery*, 38 (4), pp. 640-651.
- Kiraly, A. P., Pichon, E., Naidich, D. P. and Novak, C. L. (2004) Analysis of arterial subtrees affected by pulmonary emboli. *International Society for Optics and Photonics*. pp. 1720-1729.
- Kramer-Zucker, A. G., Olale, F., Haycraft, C. J., Yoder, B. K., Schier, A. F. and Drummond, I. A. (2005) 'Cilia-driven fluid flow in the zebrafish pronephros, brain and Kupffer's vesicle is required for normal organogenesis', *Development (Cambridge, England)*, 132 (8), pp. 1907-1921.
- Krissian, K., Malandain, G., Ayache, N., Vaillant, R. and Troussel, Y. (2000) 'Model-based detection of tubular structures in 3D images', *Computer Vision and Image Understanding*, 80 (2), pp. 130-171.
- Krupinski, E. A. (2004) 'Computer-aided detection in clinical environment: benefits and challenges for radiologists', *Radiology*, 231 (1), pp. 7-9.
- Lalkhen, A. G. and McCluskey, A. (2008) 'Clinical tests: sensitivity and specificity', *Continuing Education in Anaesthesia Critical Care & Pain*, 8 (6), pp. 221-223.
- Landini L., Positano V. and Santarelli M.F (2008) *3D Medical Image Processing*. Springer, Berlin, pp. 68-74.
- Leung, A., Smithuis, R. (2007) solitary-pulmonary-nodule-benign-versus-malignant, <http://www.radiologyassistant.nl/en/p460f9fcd50637/solitary-pulmonary-nodule-benign-versus-malignant.html>.

References

- Levin, M. (2005) 'Left–right asymmetry in embryonic development: a comprehensive review', *Mechanisms of Development*, 122 (1), pp. 3-25.
- Levy, B. I., Schiffrin, E. L., Mourad, J. J., Agostini, D., Vicaud, E., Safar, M. E. and Struijker-Boudier, H. A. (2008) 'Impaired tissue perfusion: a pathology common to hypertension, obesity, and diabetes mellitus', *Circulation*, 118 (9), pp. 968-976.
- Lewis, D. W. (1991) *Matrix theory*. World Scientific Publishing Co, pp.298.
- Lin, C. H., Li, T. C., Tsai, P. P. and Lin, W. C. (2015) 'The relationships of the pulmonary arteries to lung lesions aid in differential diagnosis using computed tomography', *BioMedicine*, 5 (2), pp. 11-015-0011.
- Lindeberg, T. (1998) 'Edge detection and ridge detection with automatic scale selection', *International Journal of Computer Vision*, 30 (2), pp. 117-156.
- Linden, A. (2006) 'Measuring diagnostic and predictive accuracy in disease management: an introduction to receiver operating characteristic (ROC) analysis', *Journal of Evaluation in Clinical Practice*, 12 (2), pp. 132-139.
- Lorthois, S., Lauwers, F. and Cassot, F. (2014) 'Tortuosity and other vessel attributes for arterioles and venules of the human cerebral cortex', *Microvascular Research*, 91 pp. 99-109.
- Luessi, M., Eichmann, M., Schuster, G. M. and Katsaggelos, A. K. (2009) 'Framework for efficient optimal multilevel image thresholding', *Journal of Electronic Imaging*, 18 (1), pp. 013004-013004-10.
- Lusic, H. and Grinstaff, M. W. (2012) 'X-ray-computed tomography contrast agents', *Chemical Reviews*, 113 (3), pp. 1641-1666.
- Malek, J., Azar, A. T. and Tourki, R. (2015) 'Impact of retinal vascular tortuosity on retinal circulation', *Neural Computing and Applications*, 26 (1), pp. 25-40.
- Marti, R., Zwiggelaar, R. and Rubin, C. M. (2001) *Tracking Mammographic Structures Over Time*. pp. 1-10.
- McCollough, C. H. and Morin, R. L. (1994) 'The technical design and performance of ultrafast computed tomography', *Radiologic Clinics of North America*, 32 (3), pp. 521-536.
- McGill, R., Tukey, J. W. and Larsen, W. A. (1978) 'Variations of box plots', *The American Statistician*, 32 (1), pp. 12-16.
- Menzl, Ina, Lebeau, Lauren,. (2014) 'Loss of primary cilia occurs early in breast cancer development', 3 (2046-2530), pp. 7.

References

- Mori, K., Hasegawa, J., Toriwaki, J., Anno, H. and Katada, K. (1995) Automated extraction and visualization of bronchus from 3D CT images of lung. Springer.pp.542-548.
- Murfee, W. L. and Schmid-Schönbein, G. W. (2008) 'Structure of microvascular networks in genetic hypertension', *Methods in Enzymology*, 444 pp. 271-284.
- N. Sadri, D. Wertheim, (2016) Investigation of Vessel Structure in the Vicinity of Lung Tumours, London, Thorax 71: A8.
- N. Sadri, D. Wertheim, (2017) Computer detection of thin structures in lung CT images, BIR Annual Congress, London.
- Niehaus, R., Raicu, D. S., Furst, J. and Armato, S. (2015) 'Toward understanding the size dependence of shape features for predicting spiculation in lung nodules for computer-aided diagnosis', *Journal of Digital Imaging*, 28 (6), pp. 704-717.
- Niemeijer, M., Staal, J., van Ginneken, B., Loog, M. and Abramoff, M. D. (2004) Comparative study of retinal vessel segmentation methods on a new publicly available database. *International Society for Optics and Photonics* 648-656.
- Niemeijer, M., Van Ginneken, B., Staal, J., Suttorp-Schulten, M. S. and Abramoff, M. D. (2005) 'Automatic detection of red lesions in digital color fundus photographs', *IEEE Transactions on Medical Imaging*, 24 (5), pp. 584-592.
- Norris, D. P. and Grimes, D. T. (2012) 'Mouse models of ciliopathies: the state of the art', *Disease Models & Mechanisms*, 5 (3), pp. 299-312.
- Oh, E. C. and Katsanis, N. (2012) 'Cilia in vertebrate development and disease', *Development (Cambridge, England)*, 139 (3), pp. 443-448.
- Olson, Eric J. (2017) Can Lung Nodules be cancerous. <https://www.mayoclinic.org/diseases-conditions/lung-cancer/expert-answers/lung-nodules/faq-20058445>.
- Patel P. H. M., 2017, "Solitary Pulmonary Nodule, <https://emedicine.medscape.com/article/2139920-overview>, Department of Pulmonary, Critical Care and Sleep Medicine, St Louis University Hospital.
- Paul, C. (2017) What is Confocal Laser Scanning Microscopy, <https://bitesizebio.com/19958/what-is-confocal-laser-scanning-microscopy>.
- Pezzella, F. and Gatter, K. (2015) 'Non-angiogenic tumours unveil a new chapter in cancer biology', 235: 381–383.
- Pizer, S. M., Amburn, E. P., Austin, J. D., Cromartie, R., Geselowitz, A., Greer, T., ter Haar Romeny, B., Zimmerman, J. B. and Zuiderveld, K. (1987)

References

'Adaptive histogram equalization and its variations', Computer Vision, Graphics, and Image Processing, 39 (3), pp. 355-368.

Reza, A. M. (2004) 'Realization of the contrast limited adaptive histogram equalization (CLAHE) for real-time image enhancement', Journal of VLSI Signal Processing Systems for Signal, Image and Video Technology, 38 (1), pp. 35-44.

Ricci, E. and Perfetti, R. (2007) 'Retinal Blood Vessel Segmentation Using Line Operators and Support Vector Classification', Medical Imaging, IEEE Transactions on, 26 (10), pp. 1357-1365.

Rudyanto, R. D., Kerkstra, S., Van Rikxoort, E. M., Fetita, C., Brillet, P., Lefevre, C., Xue, W., Zhu, X., Liang, J. and Öksüz, İ. (2014) 'Comparing algorithms for automated vessel segmentation in computed tomography scans of the lung: the VESSEL12 study', Medical Image Analysis, 18 (7), pp. 1217-1232.

Sae-Tang, W., Chiracharit, W. and Kumwilaisak, W. (2010) Exudates detection in fundus image using non-uniform illumination background subtraction. IEEE.pp. 204-209.

Salem, N. M. and Nandi, A. K. (2006) Segmentation of retinal blood vessels using scale-space features and K-nearest neighbour classifier. IEEE. international Conference on Acoustics Speech and signal processing proceeding,pp. II-II.

Satir, P. and Christensen, S. T. (2007) 'Overview of structure and function of mammalian cilia', Annu.Rev.Physiol., 69 pp. 377-400.

Sato, Y., Nakajima, S., Atsumi, H., Koller, T., Gerig, G., Yoshida, S. and Kikinis, R. (1997) 3D multi-scale line filter for segmentation and visualization of curvilinear structures in medical images. Springer.pp.213-222

Shoemark, A. (2014) structure and function of Cilia., <http://www.ciliopathyalliance.org/cilia/structure-and-function-of-cilia.html>.

Siemann, D. W., Mercer, E., Lepler, S. and Rojiani, A. M. (2002) 'Vascular targeting agents enhance chemotherapeutic agent activities in solid tumor therapy', International Journal of Cancer, 99 (1), pp. 1-6.

Slezak, D., Pal, S., Kang, B., Gu, J., Kuroda, H. and Kim, T. (2009) Signal Processing, Image Processing and Pattern Recognition: International Conference, SIP, Held as Part of the Future Generation Information Technology Conference, FGIT, Jeju Island, Korea, December 10-12, Proceedings. Springer.

Soares, J. V., Leandro, J. J., Cesar, R. M., Jelinek, H. F. and Cree, M. J. (2006) 'Retinal vessel segmentation using the 2-D Gabor wavelet and supervised classification', IEEE Transactions on Medical Imaging, 25 (9), pp. 1214-1222.

References

- Solomon, C. and Breckon, T. (eds.) (2011) *Fundamentals of Digital Image Processing: A Practical Approach with Examples in Matlab*. Wiley Online Library: John Wiley & Sons, Ltd.
- Spencer, T., Olson, J. A., McHardy, K. C., Sharp, P. F. and Forrester, J. V. (1996) 'An image-processing strategy for the segmentation and quantification of microaneurysms in fluorescein angiograms of the ocular fundus', *Computers and Biomedical Research*, 29 (4), pp. 284-302.
- Sulik, K., Dehart, D., Inagaki, T., Carson, J., Vrablic, T., Gesteland, K. and Schoenwolf, G. (1994) 'Morphogenesis of the murine node and notochordal plate', *Developmental Dynamics*, 201 (3), pp. 260-278.
- Sun, K. and Sang, N. (2008) 'Morphological enhancement of vascular angiogram with multiscale detected by Gabor filters', *Electronics Letters*, 44 (2), pp. 1.
- Koller T. M., G. Gerig, G. Szekely and D. Dettwiler. (1995) Multiscale detection of curvilinear structures in 2-D and 3-D image data, in *Proceeding of IEEE International Conference on Computer Vision*, pp 864-869.
- Tamura, A. (2016) 'Tuberculosis and Lung Cancer', *Kekkaku: [Tuberculosis]*, 91 (1), pp. 17-25.
- Teoh, S. H. and Ibrahim, H. (2012) 'Median filtering frameworks for reducing impulse noise from grayscale digital images: a literature survey', *International Journal of Future Computer and Communication*, 1 (4), pp. 323.
- Terzopoulos, D. (1987) On matching deformable models to images, in *Topical Meeting on Machine Vision Tech. Digest Series*, pp. 160-167.
- Valli G, (1997) "An Algorithm for Real-time Vessel Enhancement and Detection, Riccardo Poli School of Computer Science The University of Birmingham,".
- Vandermeulen, D., Delaere, D., Suetens, P., Bosmans, H. and Marchal, G. (1992) Local filtering and global optimization methods for 3-d magnetic-resonance angiography image enhancement. *International Society for Optics and Photonics*.pp.274-288.
- Varma, D. R. (2012) 'Managing DICOM images: Tips and tricks for the radiologist', *The Indian Journal of Radiology & Imaging*, 22 (1), pp. 4-13.
- Viggiano, R. W., Swensen, S. J. and Rosenow, E. C.,3rd (1992) 'Evaluation and management of solitary and multiple pulmonary nodules', *Clinics in Chest Medicine*, 13 (1), pp. 83-95.
- Waters, A. M. and Beales, P. L. (2011) 'Ciliopathies: an expanding disease spectrum', *Pediatric Nephrology*, 26 (7), pp. 1039-1056.
- Wielputz, M. O., Heussel, C. P., Herth, F. J. and Kauczor, H. U. (2014) 'Radiological diagnosis in lung disease: factoring treatment options into the

References

choice of diagnostic modality', *Deutsches Arzteblatt International*, 111 (11), pp. 181-187.

Wiernsperger, N., Nivoit, P., De Aguiar, L. and Bouskela, E. (2007) 'Microcirculation and the metabolic syndrome', *Microcirculation*, 14 (4-5), pp. 403-438.

Willis, R. A. (1934) *The spread of tumours in the human body*. London J. & A. Churchill, pp 196.

Winston Tan W. (2018) "Non-Small Cell Lung Cancer Clinical Presentation," <https://emedicine.medscape.com/article/279960-clinical>.

Xu, C., Hao, K., Song, Y., Yu, L., Hou, Z. and Zhan, P. (2013) 'Early diagnosis of solitary pulmonary nodules', *Journal of Thoracic Disease*, 5 (6), pp. 830-840.

Yang, J., Ma, S., Tan, W., Sun, Q., P Cao, P. and Zhao, D. (2015) 'MRA Fuzzy c-Means Vessel Segmentation Algorithm Based on Tubular Structure', *Journal of Medical Imaging and Health Informatics*, 5 (8), pp. 1853-1858.

Yim P. J., P. L. Choyke and R. M. Summers. (2000) "Gray-scale skeletonization of small vessels in magnetic resonance angiography," *IEEE Trans. Med. Imaging*, vol. 19, (6), pp. 568-576.

Yuan, K., Frolova, N., Xie, Y., Wang, D., Cook, L., Kwon, Y. J., Steg, A. D., Serra, R. and Frost, A. R. (2010) 'Primary cilia are decreased in breast cancer: analysis of a collection of human breast cancer cell lines and tissues', *The Journal of Histochemistry and Cytochemistry : Official Journal of the Histochemistry Society*, 58 (10), pp. 857-870.

Zana, F. and Klein, J. (2001) 'Segmentation of vessel-like patterns using mathematical morphology and curvature evaluation', *IEEE Transactions on Image Processing*, 10 (7), pp. 1010-1019.

Zerhouni, E. A., Stitik, F. P., Siegelman, S. S., Naidich, D. P., Sagel, S. S., Proto, A. V., Muhm, J. R., Walsh, J. W., Martinez, C. R. and Heelan, R. T. (1986) 'CT of the pulmonary nodule: a cooperative study', *Radiology*, 160 (2), pp. 319-327.

Zhang, B., Zhang, L., and Karray, F. (2010) 'Retinal vessel extraction by matched filter with first-order derivative of Gaussian', *Computers in Biology and Medicine*, 40 (4), pp. 438-445.

Zhou, X., Hayashi, T., Hara, T., Fujita, H., Yokoyama, R., Kiryu, T. and Hoshi, H. (2006) 'Automatic segmentation and recognition of anatomical lung structures from high-resolution chest CT images', *Computerized Medical Imaging and Graphics*, 30 (5), pp. 299-313.

Zucker, S. W. (1976) 'Region growing: Childhood and adolescence', *Computer Graphics and Image Processing*, 5 (3), pp. 382-399.

References

Zwiggelaar, R., Astley, S. M., Boggis, C. R. and Taylor, C. J. (2004) 'Linear structures in mammographic images: detection and classification', IEEE Transactions on Medical Imaging, 23 (9), pp. 1077-1086.

Zwiggelaar, R., Parr, T. C. and Taylor, C. J. (1996) Finding Orientated Line Patterns in Digital Mammographic Images.

Zwirewich, C. V., Vedal, S., Miller, R. R. and Muller, N. L. (1991) 'Solitary pulmonary nodule: high-resolution CT and radiologic-pathologic correlation', Radiology, 179 (2), pp. 469-476.